Neutrino Induced Coherent Pion Production

Daniel Ivan Scully

Thesis submitted in partial fulfilment of the requirements
for the degree of Doctor of Philosophy in Physics

University of Warwick, Department of Physics

September 2013

Contents

Tables

Figures

Acknowledgements

Callie

My Parents

Dr Gary Barker & Dr Steve Boyd

Ally Caldecote

Dr Leigh Whitehead, Callum Lister,
and my many other office colleagues

Declarations

The material presented in this document has not been published or submitted for examination at another institute. It represents my own work unless stated otherwise, complete with references.

Chapter 3 and Chapter 4 make substantial use of the GENIE neutrino interaction simulation. It is the work of the GENIE collaboration, whom I have assisted with maintenance of its Rein-Sehgal model, as well as contributing an implementation of the Alvarez-Ruso model.

I implemented the Alvarez-Ruso model described in Chapter 4 into GENIE using the original papers and code provided to me by the authors. I am grateful for the guidance provided to me in this task by Dr Luis Alvarez-Ruso and Dr Costas Andreopoulos. I am also grateful to Steve Dennis for assisting me in interfacing the model with GENIE's framework, and particularly to Dr Steve Boyd for essential help in optimising its performance.

Chapter 5 describes the T2K experiment, an international collaboration to which hundreds of people have contributed, myself included. The more substantial of my contributions included taking a leading role in the construction of six "P0D ECal" sub-detector modules which form part of the experiment's off-axis near detector. I also made substantial contributions to the near detector's software infrastructure, including maintaining the interface to the simulated detector geometries, the writing of that geometry for the ECals and contributing to the ECal reconstruction algorithms.

The analysis presented in Chapter 6 is my own work, though it draws on studies and selections reported by other members of the T2K collaboration, which have been appropriately referenced. I am grateful to Dr David Hadley for assistance in implementing the result calculation procedure described in Section 6.9.

Abstract

Neutrino-induced coherent pion production is an important channel for the study of neutrino-nucleus interactions. It is both a dangerous background for ν_e oscillation experiments, and a critical component required for precise understanding of neutrino-nucleus pion production in general.

The body of experimental evidence for coherent pion production at high neutrino energies is reviewed. This data is described well by the Rein-Sehgal model, which is described and studied. In light of recent low energy limits set below the Rein-Sehgal model cross-section an alternative low energy model, the Alvarez-Ruso model, was implemented in the neutrino interaction simulation GENIE. The results of this simulation are compared with those from the Rein-Sehgal model, and briefly with those from other models.

Finally, a search for ν_μ-induced charged-current (CC) coherent pion production on ^{12}C was conducted at a mean neutrino energy of 0.86 GeV, using data from the T2K experiment's off-axis near detector. A $3.0\,\sigma$ excess of events was found above the background prediction, constituting the first experimental evidence of CC coherent pion production below 7 GeV. Preliminary attempts to interpret this excess in the context of the Rein-Sehgal and Alvarez-Ruso models found cross-sections consistent with the limits set by SciBooNE.

1. Introduction

The discovery of the Higgs boson at the LHC last year [1] [2] marked the completion of the Standard Model of particle physics. Arguably it has been one of the most successful theories in the history of scientific endeavour, however we already know it is insufficient.

The discovery of neutrino oscillations has proved that the neutrinos are not all massless, as they are assumed to be by the Standard Model. Though many theoretical approaches have been suggested on how this can be accommodated, experimental guidance is urgently required.

Likewise, the Standard Model is unable to provide an explanation of the baryonic matter – anti-matter asymmetry of the Universe. It was noted by Sakharov [3] that a solution to this problem would require some form of CP-violation in the early Universe. Though evidence of CP-violation has been found in the quark sector, additional physics beyond the Standard Model is required to account for the observed size of the asymmetry [4].

Once again the discovery of neutrino oscillations could hold the answer since the phenomenon also allows for the possibility of leptonic CP-violation. Various mechanisms have been proposed that would allow CP-violation in the lepton sector to provide the necessary asymmetry in the baryons [5]. Establishing whether or not CP-violation does occur in neutrinos is therefore a priority.

It is clear that the study of neutrinos is of vital importance to the future development of particle physics, in particular through the study of oscillations. However, as will be discussed in Chapter 2, precision measurements of neutrino oscillations are predicated on improving our understanding of neutrino-nucleus interactions.

There are multiple channels through which neutrinos can interact with nuclei and, as described in Chapter 3, many of them are in need of improvements in both our experimental and theoretical understanding. In Chapter 4 one interaction channel, coherent pion production, is identified as being of particular importance to the field, in need of experimental input, and with the

potential for significant improvements in the near future. The T2K neutrino oscillation experiment, described in Chapter 5, provided an opportunity to contribute to this field, the results of which are reported in Chapter 6.

2. Neutrinos & Neutrino Oscillations

The existence of a light, weakly-interacting neutral particle was first suggested by Wolfgang Pauli in 1930 to explain the energy spectrum observed for electrons/positrons emitted in beta decays. Although not universally popular at first (even Pauli himself was sceptical) the idea eventually became widely accepted, but it was not until 1956 that the first experimental detection of "neutrinos" was made [6].

In the decades which followed discovery, their use in experiments was as probes of other physics. For example, the study of solar neutrinos was mainly motivated by understanding the fusion processes present in the Sun. Likewise, accelerator-based neutrino beams were made to study the workings of the weak force at lower energies than would be possible with electromagnetically or strongly interacting particles.

It wasn't until observation of the solar and atmospheric neutrino problems, and the eventual discovery of neutrino oscillations, that neutrinos became of interest in their own right.

2.1. Neutrino States

The leptons, like all matter particles in the Standard Model, exhibit the peculiar feature that the states in which they undergo charged-current weak interactions, "flavour states", are not mass eigenstates[1]. Instead the three flavour states are a superposition, or mixture, of the three mass states [7].

Experimentally we have the freedom to define the reference point from which the flavour states are measured. Conventionally in quarks, we define the flavour states in terms of the up-type quarks, such that all the mixing occurs in the down-type quarks. Similarly in neutrinos, the convention is to define the flavour states in terms of the charged leptons with all the mixing confined to

1. This is unlike the electromagnetic and strong interactions, whose interaction states are mass eigenstates.

the neutrinos. There is good reason for this choice: the fact that neutrinos interact only weakly and that the differences between their masses are tiny, make it impossible to measure which mass state has been created.

One will sometimes find one or other of the flavour/mass states being described as the "physical" states (usually mass in quarks and flavour in neutrinos) but such a description is misleading. It is the measurement being made which determines which states are important, and any perception that one set is more "real" than another is simply an artefact of the view the experimenter has.

It is natural to assume that like the other fermions each neutrino flavour ν_α has an anti-matter equivalent $\bar{\nu}_\alpha$, i.e. that they are Dirac particles. However because of their neutral charge it is possible that neutrinos could be Majorana particles. If this were to be the case then neutrinos would be their own anti-particles and they could have both Majorana and Dirac masses.

Today it is thought there are three neutrino flavour states which are defined by the charged lepton they interact with at charged-current weak vertices: ν_e, ν_μ and ν_τ. There are also three mass states ν_1, ν_2, ν_3 with masses m_1, m_2 and m_3 respectively:

The mass and flavour states are related by a mixing matrix:

$$\begin{pmatrix} \nu_e \\ \nu_\mu \\ \nu_\tau \end{pmatrix} = \begin{pmatrix} U_{e1} & U_{e2} & U_{e3} \\ U_{\mu 1} & U_{\mu 2} & U_{\mu 3} \\ U_{\tau 1} & U_{\tau 2} & U_{\tau 3} \end{pmatrix} \begin{pmatrix} \nu_1 \\ \nu_2 \\ \nu_3 \end{pmatrix} \tag{2.1}$$

This unitary matrix is known as the "Pontecorvo-Maki-Nakagawa-Sakata" matrix [8] [9]. The expression can also be inverted to express the mass states, i, in terms of the flavour states, α, highlighting the fact that they are both mixtures of each other:

$$\nu_i = \sum_\alpha U^*_{\alpha i} \nu_\alpha \tag{2.2}$$

It is convenient for experimental purposes to parametrise the PMNS matrix as the product of four sub-matrices [7]:

$$U_{\text{PMNS}} = \begin{pmatrix} 1 & 0 & 0 \\ 0 & \cos\vartheta_{23} & \sin\vartheta_{23} \\ 0 & -\sin\vartheta_{23} & \cos\vartheta_{23} \end{pmatrix} \begin{pmatrix} \cos\vartheta_{13} & 0 & \sin\vartheta_{13}e^{-i\delta} \\ 0 & 1 & 0 \\ -\sin\vartheta_{13}e^{-i\delta} & 0 & \cos\vartheta_{13} \end{pmatrix} \begin{pmatrix} \cos\vartheta_{12} & \sin\vartheta_{12} & 0 \\ -\sin\vartheta_{12} & \cos\vartheta_{12} & 0 \\ 0 & 0 & 1 \end{pmatrix} \begin{pmatrix} e^{\frac{1}{2}i\alpha_1} & 0 & 0 \\ 0 & e^{\frac{1}{2}i\alpha_2} & 0 \\ 0 & 0 & 1 \end{pmatrix} \quad (2.3)$$

This parametrisation consists of three mixing angles (ϑ_{12}, ϑ_{23} and ϑ_{13}) two Majorana CP-violating phases (α_1 and α_2) and one Dirac CP-violating phase (δ).

The value of the three mixing angles effectively determines the degree to which the mass and flavour states are mixed.

The phases α_1 and α_2 are only physically observable if neutrinos are Majorana particles. Even if they exist it will be very difficult to measure their values experimentally, but in either case they do not contribute at all to neutrino oscillations (so they will be neglected from here on in).

However the final phase δ, which is commonly referred to as δ_{cp}, is directly observable and, if its value is non-zero, represents the source of leptonic CP-violation which most strongly motivates our interest in oscillations. As can be seen in Equation 2.3 however, it only appears with terms of $\sin\vartheta_{13}$ so, regardless of the value of δ_{cp}, we also require $\vartheta_{13} \neq 0$ for any CP-violating effects to exist.

2.2. Neutrino Oscillations

Neutrino oscillations is a phenomenon which occurs as a result of the mixing of neutrino flavour and mass states discussed above. Experimentally it is the observation of a change in the flavour composition of neutrinos as they travel away from their source.

When a neutrino is created, it is created by the weak force, and therefore exists in a weak (flavour) eigenstate. So the wavefunction describing a pure source of ν_α at creation looks like:

$$\left|\ \psi(0,0)\right\rangle = \left|\ \nu_\alpha\right\rangle = U_{\alpha 1}\left|\ \nu_1\right\rangle + U_{\alpha 2}\left|\ \nu_2\right\rangle + U_{\alpha 3}\left|\ \nu_3\right\rangle \tag{2.4}$$

Later, after travelling a distance L through a vacuum the wavefunction becomes:

$$\left|\ \psi(\mathrm{L},\mathrm{t})\right\rangle = U_{\alpha 1}\left|\ \nu_1\right\rangle e^{-\mathrm{i}\varphi_1} + U_{\alpha 2}\left|\ \nu_2\right\rangle e^{-\mathrm{i}\varphi_2} + U_{\alpha 3}\left|\ \nu_3\right\rangle e^{-\mathrm{i}\varphi_3} \tag{2.5}$$

where, assuming a plane-wavefunction[2], each mass state has acquired a phase $\varphi_i = E_i t - |p_i|L$. Since each of these states represents a different mass, the phases are also slightly different. So as the neutrinos travel away from the source, the mass states get out of phase with one another and the resulting interference means that the wavefunction evolves to contain components from all three flavour states. This can be seen from Equation 2.5 by substituting the mass states for their flavour mixtures from Equation 2.2:

$$\begin{aligned}\left|\ \psi(\mathrm{L},\mathrm{t})\right\rangle \quad &= \left(U_{\alpha 1}\mathrm{U}^*_{\mathrm{e}1}e^{-\mathrm{i}\varphi_1} + U_{\alpha 2}\mathrm{U}^*_{\mathrm{e}2}e^{-\mathrm{i}\varphi_2} + U_{\alpha 3}\mathrm{U}^*_{\mathrm{e}3}e^{-\mathrm{i}\varphi_3}\right)\left|\ \nu_e\right\rangle \\ &+\left(U_{\alpha 1}\mathrm{U}^*_{\mu 1}e^{-\mathrm{i}\varphi_1} + U_{\alpha 2}\mathrm{U}^*_{\mu 2}e^{-\mathrm{i}\varphi_2} + U_{\alpha 3}\mathrm{U}^*_{\mu 3}e^{-\mathrm{i}\varphi_3}\right)\left|\ \nu_\mu\right\rangle \\ &+\left(U_{\alpha 1}\mathrm{U}^*_{\tau 1}e^{-\mathrm{i}\varphi_1} + U_{\alpha 2}\mathrm{U}^*_{\tau 2}e^{-\mathrm{i}\varphi_2} + U_{\alpha 3}\mathrm{U}^*_{\tau 3}e^{-\mathrm{i}\varphi_3}\right)\left|\ \nu_\tau\right\rangle\end{aligned} \tag{2.6}$$

After travelling a distance L through a vacuum the neutrino wavefunction, which was initially pure ν_α, is now a mixture of all three neutrino types and the proportion of each flavour varies as the neutrinos travel. This is neutrino oscillations.

Expanding Equation 2.6 out and calculating an example probability gets cumbersome so we make the assumption, valid at the resolution of current experiments, that δ_{cp} is zero to simplify things. Then for a beam of initially pure ν_μ with energy E, the probability of a neutrino being a ν_e at a distance L from the source is:

$$\begin{aligned}\mathrm{P}\left(\nu_\mu \rightarrow \nu_e\right) = {} & \sin^2\left(\vartheta_{23}\right)\sin^2\left(2\vartheta_{13}\right)\sin^2\left(\Delta\mathrm{m}^2{}_{32}\Phi\right) + \cos^2\left(\vartheta_{23}\right)\sin^2\left(2\vartheta_{13}\right)\sin^2\left(\Delta\mathrm{m}^2{}_{21}\Phi\right) \\ & + \cos\left(\vartheta_{13}\right)\sin\left(2\vartheta_{12}\right)\sin\left(2\vartheta_{13}\right)\sin\left(2\vartheta_{23}\right)\sin\left(\Delta\mathrm{m}^2{}_{32}\Phi\right)\sin\left(\Delta\mathrm{m}^2{}_{21}\Phi\right)\cos\left(\Delta\mathrm{m}^2{}_{32}\Phi\right)\end{aligned} \tag{2.7}$$

2. Assuming plane-wavefunctions gives the same results as a more complete treatments in all but extreme cases [10].

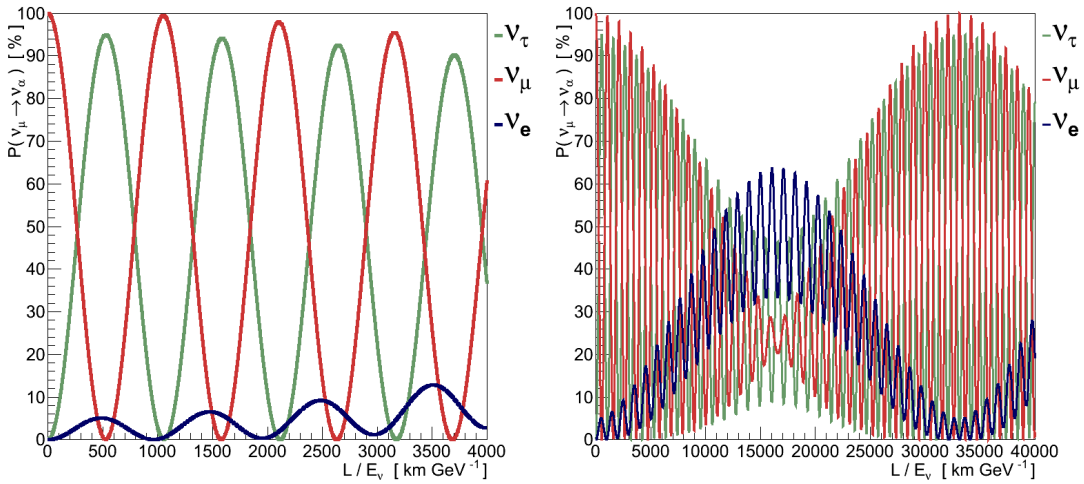

Figure 2.1: The detection probability of the three neutrino flavours from an initially pure ν_μ beam, as a function of L/E_ν (using values from Table 2.1). Over longer distances, or at lower energies, "beat" patterns emerge - the neutrinos essentially behave as three coupled oscillators. The fact that the ν_μ component can reach both 1 and 0 is a consequence of $\vartheta_{23} = 45\,^\circ$.

Where, for the sake of brevity:

$$\Phi = \frac{L}{4E} \tag{2.8}$$

and we meet for the first time the mass-splittings:

$$\Delta m^2_{ij} = m_i^2 - m_j^2 \tag{2.9}$$

We can plot this probability as a function of L/E (Figure 2.1), making the origin of the name "oscillations" more apparent.

Oscillations are therefore a function of the three mixing angles, the distance travelled (often called the baseline) and the neutrino energy. They are also a function of the size of the differences between the mass states, Δm^2_{ij}, which is unsurprising given that it is the *differences* in how the states propagate, and hence their phases, that cause the oscillations. There are three of these mass splittings but since:

$$\Delta m^2_{32} + \Delta m^2_{21} = \Delta m^2_{31} \tag{2.10}$$

Parameter	Value
ϑ_{12}	$33.9 \pm 1.0\,^{\circ}$
ϑ_{23}	$39\,^{\circ} < \vartheta_{23} < 51\,^{\circ}$
ϑ_{13}	$9.1 \pm 0.6\,^{\circ}$
Δm^2_{21}	$(7.50 \pm 0.20) \times 10^{-5}$ eV^2
$\lvert\Delta m^2_{32}\rvert$	$(2.32\ ^{+0.12}_{-0.08}) \times 10^{-3}$ eV^2
δ_{cp}	unknown

Table 2.1: Current world knowledge of the neutrino oscillation parameters [7].

there are only two which are independent. It is also worth emphasizing that it is only the differences between the masses which matter and neutrino oscillations are insensitive to the absolute scale of the three masses.

The Particle Data Group [7] provide a review of current world knowledge of the values of all the fundamental parameters that contribute to neutrino oscillations, which are summarised in Table 2.1.

The equations above all apply to oscillations in a vacuum, however the situation is complicated further when a neutrino beam passes through matter. Because matter contains electrons but none of the other charged leptons/ anti-leptons, ν_e have an additional interaction mode (CC forward scattering) available to them which is unavailable to the other neutrino flavours. This gives a larger effective mass to the ν_e component, which in turn affects the propagation of the associated states and hence the oscillations. The magnitude of the effect increases with the distance travelled in matter and the electron density encountered. Matter effects are not significant in the T2K experiment so won't be discussed in any more depth, but they are important in longer baseline experiments.

Finally, it is possible that there could be more than three neutrino flavour states, though the additional states would have to be "sterile", i.e. not interact via the weak force, or it would conflict with other experimental evidence (the decay width of the Z^0 [11], for example). If this were the case the mixing matrix would have to grow to accommodate it, and there may or may not be more neutrino mass states as well. However at present there is no convincing or consistent evidence to suggest that steriles exist [7].

2.3. Neutrino Masses

In the Standard Model neutrinos have always been treated as massless particles and it is only the discovery of neutrino oscillations which has given us any evidence to suggest otherwise.

The fact that any oscillations occur means that one of the $\Delta m^2_{ij} \neq 0$, implying that at least one of the neutrino masses must also be non-zero. In fact, since all of the mass splittings are measured to be non-zero at least two of the masses are required to be non-zero. However, as discussed in Section 2.2, oscillations are insensitive to the absolute values of the neutrino masses and can only observe the differences between them.

At present the masses have proven to be so small that they are inaccessible to current experiments. The end-point of tritium beta-decay in the Troitzk experiment sets the world's most stringent limit: $m^-_{\nu_e} < 2.05\,\text{eV}$ at 95% CL [12]. Though it should be noted that the mass measured here, $m^-_{\nu_e}$, is that of a flavour state, and therefore represents a combination of the three mass states it contains.

Even with the mass differences we can measure, thus far it has not been possible to determine the sign of Δm^2_{31}. The two possibilities are referred to as the "normal" ($\Delta m^2_{31} > 0$) and "inverted" ($\Delta m^2_{31} < 0$) hierarchies, and amount to a choice between which of the mass states is largest:

$$\begin{aligned} \text{Normal Hierarchy:} &\quad m_3 > m_2 > m_1 \\ \text{Inverted Hierarchy:} &\quad m_2 > m_1 > m_3 \end{aligned} \tag{2.11}$$

The difficulty in determining the sign is essentially caused by the uncertainties on Δm^2_{32} and Δm^2_{31} being larger than the size of Δm^2_{21}, and therefore the sign has a negligible effect on the oscillation probabilities compared to current experimental uncertainties. It is only matter effects in solar neutrino oscillations that have allowed us to determine the sign of Δm^2_{21}.

2.4. Measuring Neutrino Oscillation Parameters

Equation 2.7 tells us that neutrino oscillations depend on the mixing angles, the mass splittings, the distance travelled and the neutrino energy. The mixing angles and mass splittings are properties of the Universe, we can't change them, we can only measure them. The distance travelled in a conventional accelerator-based oscillation experiment is a fixed quantity which we know.

The final parameter, the neutrino energy, is a property of the neutrino source - but that's an oversimplification. There is no practical way to create a mono-energetic neutrino source[3] and in practice experiments produce neutrinos over a range of energies.

The values of the oscillation parameters then, are determined by measuring the E_ν spectrum for a given flavour before and after traversing the baseline. Any deficits/excesses found are the result of oscillations and the energy, size and shape of those changes can be used to measure the oscillation parameters. We can see this by considering the example of an initially pure ν_μ beam, measured after traversing a baseline of 295 km - approximately equivalent to the T2K experiment (Chapter 5)[4].

Determination of the mixing angles comes from measurement of the amplitude of oscillations (Figure 2.2). For example, the value of ϑ_{23} can be determined from the ν_μ spectrum, where the depth of the minimum resulting from oscillations away from ν_μ indicates the size of ϑ_{23}. Likewise, measuring the height of the peak in oscillations to ν_e allows the determination of ϑ_{13}.

The mass splittings on the other hand affect the energy at which these oscillation features occur (Figure 2.3). The value of Δm^2_{32} can be measured from the E_ν of the minimum in the ν_μ spectrum, and the choice of normal

3. There are options for creating mono-energetic neutrinos but none of them are practical. Pion decay at rest would provide a mono-energetic ν_μ source, but their ~30 MeV energy would be too low for ν_μ CC interactions. Alternatively, Z^0 decay at rest would make an interesting neutrino source. Around 20% would decay to give an even mix of all six neutrinos and anti-neutrinos at 45.6 GeV. However the oscillation baseline required for such a high energy would be difficult, and the problems in making a high-flux source from stationary Z^0s are many and large.

4. Unless specified otherwise, for all the plots in this chapter the oscillation parameters are set to the values in Table 2.1, the initial flux is 100% ν_μ and L = 295 km.

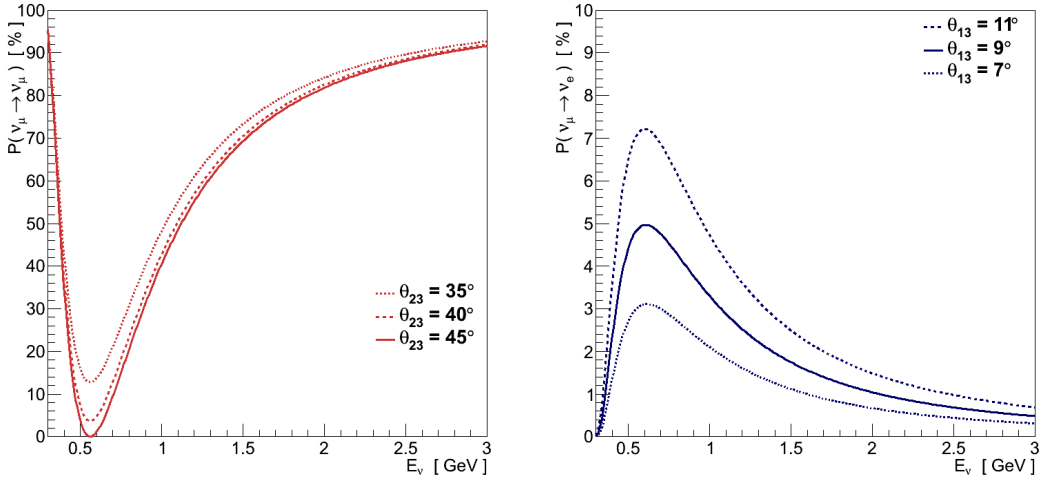

Figure 2.2: (left) The effect of ϑ_{23} on $P(\nu_\mu \rightarrow \nu_\mu)$, its value can be determined by measuring the depth of the minimum. (right) The effect of ϑ_{13} on $P(\nu_\mu \rightarrow \nu_e)$, in this case the value can be determined from the height of the peak.

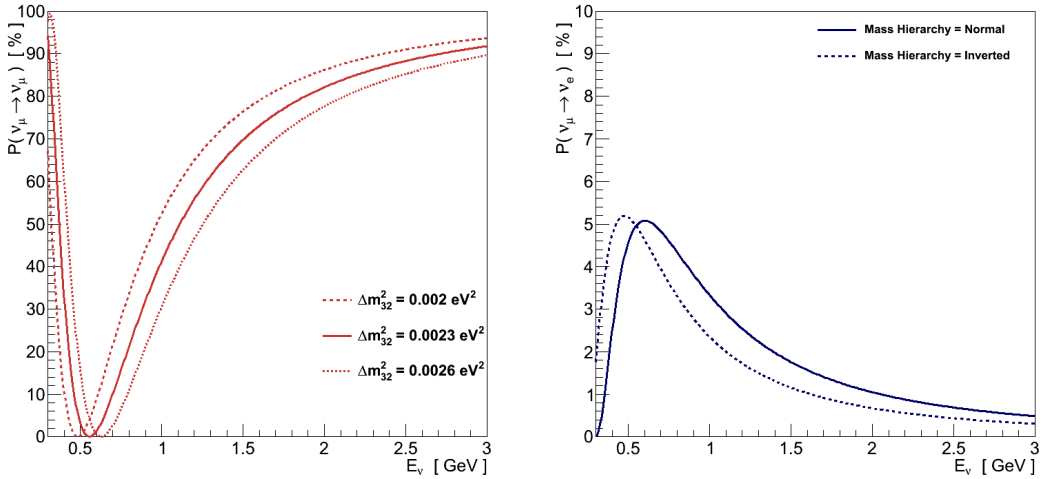

Figure 2.3: (left) The effect of Δm^2_{32} on $P(\nu_\mu \rightarrow \nu_\mu)$, the value can be determined by measuring the energy of the minimum. (right) The dominant effect on the ν_e spectrum of changing the mass hierarchy is a shift of the peak's energy.

or inverted mass hierarchy results in a shift in the E_ν of the peak in the ν_e spectrum.

The long-term goal is to determine whether or not neutrinos violate CP, and perhaps therefore contribute to the matter – anti-matter asymmetry of the Universe. In other words, to measure the value of δ_{cp}.

While the other oscillation parameters tend to affect one or other of the amplitude or energy of oscillations, δ_{cp} affects both (Figure 2.4). As the value

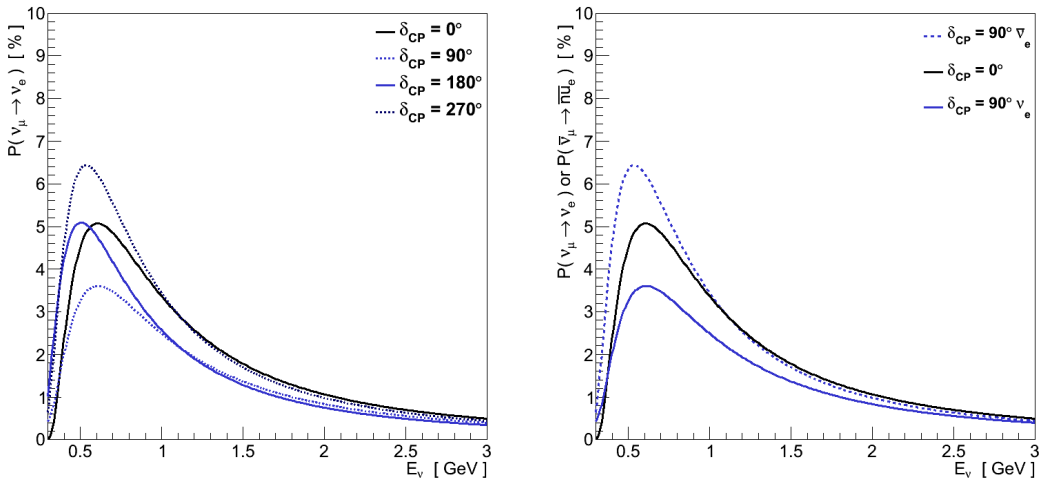

Figure 2.4: The effect of δ_{cp} on $P(\nu_\mu \rightarrow \nu_e)$. (left) As you rotate the angle of δ_{cp}, the position of the peak follows a circular path, changing both its height and energy. (right) The peak for $P(\bar{\nu}_\mu \rightarrow \bar{\nu}_e)$ follows the same circular path, but in the opposite direction.

of δ_{cp} is rotated, the position of the ν_e peak varies both in height and energy, traversing a circular path which reaches extremes in amplitude at $\delta_{cp} = 90/270\,^\circ$ and energy at $\delta_{cp} = 0/180\,^\circ$. It also affects ν_e and $\bar{\nu}_e$ differently, with $\bar{\nu}_e$ traversing the same circular path but in the opposite direction. Looking at lower E_ν (Figure 2.5), equivalent to higher L/E_ν, there are additional oscillation peaks which are much more strongly affected by the value of δ_{cp}.

This leaves three ways through which such an experiment could determine δ_{cp}: a precise measurement of the position of the first peak in $P(\nu_\mu \rightarrow \nu_e)$ spectrum, a comparison of that peak in neutrino and anti-neutrinos or, if the experiment is capable of resolving it, measuring the position of the second $P(\nu_\mu \rightarrow \nu_e)$ peak.

However, determining the value of δ_{cp} through any of these methods will be particularly challenging. Because they only interact weakly, experiments cannot observe neutrinos directly. Instead, they only observe them via the secondary particles produced when they interact. In order to determine the proportion of neutrinos of a given flavour, the experiment must measure the number of events in which the corresponding charged lepton is produced, then use knowledge of the probability of that neutrino interacting to infer the number of neutrinos that actually passed through the detector. In order to measure the energy of the neutrino, the experiment must infer it from measurements of the secondary particles produced, and an understanding of how the neutrino's interaction produced these particles.

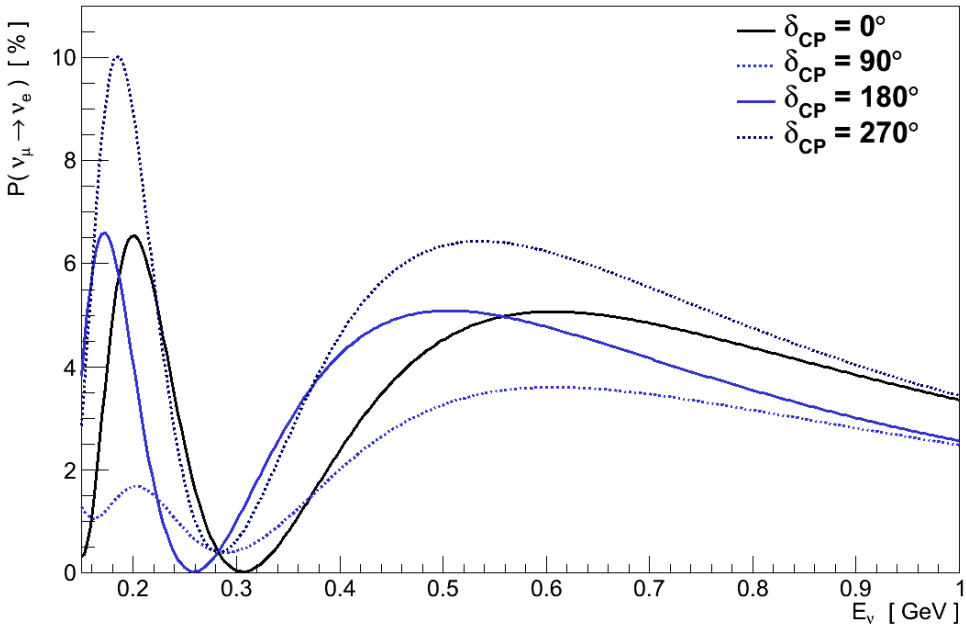

Figure 2.5: The effect of δ_{cp} on $P(\nu_\mu \rightarrow \nu_e)$. If an experiment can resolve the second oscillation maximum at lower E_ν, the effects of δ_{cp} can be much larger.

Not understanding the probability of a given neutrino flavour interacting will lead to incorrectly determining the number of those neutrinos present, and hence the oscillation probability. Not understanding the kinematics of secondary particles produced by a neutrino's interaction, will result in the energy being mis-reconstructed, and hence the neutrino energy spectrum being distorted. So in order to make precise measurements of the oscillation parameters, a precise understanding of neutrino interactions is needed.

This is particularly true for the determination of δ_{cp}. The variations in the height and position of the ν_e peak resulting from changes in δ_{cp} could also be attributed to changes in the values of the mixing angles and mass-splittings. And the size of those variations resulting from δ_{cp} are much smaller in scale than the current precision in those parameters will allow us to resolve. Furthermore, neutrinos and anti-neutrinos have quite different interaction probabilities, and result in a different range of secondary particles.

So our ability to measure δ_{cp} is limited by the need for precise knowledge of the other oscillation parameters, and of the interactions of neutrinos and anti-neutrinos. The precision of our knowledge of the other oscillation parameters, is also limited by our understanding of neutrino interactions, and how they relate to the energy and number of neutrinos in our experiment.

In order to increase the precision to which we understand neutrino oscillations, measure δ_{cp}, and perhaps solve the matter – anti-matter asymmetry of the Universe, we must first understand neutrino interactions.

3. Neutrino Interactions

As electrically-neutral and un-coloured particles the only Standard Model interactions available to neutrinos are those of the weak force, as a result of which it is impossible to directly observe the path of a neutrino through a detector. This fact, coupled with the small cross-sections typical of the weak interaction at low energy, makes the study of neutrino interactions a challenging task. However, since we rely on our understanding of neutrino interactions to infer the number, type, direction and energy of the neutrinos in experiments, it is essential to study them before precision measurements of neutrino oscillations can be achieved.

Though a discussion of neutrino interaction simulations will be left until Section 3.8 it should be noted that in this chapter, all of the cross-section predictions shown are those implemented in the neutrino interaction simulation GENIE (version 2.8.0), and experimental data are those digitised for, and distributed as part of, GENIE's built-in validation.

3.1. Weak Interactions

The weak force through which neutrinos interact has two forms: charged-current (CC) interactions mediated by the $W^{\pm}$ bosons, and neutral-current (NC) interactions mediated by the Z^0 boson. Their respective currents are [13]:

$$\begin{aligned} j_{\mu}^{\pm} &= \overline{u}\frac{-ig_W}{2\sqrt{2}}\Big(\gamma^{\mu}-\gamma^{\mu}\gamma^5\Big)u \\ j_{\mu}^{0} &= \overline{u}\frac{-ig_Z}{2}\Big(g_V\gamma^{\mu}-g_A\gamma^{\mu}\gamma^5\Big)u \end{aligned} \tag{3.1}$$

Where u and $\overline{u}$ are Dirac spinors, γ^{μ} are the four Dirac gamma matrices, $\gamma^5 = i\gamma^0\gamma^1\gamma^2\gamma^3$, and g_W and g_Z are coupling-strengths.

In these expressions both the charged- and neutral-current interactions can be seen to be a mixture of two components: γ^{μ} and $\gamma^{\mu}\gamma^5$. One of the key

Particles	$\mathbf{g_V}$	$\mathbf{g_A}$
Neutrinos	$\frac{1}{2}$	$\frac{1}{2}$
Charged Leptons	$\frac{1}{2} + 2\sin^2\vartheta_W$	$-\frac{1}{2}$
Up-type Quarks	$\frac{1}{2} - \frac{4}{3}\sin^2\vartheta_W$	$\frac{1}{2}$
Down-type Quarks	$-\frac{1}{2} + \frac{2}{3}\sin^2\vartheta_W$	$-\frac{1}{2}$

Table 3.1: Weak NC vector and axial-vector vertex factors.

distinctions between these two components is how they behave under parity transformations (the operation of inverting all three spatial co-ordinates):

$$\begin{aligned} \text{even parity:} \quad & \hat{P}\left(\overline{\psi}\, \gamma^{\mu}\gamma^{5}\psi \right) = \overline{\psi}\, \gamma^{\mu}\gamma^{5}\psi \\ \text{odd parity:} \quad & \hat{P}\left(\overline{\psi}\, \gamma^{\mu}\psi \right) = -\left(\overline{\psi}\, \gamma^{\mu}\psi \right) \end{aligned} \tag{3.2}$$

Ordinary three-vectors acquire a minus sign under parity transformations hence γ^{μ}, which has odd parity, is referred to as a "vector" current. In contrast $\gamma^{\mu}\gamma^{5}$ is even under parity and hence is referred to as a "pseudo-vector" or, more commonly in weak interactions, "axial-vector" current (in analogy to angular-momentum vectors which are parity even). One consequence of mixing both odd and even currents is that the parity of a system is not conserved by the weak force - parity violation (though this is neither necessary nor sufficient for CP violation).

The Standard Model relates the coupling strengths of the two interactions in Equation 3.1, g_W and g_Z, to the weak mixing angle, ϑ_W:

$$\frac{g_W}{g_Z} = \cos\vartheta_W \tag{3.3}$$

However it does not predict the values for any of these parameters which must be determined empirically: $\vartheta_W = 28.7^\circ$, $g_W = 0.653$ [14]. The weak mixing angle also determines the values of the vector (g_V) and axial-vector (g_A) couplings in the NC vertex factor, which are particle dependent and shown in Table 3.1.

Writing the weak interaction in the form shown in Equation 3.1 emphasises its behaviour under parity transformations. But it is also common to see it in an alternative form:

$$j_{\mu}^{\pm} = \overline{u}\,\frac{-ig_W}{2\sqrt{2}}\gamma^{\mu}\Big(1 \pm \gamma^5\Big)u \tag{3.4}$$

This form emphasises the weak force's chiral nature. Chirality is an abstract property of particle spinors which is a Lorentz invariant but not constant in time. Eigenstates of chirality can be either "left-" or "right-handed", defined by the chirality operator γ^5 with eigenvalues -1 (left-handed) or +1 (right-handed). In general particle spinors are composed of both left- and right-handed chiral components:

$$u = u_L + u_R \tag{3.5}$$

which can be separated out using the chiral "projection" operators:

$$\begin{array}{cc} \text{Particles} & \text{Anti-Particles} \\ u_L = \tfrac{1}{2}\Big(1-\gamma^5\Big)u & v_L = \tfrac{1}{2}\Big(1+\gamma^5\Big)v \\ u_R = \tfrac{1}{2}\Big(1+\gamma^5\Big)u & v_R = \tfrac{1}{2}\Big(1-\gamma^5\Big)v \\ \overline{u}_L = \overline{u}\,\tfrac{1}{2}\Big(1+\gamma^5\Big) & \overline{v}_L = \overline{v}\,\tfrac{1}{2}\Big(1-\gamma^5\Big) \\ \overline{u}_R = \overline{u}\,\tfrac{1}{2}\Big(1-\gamma^5\Big) & \overline{v}_R = \overline{v}\,\tfrac{1}{2}\Big(1+\gamma^5\Big) \end{array} \tag{3.6}$$

We can now see that Equation 3.4 contains the chiral projection operator, and using some gamma-matrix algebra[1] we can re-write the negative current of Equation 3.4:

$$j_{\mu}^{-} = \frac{-ig_W}{2\sqrt{2}}\,\overline{u}\,\Big(1+\gamma^5\Big)\gamma^{\mu}\Big(1-\gamma^5\Big)u = \frac{-ig_W}{2\sqrt{2}}\,\overline{u}_L\gamma^{\mu}u_L \tag{3.7}$$

Written this way, CC weak interactions can be viewed as a purely vector current interacting only with the left-handed chiral component of a particle, or

1. $(1 - \gamma^5)^2 = 2(1 - \gamma^5)$, $\gamma^{\mu}(1 - \gamma^5) = \frac{1}{2}(1 + \gamma^5)\gamma^{\mu}(1 - \gamma^5)$.

right-handed chiral component of an anti-particle. The analogous form for NC interactions leads to the same conclusion in the case of neutrinos, and since neutrinos can only be created via the weak force, we can conclude that they are always created in a left-handed chiral eigenstate.

In the case of massless particles, chirality becomes identical to helicity (the projection of a particle's spin onto its momentum). In contrast to chirality, helicity is constant in time but not Lorentz invariant. As a result, when helicity and chirality become equivalent, they are both Lorentz and time invariant. A massless particle with left-handed chirality also has left-handed helicity, and that cannot change. Because neutrinos were historically thought to be massless, this often lead to the statement that right-handed chiral neutrinos did not exist. But since they are now known to be massive this is no longer true. Even though they can still only be created in a left-handed chiral state, they will gradually evolve a right-handed chiral component. Such a right-handed component is sterile[2] - unable to interact via either the CC or NC weak interactions - but it does exist.

Nonetheless, the fraction of "wrong" sign chiral state present is proportional to m_ν/E_ν [7] and hence is sufficiently small that it is experimentally negligible. This has been confirmed in electron capture experiments, which deduced the helicity of the ν_e from the measured polarisation of a de-excitation photon emitted back-to-back with the neutrino [15]. Within experimental resolution, all the neutrinos had left-handed helicity.

The final ingredient for weak interaction calculations are the propagators associated with the weak bosons [13]:

$$\frac{-i\left(g_{\mu\nu} - \frac{q_\mu q_\nu}{M^2}\right)}{q^2 - M^2} \tag{3.8}$$

where M is the mass of the relevant boson and q the four-momentum it's transferring. However, when $q^2 \ll M$ this can be reduced to:

$$\frac{ig_{\mu\nu}}{M^2} \tag{3.9}$$

2. Strictly, this is not true for Majorana neutrinos, then the right-handed chiral component is the anti-neutrino.

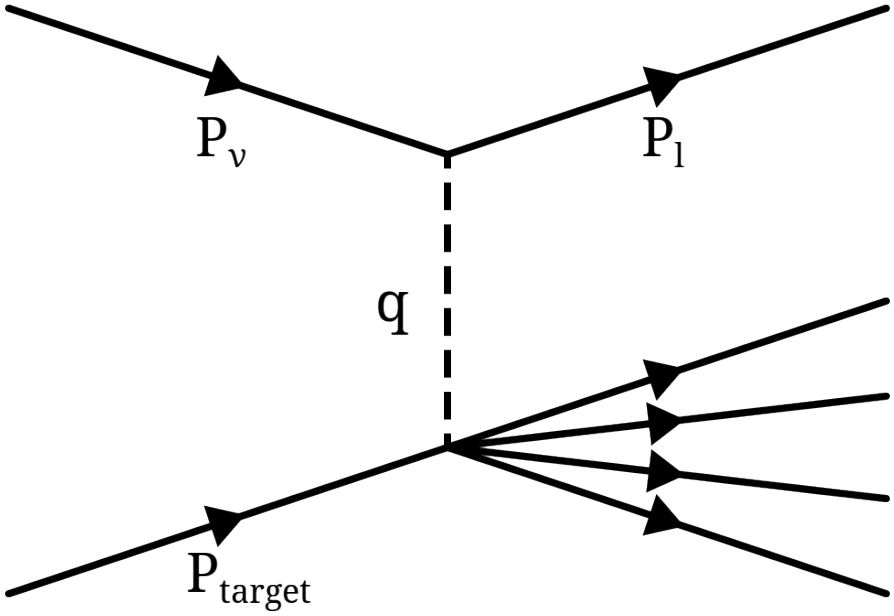

Figure 3.1: Diagram of a generic neutrino interaction with a target, leaving a (charged or neutral) final-state lepton and an unspecified system of final-state particles.

Since $M_W \approx 80\,\text{GeV}$, $M_Z \approx 91\,\text{GeV}$ and all existing neutrino beamline experiments are run at $E_\nu < 100\,\text{GeV}$ it will be safe to assume that this is always the case.

3.2. Conventional Notation

Before proceeding with a discussion of the various interactions which a neutrino can undergo, it is useful to introduce the conventional notation used within the field. Figure 3.1 shows a view of a generic neutrino interaction with a target, generating a final-state lepton l (which could be either a charged or neutral lepton depending on the weak current involved) and an unspecified system of other final-state particles.

The four-momentum transferred between the neutrino-lepton system and the target system is denoted q and, as is expected for a four-vector, the square of this transfer, q^2, is a Lorentz invariant. Because q^2 is usually negative, it is common to see $Q^2 = -q^2$ used instead. Although the total cross-section for a

neutrino interacting is a function of its energy, it is Q^2 that determines what features of the target are resolved, and what final-states are available as a result of the interaction. However, since the Q^2 available to an interaction is strongly dependent on the neutrino's energy, this distinction is often not made explicit.

There are three other Lorentz invariants commonly used to characterise interactions [16], the first being the inelasticity, y:

$$y = \frac{q \cdot P_{\text{target}}}{P_{\nu} \cdot P_{\text{target}}} \tag{3.10}$$

In the target's rest frame this is more simply:

$$y = \frac{q_0}{E_{\nu}} = \frac{E_{\nu} - E_l}{E_{\nu}} \tag{3.11}$$

allowing the inelasticity to be interpreted as the fraction of the initial neutrino's energy transferred by the interaction. While inelasticity is defined for all neutrino interactions, the remaining Lorentz invariants are reserved for neutrino interactions where the target is a nucleon or nucleus. The Bjorken scaling variable, x:

$$x = \frac{-q^2}{2P_{\text{target}} \cdot q} \tag{3.12}$$

is most commonly used for deep inelastic scattering (Section 3.5.3), where it is roughly equivalent to the fraction of the target nucleon's momentum carried by the quark which was struck. Deep inelastic scattering is characterised by lower-x interactions than are found in more inelastic interactions (where $x \approx 1$). Finally, the invariant hadronic mass, W:

$$W = \sqrt{\left(q + P_{\text{target}}\right)^2} \tag{3.13}$$

represents the total invariant mass of the outgoing particle system, with the exception of the lepton, and is useful for characterising the final-states available to that system.

The inelasticity, Bjorken scaling variable and invariant hadronic mass are convenient because they can be more directly inferred from measurements of final-state particles, and can highlight characteristic features of the interactions.

With the conventional formalism for the weak interaction and neutrino scattering introduced, the various processes available to neutrinos in experiments can now be discussed. The simplest of these, inverse muon decay and electron elastic scattering, utilise electrons as their targets. At the cost of increased theoretical complexity, nucleon targets provide more interaction modes and higher cross-sections, making them more practical for use in oscillation experiments. However, the fact that these target nucleons are usually bound within nuclei significantly affects both the interactions and their appearance in experiments.

3.3. Inverse Muon Decay

One of the simplest neutrino interactions to consider is the CC scattering of a ν_μ off of a free electron. This is often referred to as "inverse muon decay" and is simple in that it involves only fundamental particles and just one diagram at tree-level (Figure 3.2). The same interaction is also possible for ν_τ, though in both cases E_ν must be above the threshold required to provide the mass of the corresponding charged lepton:

$$E_\nu \geq m_l - m_e \tag{3.14}$$

Using the ingredients from the start of the chapter, the amplitude for this interaction is then:

$$\mathcal{M} = \frac{{g_W}^2}{8{M_W}^2}\left[\overline{u}_3\left(\gamma^\mu - \gamma^\mu\gamma^5\right)u_1\right]\left[\overline{u}_4\left(\gamma_\mu - \gamma_\mu\gamma^5\right)u_2\right] \tag{3.15}$$

Averaging over incoming spin states, summing over outgoing spin states, and requiring that the neutrinos have only left-handed helicity (making the $m_\nu \approx 0$ assumption) we have:

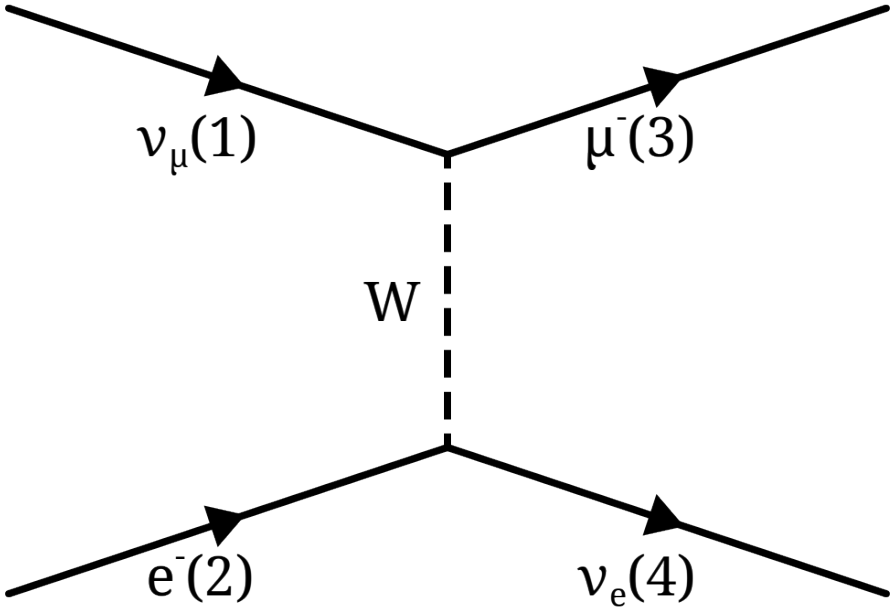

Figure 3.2: Feynman diagram of "inverse muon decay": the CC scattering of a ν_μ off of a free e^-.

$$\left\langle \left| \mathscr{M} \right|^2 \right\rangle = 2\left(\frac{g_W}{M_W}\right)^4 \left(p_1 \cdot p_2\right)\left(p_3 \cdot p_4\right) \tag{3.16}$$

If the kinematics of the interaction are now specified, the cross-section can be calculated. For example, in the centre-of-mass frame, neglecting the electron and neutrino masses, the cross-section is [13]:

$$\sigma = \frac{1}{8\pi} \frac{{g_W}^4 {E_\nu}^2}{{M_W}^4} \left(1 - \frac{{m_\mu}^2}{4{E_\nu}^2}\right)^2 \tag{3.17}$$

Before weak interactions were understood, Enrico Fermi suggested a theory of beta decay which treated it as a single four-particle vertex [17]. It turns out that this is a good approximation at low energies due to the large mass of the $W^\pm$ and it is still common to see weak interactions calculated using Fermi's coupling:

$$\frac{G_F}{\sqrt{2}} = \frac{{g_W}^2}{8{M_W}^2} \tag{3.18}$$

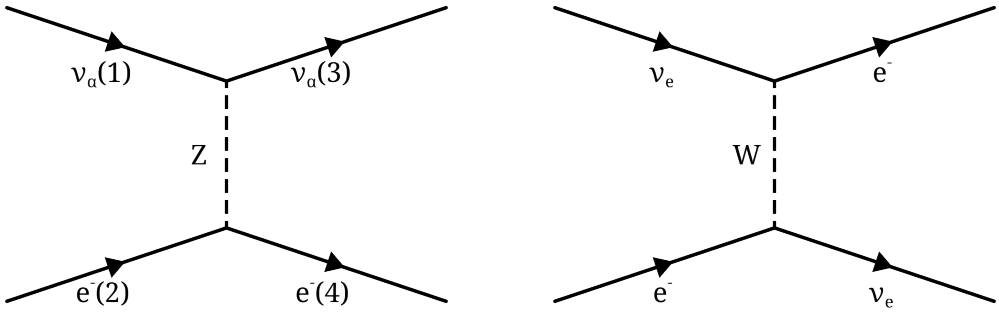

Figure 3.3: Feynman diagrams for electron elastic scattering. (left) All three neutrino flavours ($\alpha = e, \mu, \tau$) can undergo NC scattering off an electron. (right) For ν_e there is an additional CC mode.

3.4. Electron Elastic Scattering

The simplest NC neutrino interaction that can be considered is that of NC electron elastic scattering, where an incoming neutrino interacts with a free electron causing the electron to recoil but leaving no other experimental signatures (Figure 3.3).

The situation is complicated somewhat for ν_e due to an additional CC contribution to the process. It is this difference with respect to ν_μ and ν_τ which results in the matter effects discussed in Section 2.2.

Since there is no change in mass this is a threshold-less interaction. The basic amplitude for the NC process is:

$$\mathscr{M} = \frac{g_Z^2}{4M_Z^2}\left[\overline{u_3}\left(g_V^\nu \Upsilon^\mu - g_A^\nu \Upsilon^\mu \Upsilon^5\right)u_1\right]\left[\overline{u_4}\left(g_V^e \Upsilon_\mu - g_A^e \Upsilon_\mu \Upsilon^5\right)u_2\right] \tag{3.19}$$

Which, averaged over incoming spin states, summed over outgoing spin states, and neglecting the neutrino and electron masses in the centre-of-mass frame gives a cross-section [13]:

$$\sigma = \frac{2}{3\pi}\frac{g_Z^4 E_\nu^2}{M_Z^4}\left(g_V^{e\,2} + g_A^{e\,2} + g_V^e g_A^e\right) \tag{3.20}$$

approximately 9% of the cross-section for inverse muon decay.

3.5. Neutrino-Nucleon Interactions

While less easy to deal with theoretically, nucleons provide a neutrino target with much larger cross-sections and a more diverse range of processes through which to interact. Broadly, these processes can be put into two categories: elastic and inelastic. Elastic interactions dominate at small Q^2 and are characterised by the struck nucleon recoiling from the interaction intact, though in the CC case there is also a change of charge. CC interactions are also more correctly referred to as "quasi-elastic", due to the transfer of mass to the final-state lepton.

In inelastic interactions, the low Q^2 region is dominated by resonance production - where the nucleon is excited into a baryonic resonance, for example a Δ, before decaying. At high Q^2, inelastic scattering is dominated by deep inelastic scattering (DIS) - where the neutrino scatters directly off a constituent quark, fragmenting the original nucleon. In between these extremes exists a messy region, where neither resonance nor DIS dominate, and additional contributions come from interactions where the hadronic system is neither completely fragmented nor forms a recognisable resonance. These interactions are sometimes referred to as "shallow inelastic scattering", and there is no clear model for dealing with them[3].

The overall picture is one where both the NC and CC total neutrino-nucleus cross-sections rise linearly above around 10 GeV (Figure 3.4). At these energies interactions are almost completely the result of DIS. At lower energies, elastic interactions dominate below 1 GeV, with a transition region in between where the relative fractions of each channel vary rapidly (Figure 3.5).

Making calculations for the interactions of neutrinos with nucleons presents additional complexity over electrons since they are compound particles. The Standard Model does not have a prescription to describe such a compound particle directly, and we are not currently capable of calculating it from its constituents. Although essentially composed of only three quarks, they are constantly interacting via gluon exchanges which in turn can produce other temporary quark/anti-quark pairs. It is the average of this activity which is seen by the weak interaction, so we require some mechanism to describe the effect this has. The four-momentum of the weak boson determines how much

3. The approach used in GENIE is to scale components of the DIS cross-section below $W = 1.7$ GeV, such that the total inelastic cross-section matches existing data.

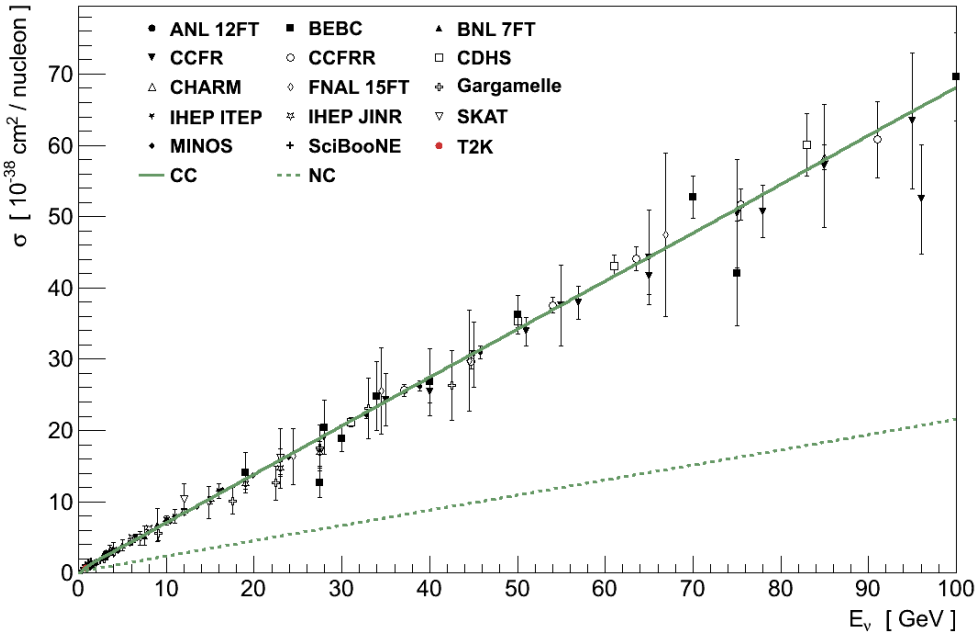

Figure 3.4: The total ν_μ CC and NC cross-sections on deuterium as a function of neutrino energy (lines), compared with data on ν_μ CC from a variety of targets.

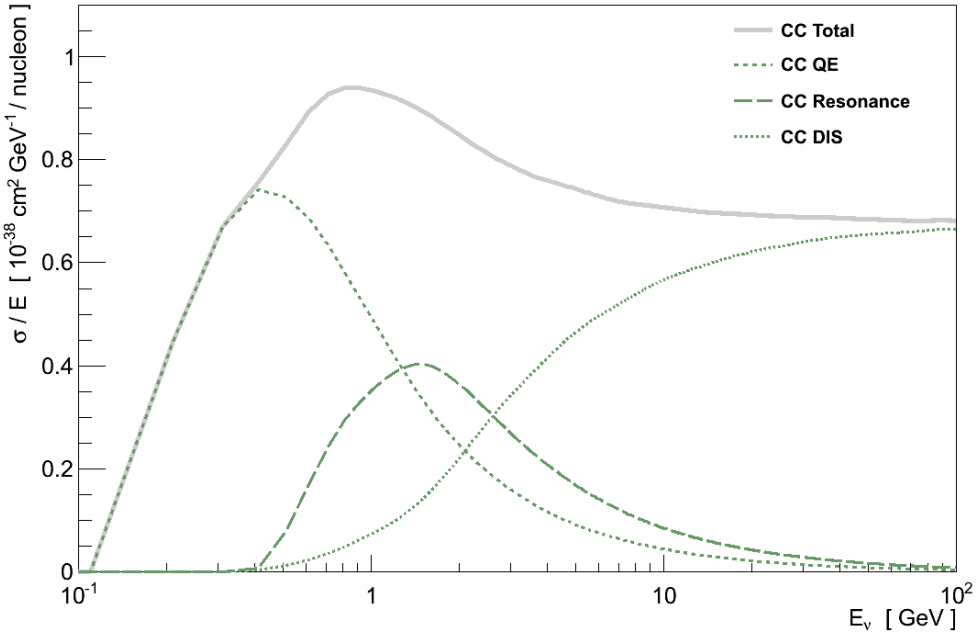

Figure 3.5: σ/E_ν for total ν_μ CC interactions, and the three major components: CC QE, resonance and DIS.

of the nucleon's internal structure is resolved by a weak interaction, so that mechanism will in general be a function of Q^2.

For a fixed value of Q^2, one simple approach is to treat the nucleon in the same manner as a fundamental fermion, but substitute two experimentally determinable parameters into the vertex factor:

$$\left(\gamma^\mu - \gamma^\mu\gamma^5\right) \rightarrow \left(c_V\gamma^\mu - c_A\gamma^\mu\gamma^5\right) \tag{3.21}$$

At $Q^2 \approx 0$, the values of these parameters can be measured from neutron (beta) decays within atoms. The vector parameter is measured as $c_V = 1.0$, implying the vector part of the neutron is unaltered (conserved) by the strong interactions within, a conclusion known as the "conserved vector current" (CVC). Meanwhile $c_A = 1.270 \pm 0.003$ [18] implying even the axial-vector part is only slightly affected, a conclusion referred to as the "partially conserved axial-vector current" (PCAC).

This approach is not suitable in general as the nucleon structure which can be resolved, and hence the values of c_V and c_A, is a function of Q^2. It works well for low Q^2 processes, such as neutron decay, where the parameters approach a constant, but a more thorough approach is required for neutrino scattering in oscillation experiments.

The approach generally taken is to represent a nucleon (hadronic) current by generic vector, axial-vector and isoscalar currents [16] [18]:

$$H_\mu^{CC} = V_\mu^\pm + A_\mu^\pm \tag{3.22}$$

$$H_\mu^{NC} = \left(1 - 2\sin^2\vartheta_W\right)V_\mu^0 + A_\mu^0 - 2\sin^2\vartheta_W V_\mu^S \tag{3.23}$$

where V_μ, A_μ and $V^S{}_\mu$ are the vector, axial-vector and isoscalar currents respectively. These currents are in turn composed of several "form-factors": phenomenological functions of Q^2 representing the different terms which could contribute. The selection of form-factors which are required is interaction dependent, as are the functions used to describe them. Sometimes the form-factors can be related to analogous interactions from other nucleon scattering fields (electron scattering in particular), though there are others which can only be determined from neutrino scattering.

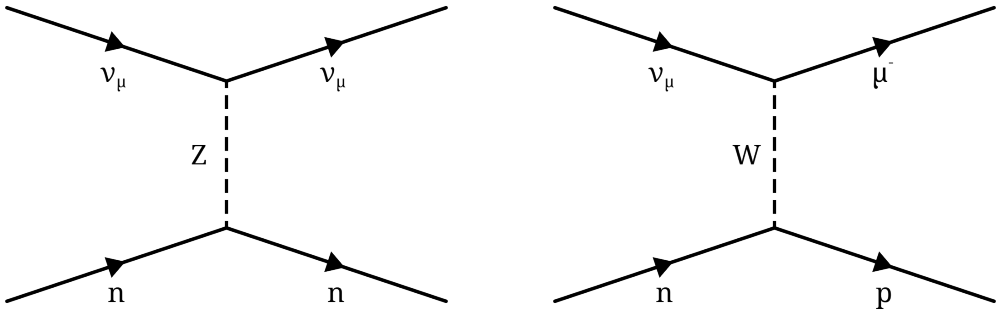

Figure 3.6: (left) An example Feynman diagram of NC elastic scattering by a ν_μ on a neutron. (right) Feynman diagram for ν_μ CC QE scattering.

3.5.1. NC Elastic & CC Quasi-Elastic Scattering

Beginning at the lowest neutrino energies the first nucleon interactions available to neutrinos are ones in which the nucleon recoils intact (Figure 3.6). When this occurs via the NC, all neutrinos and anti-neutrinos can scatter off both neutrons and protons in what is referred to as "NC elastic" scattering: $\nu + N \rightarrow \nu + N$.

Once neutrinos acquire sufficient energy they can also undergo the analogous CC interactions: $\nu_l + n \rightarrow p + l^-$ and $\bar{\nu}_l + p \rightarrow n + l^+$. Because of the need to create the charged lepton's mass this is referred to as "quasi-elastic" scattering (CC QE). For ν_μ with $E_\nu < 1$ GeV CC QE is the dominant interaction, however the cross-section plateaus at higher E_ν as the available Q^2 increases and it becomes increasingly unlikely for the nucleon to remain intact (Figure 3.7).

CC QE interactions are particularly important to neutrino physics for two reasons. First, because the nucleon recoils intact they are the best interaction with which to measure weak nucleon form-factors which are difficult or inaccessible for other scattering probes (such as those relating to the axial-vector).

Second, their nature as two-body interactions enable the kinematics to be completely reconstructed, and hence the initial neutrino energy determined which, as discussed in Chapter 2, is critical for measuring the oscillation parameters. In fact if the target nucleon is at rest, or E_ν is large enough for this to be a reasonable approximation, then just the momentum (p_l) and angle with respect to the neutrino (ϑ_l) of the outgoing charged lepton is sufficient to calculate E_ν:

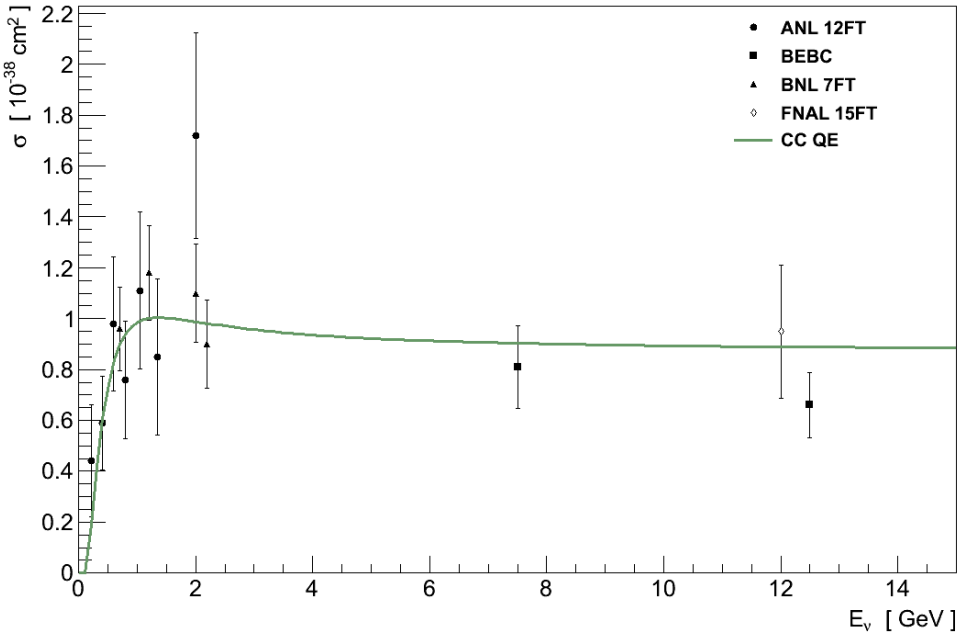

Figure 3.7: The ν_μ CC QE cross-section on deuterium, as implemented in GENIE (line) and measured in data (points).

$$E_\nu = \frac{m_n E_l + \frac{1}{2}\left(m_p{}^2 - m_n{}^2 - m_l{}^2\right)}{m_n - E_l + p_l \cos\vartheta_l} \tag{3.24}$$

However, as we will see in Section 3.6, both of these uses for CC QE are significantly complicated when the nucleon is within a nuclear environment.

To calculate the cross-section only the vector and axial-vector currents are required, since this is a CC interaction (Equation 3.22), the simplest forms[4] for which are:

$$V^a_\mu = \left[\gamma_\mu F_1 + \frac{i\sigma_{\mu\nu}q^\nu}{2m_N}F_2\right]\frac{\tau^a}{2} \tag{3.25}$$

$$A^a_\mu = \left[\gamma_\mu\gamma_5 F_\mathrm{A} + \frac{q_\mu\gamma_5}{m_N}F_\mathrm{P}\right]\frac{\tau^a}{2} \tag{3.26}$$

4. There are additional possible form-factors relating to so-called "second-class current" which, if they exist, could become relevant at low E_ν [19].

where a = ±,0 indicates the relevant change of nucleon-isospin, τ^a are the corresponding Pauli-matrices, m_N is the average nucleon mass and $\sigma_{\mu\nu} = \frac{1}{2}i[\gamma_\mu,\gamma_\nu]$.

The first two form-factors, F_1 and F_2, are vector form-factors which, as a consequence of CVC, can be measured in electro-magnetic interactions such as electron-nucleon scattering. For the axial form-factor, F_A, it is common to assume a "dipole" form:

$$F_A\left(q^2\right) = \frac{F_A(0)}{\left(1+\frac{Q^2}{{M_A}^2}\right)^2} \tag{3.27}$$

where the two controlling parameters must be determined experimentally: $F_A(0) = -c_A = -1.27$ from β-decay, and the "axial mass" $M_A = 1.014 \pm 0.014$ GeV from CC QE neutrino scattering on deuterium and pion production by electrons [20]. It should be noted though that the dipole form is an assumption. Although, to date, neutrino experiments do not have the precision required to test this, in electron scattering measurements of the electro-magnetic form-factors it has been found that a dipole form is a good approximation but not a precise description [20].

Finally the pseudo-scalar form-factor, F_P, can be related to F_A via the "Goldberger-Treiman relation" [16]:

$$F_P = \frac{2{m_N}^2}{{m_\pi}^2 + Q^2} F_A \tag{3.28}$$

To date CC QE interactions have exclusively been described by the Llewellyn-Smith model [21] which provides both a model with which to calculate the cross-section, and a formalism for separating out the form-factors to be determined in experiments:

$$\frac{\mathrm{d}\,\sigma}{\mathrm{d}\,Q^2} = \frac{{g_W}^4 \quad {m_N}^2}{8{M_W}^2\, 32\pi {E_\nu}^2}\left(A\left(Q^2\right) + \frac{B\left(Q^2\right)}{{m_N}^2}(s-u) + \frac{C\left(Q^2\right)}{{m_N}^4}(s-u)^2\right) \tag{3.29}$$

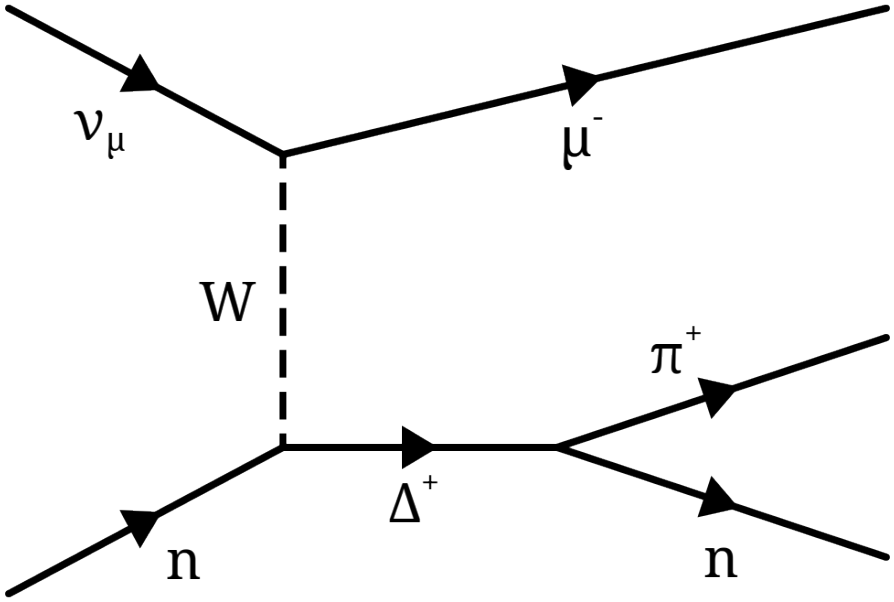

Figure 3.8: Feynman diagram for an example of resonance: ν_μ CC resonance single-pion interaction.

Where $A(Q^2)$, $B(Q^2)$, $C(Q^2)$ are functions of the various form-factors, and s, u are the usual Mandelstam variables.

3.5.2. Resonance Production

At higher energies, with more Q^2 available, neutrinos gain access to inelastic scattering processes. Although the lepton side of these interactions looks the same, on the hadronic side the target nucleon is "knocked" into a baryonic resonance, for example an N* or Δ, the available resonances being determined by the neutrino's energy (e.g. Figure 3.8).

These resonances then decay back down to a nucleon, most often accompanied by a single pion. However a variety of final-states can result depending on the resonance and can include multiple pions, kaons or a radiative photon.

The most common result of resonance decay is single-pion production, for which a model by Dieter Rein and Lalit Sehgal [22] has been the common framework used by experiments and simulations. In it, the production of 18 resonances below 2.0 GeV are described along with interferences in the

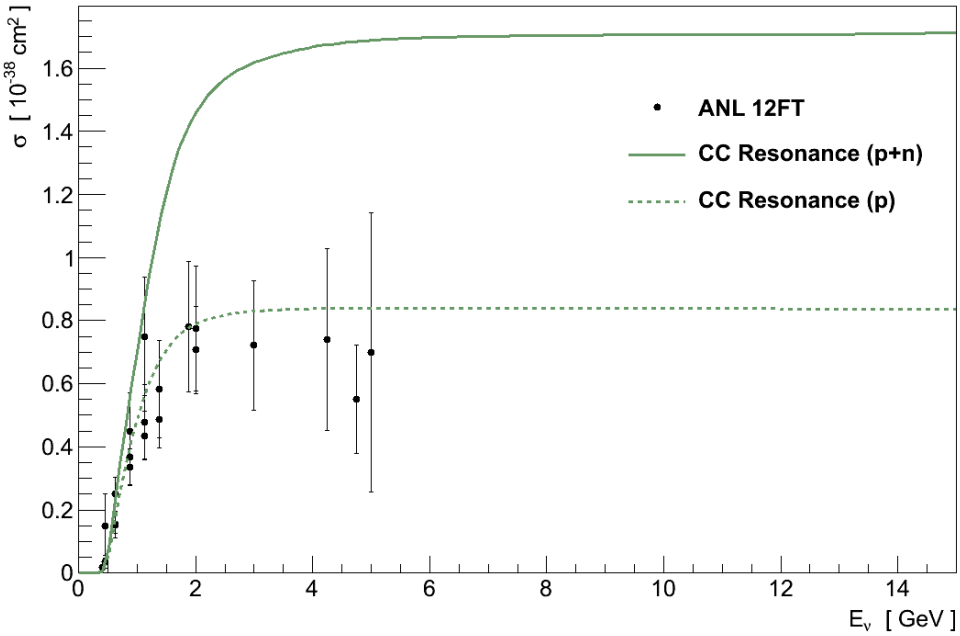

Figure 3.9: Cross-sections for ν_μ CC resonance single-pion production on deuterium. The total cross-section (solid) is shown alongside the proton-only cross-section (dashed) for comparison with data on ν_μ p $\rightarrow$ μ^- p π^+ (points).

regions where they overlap. The CC cross-section predicted from this model, as implemented in GENIE, is shown in Figure 3.9.

All combinations of neutrinos and anti-neutrinos, scattering off neutrons and protons, via charged- or neutral-current, which obey charge conservation can occur. For example, CC single π^+ production can occur on both neutrons ($\nu_l\ n \rightarrow l^-\ n\ \pi^+$) and protons ($\nu_l\ p \rightarrow l^-\ p\ \pi^+$):

Resonance production is most significant in the transition region between CC QE and DIS dominance, $0.5\,\text{GeV} < E_\nu < 10\,\text{GeV}$, above which it plateaus like CC QE. It is of particular interest for neutrino oscillation experiments searching for ν_e, since the signal produced by $\pi^0 \rightarrow 2\gamma$ can easily mimic an electron.

3.5.3. Deep Inelastic Scattering

At even higher energies the neutrino is able to transfer sufficient momentum that the internal structure of the nucleon can be resolved. Now neutrinos can

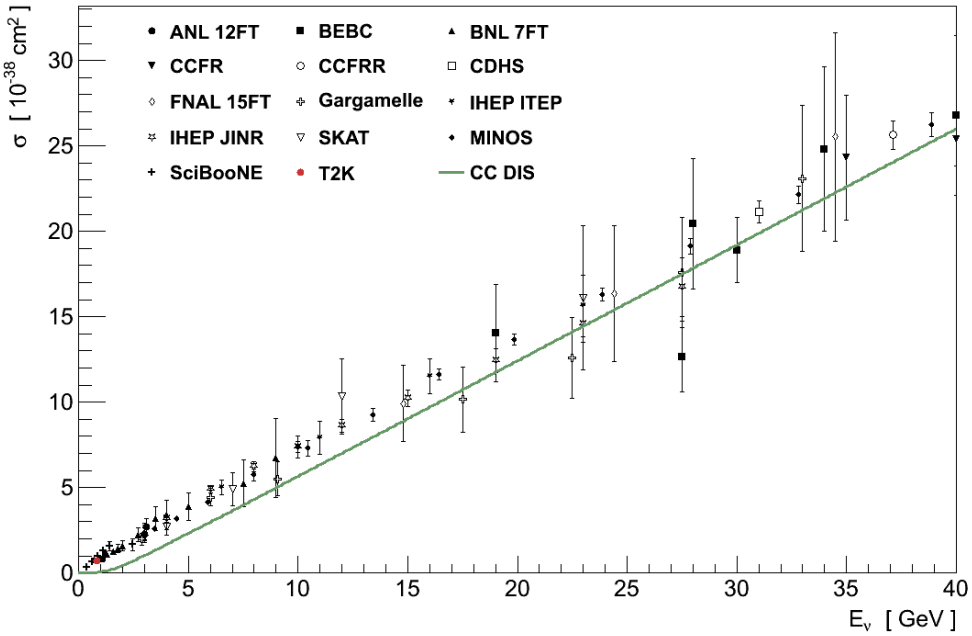

Figure 3.10: The ν_μ CC DIS cross-section on deuterium (line). Data on the total inclusive ν_μ CC cross-section measured on multiple targets is shown for comparison (points). As the neutrino energy increases DIS starts to dominate and approaches the total cross-section.

scatter directly off the quarks inside in a process known as deep inelastic scattering (DIS). The neutrino can scatter off any of the quarks that appear inside the nucleon, including those which form the "sea" of quarks and anti-quarks that are constantly popping in and out of existence. Which of these the neutrino can see depends on the four-momentum transfer available: at lower values the nucleons contain mostly up, down and some strange quarks, but higher values can access the higher-mass and shorter-lived quarks too.

The most visible consequence of DIS is the break up of the nucleon containing the struck quark. As the struck quark recoils the nucleon fragments, and the strong force between the quarks results in "hadronisation". In an experiment this appears as a jet of strongly interacting particles.

DIS is the dominant process for $E_\nu > 10\,\text{GeV}$ and continues to rise linearly until E_ν approaches M_Z and M_W (Figure 3.10).

3.6. Neutrino-Nucleus Interactions

The above set of interactions provides a fairly complete overview of the interactions which are available to neutrinos however, as is often the case, the situation in real experiments is more complicated. The best understood interactions are those with free electrons, but constructing a target of pure electrons is impossible in practice and the cross-section is much smaller than for nucleons. Ideally then experiments would like to study neutrino interactions directly on nucleons, but a target of pure neutrons is similarly impractical to construct. The simplest target that could be made is one of hydrogen but the critical CC QE interactions would only be available to anti-neutrinos - which have lower overall cross-sections and cannot be produced in the same quantities. Deuterium is a good target which was used in early experiments - the presence of both a neutron and a proton makes all neutrino-nucleon interactions available. However it is still relatively light, resulting in low interaction rates, and chemically very volatile. Driven by the need for higher interaction rates in large active detectors, particularly at far-detectors, experiments build their detectors out of heavier nuclei such as carbon, oxygen (water) or iron. But the fact that the target nucleons are then contained within a nucleus introduces effects which significantly complicates the resulting interactions observed in the detector.

The first effect to consider is the initial state of the nucleons. Nucleons in a nucleus are constantly moving around inside the nuclear potential, changing their momentum and direction. And the direction and momentum of the nucleon in relation to an incoming neutrino affects both the kinematics of any interaction, and the cross-section for an interaction even occurring. At high neutrino energies where Q^2 is large, these effects are negligible, but at lower Q^2 this is no longer true. Unfortunately the initial momentum spectra of nucleons is not well known, and can vary significantly between even similar mass nuclei. Most past experiments have used a simple relativistic Fermi-gas model [23] [24], but with the current generation of experiments investigating lower E_ν alternative models are being investigated, such as "spectral functions" [25] (see Figure 3.11).

Through an effect known as "Pauli-blocking", this nuclear potential also limits the final-state kinematics available to interactions which produce a nucleon. As a fermion, the resulting nucleon is not permitted to be in a state which is already occupied by another nucleon - reducing the available phase space

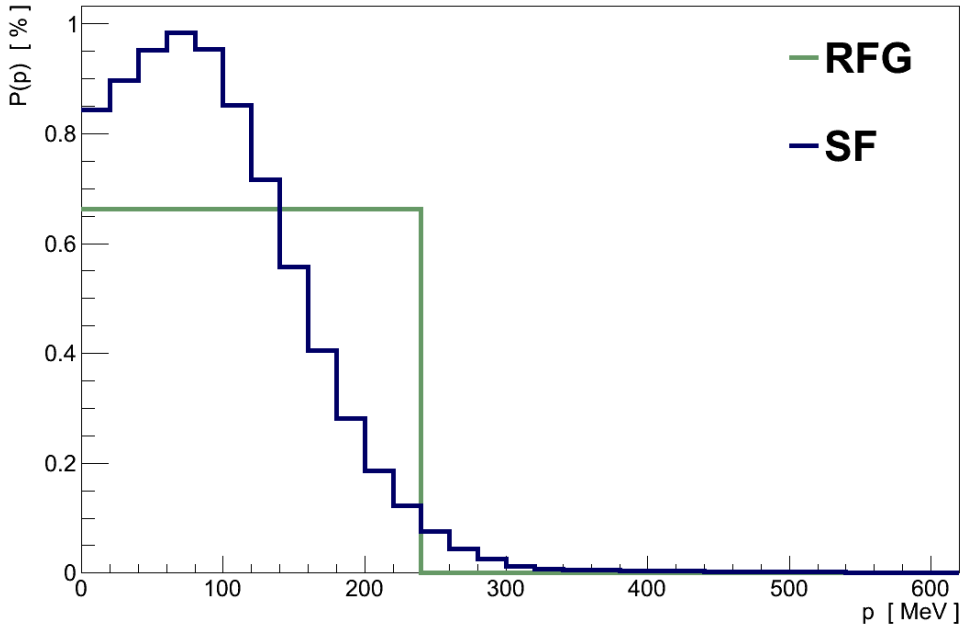

Figure 3.11: The nucleon momentum distributions from a relativistic Fermi-gas (with $p_F = 220\,\text{MeV}$) and a spectral function (both for ^{12}C).

and hence the cross-section. In the case of a relativistic Fermi-gas model this requires the final-state nucleon's momentum to exceed the Fermi-momentum.

Even the target with which the neutrino can interact is no longer limited to simply be individual nucleons, but can include correlated nucleon pairs, alpha particles, or any combination of nucleons in a quasi-bound state.

After the final-state particles have been created from an interaction, they then need to propagate out through the nucleus, at which point they can undergo strong interactions with the other nucleons inside the nucleus. These "final-state interactions" (FSI) can significantly alter the momentum and direction of the final-state particles. They can also alter the type and number of particles: pions and nucleons can be absorbed and never escape the nucleus, or their collisions with other nucleons can generate additional particles. Generally the final-state lepton is unaffected by FSI, though for electrons some radiative effects need to be considered [19], and higher momentum hadrons will be less affected. Still, the net effect is that the particles leaving the nucleus can be significantly different to those created at the interaction vertex.

All of these effects are present in all neutrino-nucleus interactions, but can largely be ignored at high E_ν where DIS dominates and the final-state particles

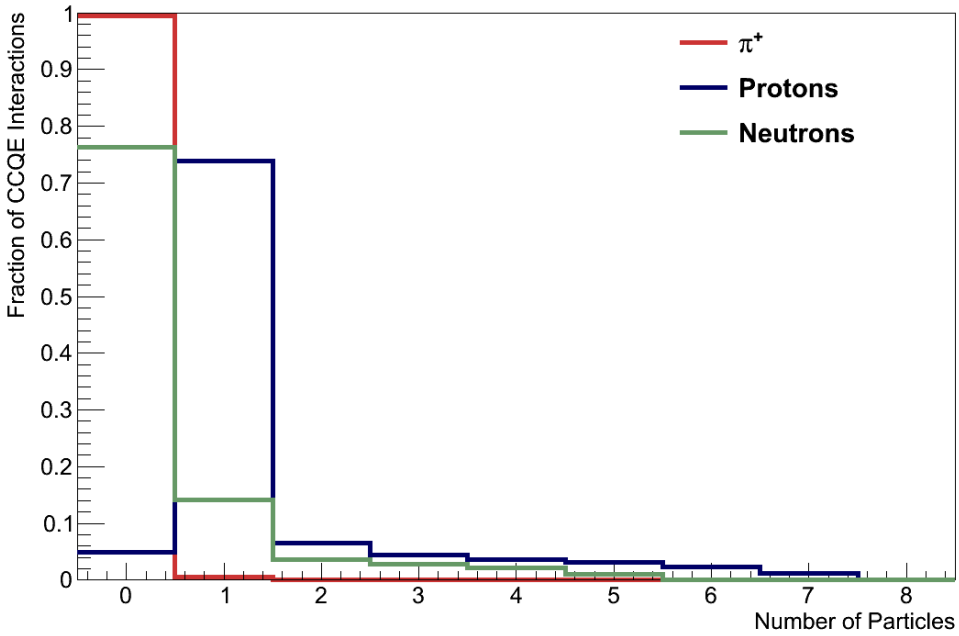

Figure 3.12: The number of hadronic particles leaving a ^{12}C nucleus after a ν_μ CC QE interaction at $E_\nu = 1.0\,GeV$, as simulated by GENIE. In addition, 2.4 % of interactions contained a π^0, and 0.7 % a π^-. In 16.2 % of events there were no particles at all.

are produced with high momenta. But they are much more important at lower E_ν, where scattering no longer occurs within nucleons but on them, where the target's momentum is of similar magnitude to the neutrino's, and interactions in the nucleus have relatively large effects on the type, number and kinematics of final-state particles.

It is important therefore that neutrino interaction experiments are aware of the consequences of these effects for their analysis, a couple of which are worth highlighting. First, any attempt to measure the neutrino-nucleon form-factors must have a complete understanding of the nuclear effects, or those effects will obscure the form-factors and lead, for example, to only an effective value of M_A (Equation 3.27) being measured.

Second, the particles and kinematics observed in neutrino detectors can not be equated to those generated at the interaction vertex. This means, for example, that a CC QE interaction may not appear as $\mu^- + p$ in the detector, and observing $\mu^- + p$ does not imply a CC QE interaction (see Figure 3.12). This is important when comparing theoretical predictions for interaction modes with experimental measurements: theories predict particles before final-state interactions, experiments measure them after final-state interactions. For

experiments in particular the lesson is to report measurements for particle topologies as seen in the detector, and not neutrino interaction modes.

3.6.1. Coherent Scattering

One advantage of using nuclear targets is that it makes available an additional interaction mode known as "coherent" scattering. The defining feature of coherent scattering is that the nucleus recoils as a whole, un-fragmented, in the same state as when the neutrino arrived. This can only be achieved if the four-momentum transfer to the nucleus is kept small.

One of the interesting features of coherent scattering is its nuclear A dependence: because the neutrino-nucleon amplitudes sum coherently the cross-section is proportional to A^2 ($\sigma_{\nu A} \sim |A \times \mathscr{M}_{\nu N}|^2$), instead of the A dependence resulting from a sum of independent cross-sections as in other neutrino-nucleon interactions ($\sigma_{\nu A} \sim A \times |\mathscr{M}_{\nu N}|^2$)[5].

At low E_ν, a neutrino can undergo NC coherent scattering, resulting only in the slight recoil of the struck nucleus. At higher neutrino energies, both CC and NC coherent scattering becomes possible, which also results in the creation of an additional final-state particle such as a π, ρ or K meson. Figure 3.13 shows the example of CC coherent π^+ production.

The requirement that the four-momentum transfer to the nucleus be kept small, strongly constrains the kinematics of coherent scattering such that the final-state lepton, and any additional particles created, are produced at small-scattering angles with respect to the incoming neutrino. It is also this constrained kinematics which results in the coherent cross-sections being relatively small.

Although the cross-sections for all coherent interactions are low, coherent pion production is an important interaction for oscillation experiments searching for ν_e, since the two decay photons from NC coherent π^0 production can mimic the electrons they are looking for (as with resonance π^0 production in

5. In practice, other nuclear effects mean that the dependence on A is more complicated (see Chapter 4), but this is true for the neutrino interaction vertex.

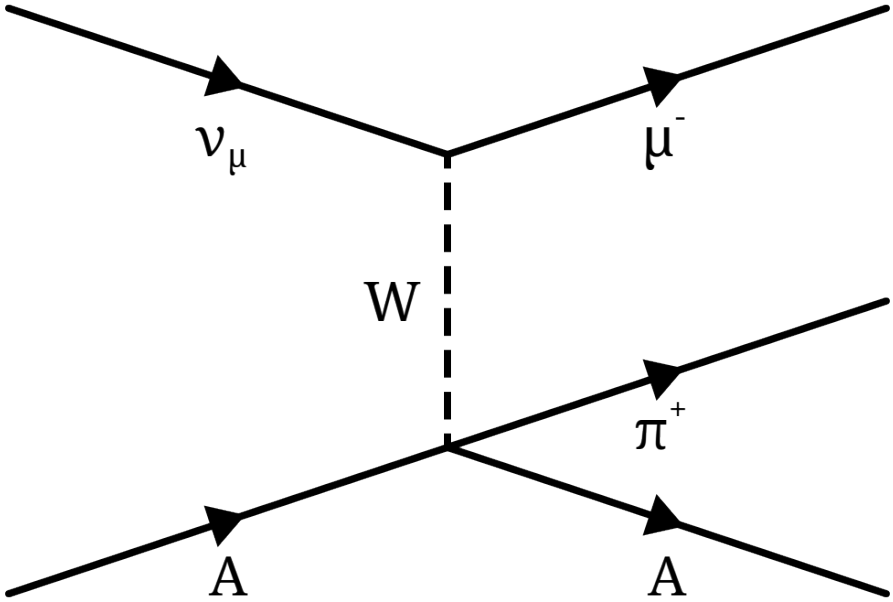

Figure 3.13: Diagram of CC coherent π^+ production.

Section 3.5.2). Neutrino induced coherent pion production will be discussed in much greater depth in Chapter 4.

3.7. Current Experimental Status

Although the various processes available to neutrinos interacting with nuclei are broadly known, the precision of that understanding and our ability to make predictions is limited by the current state of experimental data, which is often sparse, scattered or both.

Such data is required to constrain inputs to theoretical models, such as the form-factors discussed in Section 3.5.1. It is also required to better understand the processes involved in the "shallow inelastic" transition region between resonance and DIS dominance. And it is necessary to resolve the convoluted effects from the initial nuclear state, hadronisation and final-state interactions.

The least ambiguous measurement which can be made is the total CC cross-section for ν_μ or $\bar{\nu}_\mu$, since its definitions from theory and experiment are both equivalent and clear. However even here the existing experimental data

provides only weak constraints on predictions. The data for the total ν_μ CC cross-section was shown previously in Figure 3.4, however it spans a wide range in both cross-section and energy. Placing the energy on a log-scale and dividing the cross-section by energy, as in Figure 3.14, shows more clearly the freedom afforded both in absolute normalisation and in shape, particularly when $E_\nu < 10\,\text{GeV}$. This situation is worse for $\bar{\nu}_\mu$, also shown in Figure 3.14, where the data is more sparse in general and particularly so at low energies.

While the total interaction cross-section is unambiguous, it is less useful in constraining theoretical predictions and parameters because, particularly at low energy, it represents the combination of multiple interaction channels. To constrain predictions more effectively, more specific cross-sections are required.

The first plot in Figure 3.15 shows cross-sections measured for ν_μ CC QE in experiments either at high energies, or at low energies on light targets such as deuterium. The situation is similar to that for the total cross-section: at high energies the data is scattered and with large uncertainties, at low energies it is very sparse. However this data does still provide some constraint, one well known example being the fitting of $M_A = 1.014 \pm 0.014\,\text{GeV}$ [20] for the axial form-factor (Equation 3.27).

The second plot in Figure 3.15 shows more recent data on ν_μ CC QE on ^{12}C from the NOMAD experiment, and the lower energy MiniBooNE experiment. The data is clearly incompatible with the CC QE cross-section. Early attempts to explain the MiniBooNE discrepancy included fitting a higher value of $M_A = 1.35 \pm 0.17\,\text{GeV}$ [26]. However, while improving the theoretical agreement with the MiniBooNE data, such a high value of M_A was clearly in conflict with all other experimental data.

Since then two significant observations have been made regarding the MiniBooNE data. First, the analysis was conducted on a sample of interactions producing a muon and no charged pion, in contrast with the muon plus proton topology for NOMAD and most other data. Second, MiniBooNE were the first to attempt a measurement of the CC QE cross-section both at low-E_ν and on a heavy target. Given the discussion in Section 3.6, both of these observations highlight differences which are greatly influenced by nuclear effects which are larger at lower E_ν, and can substantially affect the particles produced by both CC QE interactions and its backgrounds. Attempts to include additional

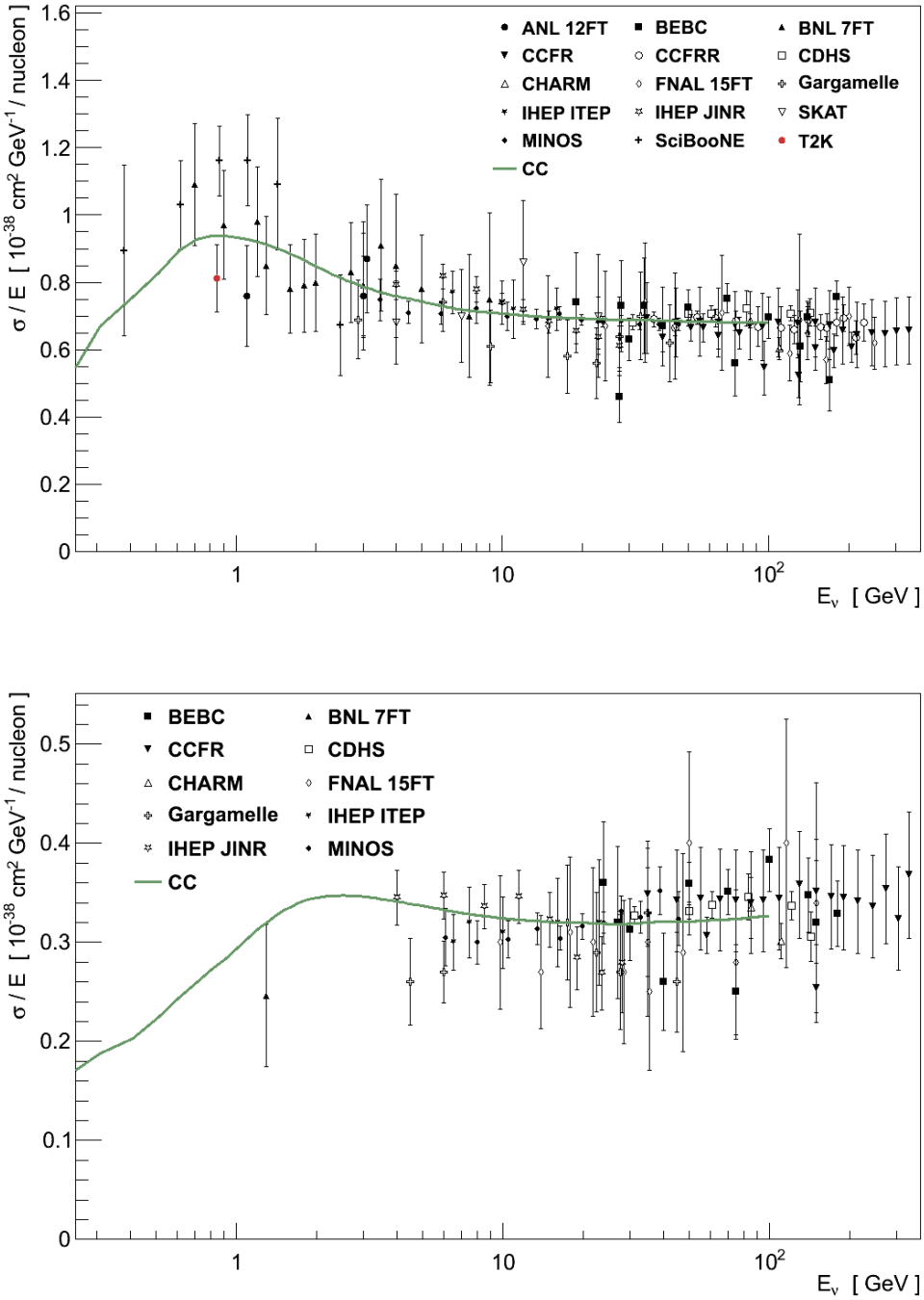

Figure 3.14: Data on total ν_μ (top) and $\bar{\nu}_\mu$ (bottom) CC cross-sections divided by energy, compared with the GENIE prediction. It is clear that the data affords a lot of freedom.

nuclear effects have had some success in explaining the MiniBooNE data while keeping $M_A \approx 1\,\text{GeV}$ [27].

Data on other neutrino interaction cross-sections starts to become sparse. Figure 3.16 shows data on ν_μ CC cross-sections for the production of various

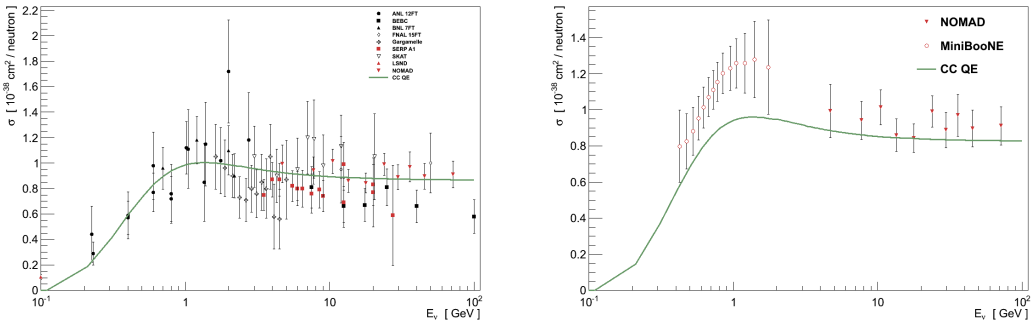

Figure 3.15: Data on the ν_μ CC QE cross-section, compared with the GENIE prediction for deuterium. (left) Data either at high energy or on deuterium matches well the model in GENIE. (right) The ν_μ CC QE cross-section cannot be simultaneously compatible with both the low-E_ν MiniBooNE data and NOMAD data (all on ^{12}C).

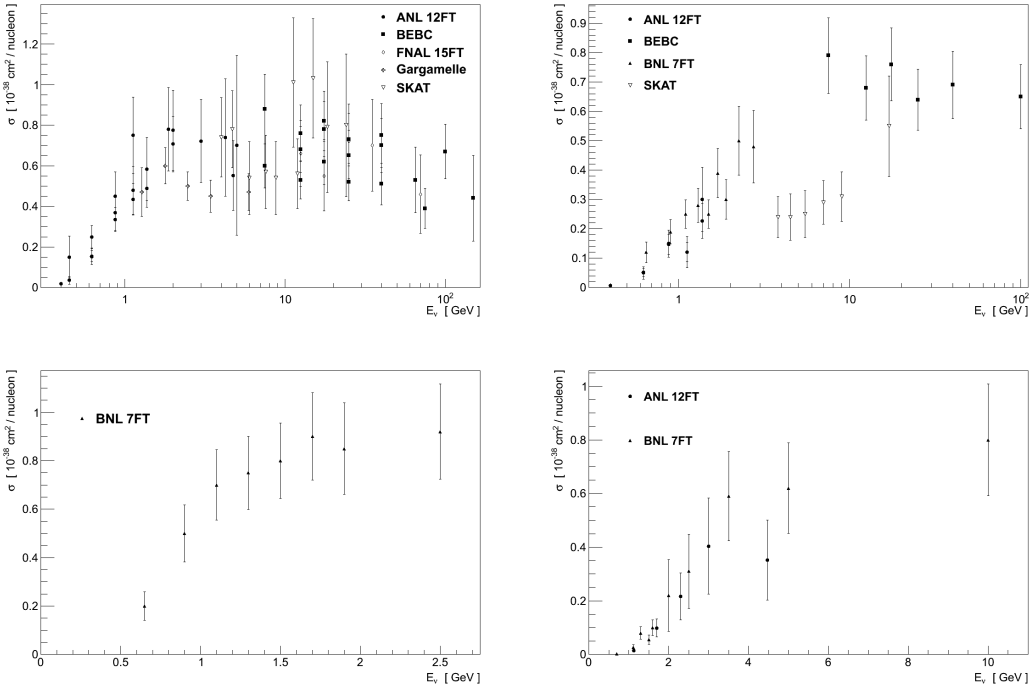

Figure 3.16: Data on cross-sections for ν_μ CC interactions with various pion-producing final-states: (top left) μ^- p π^+, (top right) μ^- p π^0, (bottom left) μ^- p π^-, (bottom right) μ^- p π^+ π^+. All data are on hydrogen/deuterium, with the exceptions of the Gargamelle and SKAT Freon detectors.

topologies which include pions. No cross-section calculations are shown in these plots, since they clearly relate to particle topologies and not a single interaction channel. It is data such as this which must be used to validate and constrain theoretical models of inelastic scattering, and the importance of nuclear effects is highlighted again in the top two plots of Figure 3.16 where the data on heavy targets (Gargamelle and SKAT) is clearly separate from the data on hydrogen and deuterium.

Data on NC processes is even rarer than for CC ones, with many processes having just one measurement available, if any at all. There is however a reasonable amount of experimental data on coherent pion production, though this is left until Chapter 4 where it is discussed in detail.

The plots in this section show data from the processes for which the most data is available. Given the degree of scatter and uncertainty in even the best of these, it is clear that a great deal of uncertainty will also exist in the theoretical models and parameters which they constrain. These models are in turn used in the simulations with which experiments define their analyses and interpret their data. It is for this reason that neutrino interactions contribute some of the largest uncertainties to neutrino oscillation measurements, and why improved understanding is essential to the field's progress.

3.8. Neutrino Interaction Simulations

As has just been discussed, neutrino interaction simulations play an important role in the development of experimental analyses, and the interpretation of the resulting measurements.

During the previous generation of experiments studying neutrino interactions, most experiments developed their own interaction simulation in-house. The Soudan 2 experiment developed NEUGEN [28] which was later adopted by MINOS, MiniBooNE and SciBooNE used NUANCE [29], and Super-Kamiokande and K2K used NEUT [30]. In general these interaction simulations were developed with a focus on their own experiment/targets/E_ν, and could often be heavily tuned to reproduce their own experiment's data.

More recently the GENIE [31] simulation has been developed to provide a more general framework which is valid over a wide range of experiments, targets and neutrino energies. Unlike earlier simulations, GENIE's more modular design allows it to accommodate multiple alternative models. It can also simulate interactions from probes other than neutrinos, which is useful in developing and validating models of form-factors and nuclear effects, which are better constrained by data from other scattering fields. GENIE is also openly available to the entire neutrino interaction community to view, run and contribute to.

It is often true that strength comes in diversity and so it would be natural to assume that the existence of multiple simulations is of benefit to the field. However in the current state of neutrino interactions the opposite is true. Because there are multiple components to simulating neutrino-nucleus interactions (nuclear model, interaction model, hadronisation model, final-state interactions) it is nearly impossible to assess the differences between two choices of model in one of these components unless the others are unchanged. Therefore comparisons between models are best made in the same simulation where all differences in the outputs can be attributed to the differences between the models in question. Furthermore, despite experimentalists' best efforts, empirical results often contain some direct or indirect dependence on the simulation used in the analysis. Comparisons between experimental measurements then are also made more difficult by the existence of multiple simulations.

As a result of the need for a unifying simulation, and its technical and structural advantages, it is expected that the neutrino interactions community will converge on the use of GENIE for future experiments. This will provide a single framework in which to develop and compare multiple models, which the entire community can benefit from. It is for these reasons that the work presented herein, on coherent modelling (Chapter 4) and cross-section analysis (Chapter 6), has been conducted with GENIE.

Finally, it should be mentioned that there are also a class of more theoretically driven simulations developed to study solutions to specific problems. NuWro [32] has been used to investigate the effects of alternative nuclear models. GIBUU [33] is essentially a model for transporting particles through a nucleus and studying final-state interactions. GIBUU is tuned heavily on data from a large variety of scattering sources, but is computationally too intensive to currently be utilised in an experiment's interaction simulations. The lessons learned from these more theoretical simulations can inform the development of simpler and less intensive models for use in full experimental simulations such as GENIE.

4. Coherent Pion Production

A coherent neutrino-nucleus interaction, as introduced in Section 3.6.1, is defined as one which leaves the nucleus in the same quantum state as it was initially. The nucleus' constituents must retain their identity, and the nucleus cannot be excited or fragmented, though it can recoil.

A specific case of this type of interaction is that of coherent pion production, which can procede either via the charged- or neutral-current, and in which the neutrino scatters off the nucleus, A, and produces a single pion of appropriate charge:

- ν_l A $\rightarrow$ l^- π^+ A
- $\bar{\nu}_l$ A $\rightarrow$ l^+ π^- A
- ν_l A $\rightarrow$ ν_l π^0 A

Coherent pion production has become an important interaction to neutrino physics for two reasons. First, the neutral-current channel results in the production of a single π^0 with no other observable particles. Since π^0's exclusively decay to two photons, any decay where the photons are collinear or one of the photons has most of the energy in the laboratory-frame, runs the risk of being mis-identified as an electron. This makes coherent π^0 production a dangerous background for oscillation experiments searching for ν_e. Second, coherent pion production is an important part of the broader goal of understanding neutrino-induced pion production in general. Due to the nuclear effects discussed in Section 3.6, it is quite possible for CC QE interactions to produce an outgoing pion, and similarly possible for a pion-producing interaction to have the pion absorbed. Correctly understanding coherent pion production therefore is a necessary part of any effort to improve understanding of these other reactions.

The requirement that the nucleus remain intact and unaffected by this interaction gives rise to several characteristic features of coherent pion production. The first is that the four-momentum transferred to the nucleus must remain small, since any substantial transfer absorbed by the nucleus would excite or otherwise fragment it and break coherence. This is

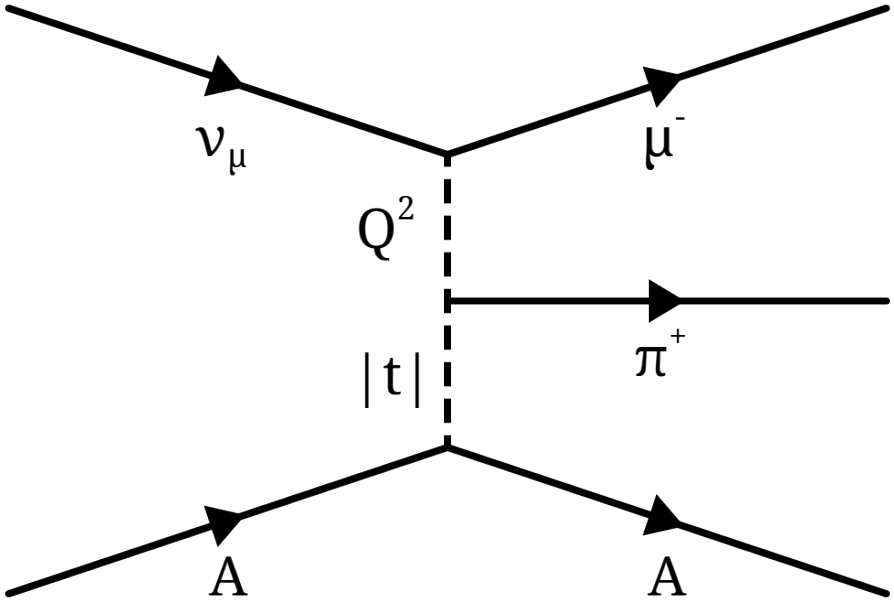

Figure 4.1: The conventional view used to describe coherent pion production, shown for the ν_μ CC case. The squared four-momentum transfer to the nucleus is denoted |t|.

characterised by the kinematic variable, |t|, which is the squared four-momentum transfer to the nucleus, from the neutrino-lepton-pion system:

$$| t | = \left| \left(q - P_\pi\right)^2 \right| = \left| \left(P_\nu - P_l - P_\pi\right)^2 \right| \tag{4.1}$$

Figure 4.1 shows |t| in relation to the other momentum transfers in the conventional view of CC coherent pion production. Of all the kinematic variables, |t| is the most characteristic indicator of coherence. The usual measure of momentum transfer, Q^2, is at times used in its stead but since larger transfers to the pion do not in principle break coherence it is not as direct an indicator.

As a result of requiring small momentum transfers, coherent pion interactions also tend to produce events with a very forward-going lepton and pion with respect to the incoming neutrino's direction. In the case of NC coherent this is particularly useful, since the inability to observe the final-state lepton prevents the calculation of |t|. Finally, because the nucleus remains intact and recoils only slightly, coherent pion production is often distinguished by searching for

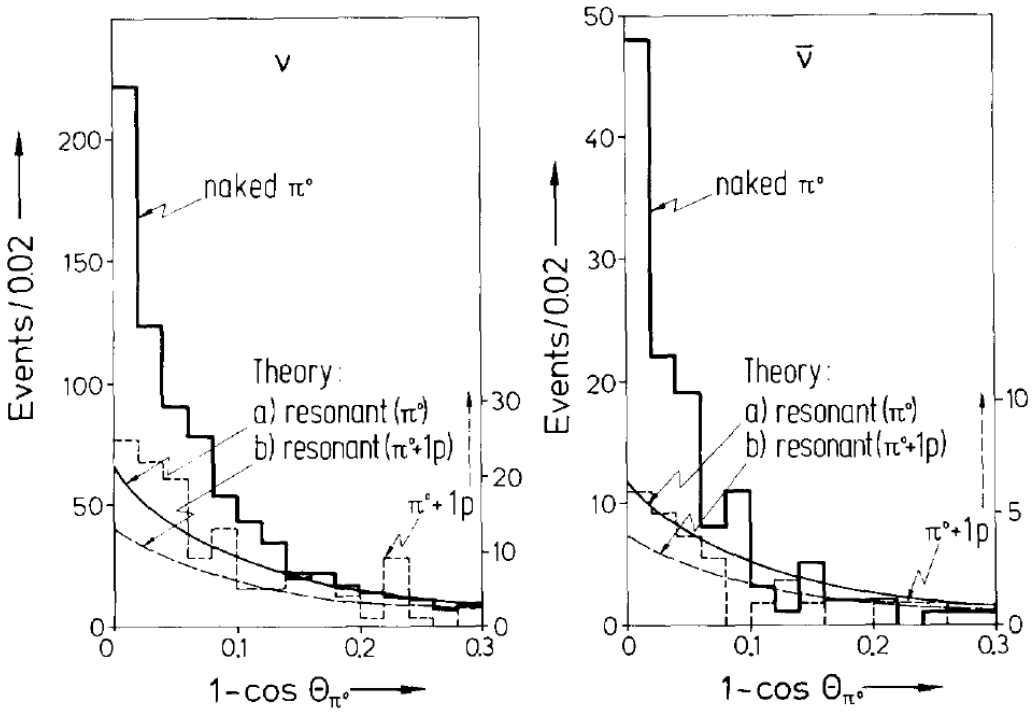

Figure 4.2: The data (histogram) and theoretical prediction (curve) for the angular distribution of π^0s produced in Aachen-Padova's ν_μ (left) and $\bar{\nu}_\mu$ (right) beams. The solid lines represent a sample of isolated ("naked") π^0s, and the dashed lines a sample where the π^0 is accompanied by a recoil proton. There is a clear excess in the "naked" sample in the forward-going region [34].

additional short tracks or large energy deposits at the interaction vertex, the presence of either hinting at a non-coherent interaction.

4.1. Experimental History

The first observation of coherent pion production was reported in February 1983 by the Aachen-Padova spark-chamber experiment [34] in CERN's PS neutrino/anti-neutrino beam. While studying a sample of solitary π^0s produced in their ν_μ and $\bar{\nu}_\mu$ beams they observed a significant excess of events in the forward-going direction, an excess that was not present in another sample in which the π^0 was produced along with a proton (Figure 4.2). They identified this excess as NC coherent pion production: a theoretical description of which had first been published by K.S. Lackner [35] four years earlier in the context of determining the structure of the weak neutral-current.

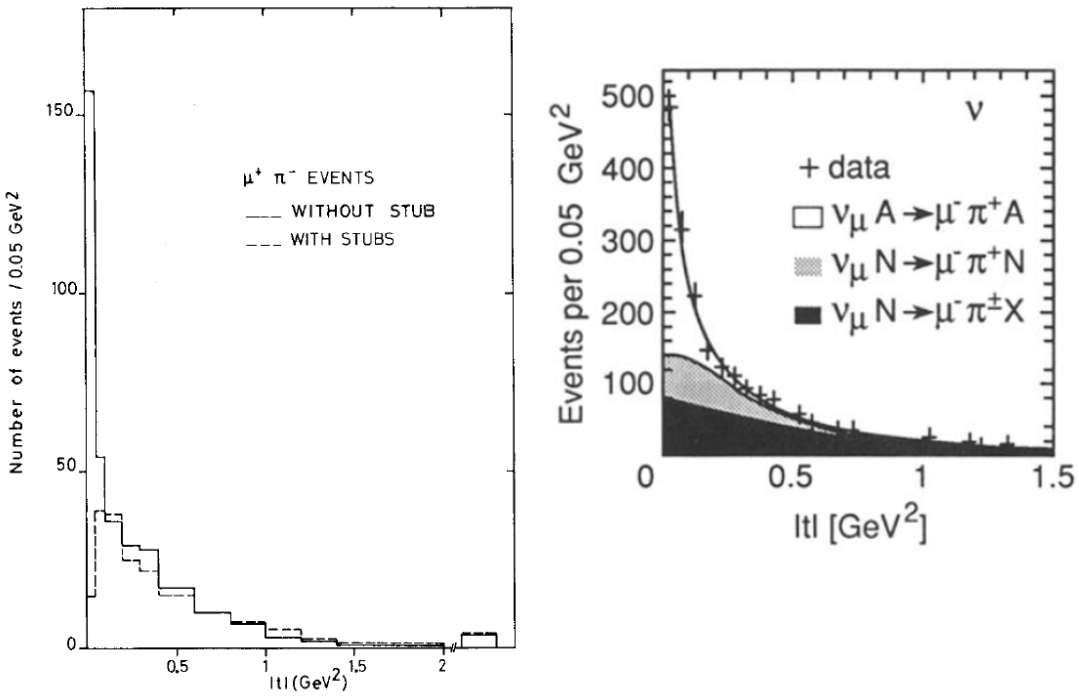

Figure 4.3: Clear CC coherent signals in |t| measurements. (Left) The the BEBC [38] experiment's bubble chamber detector had excellent resolution on additional short tracks, "stubs", at the vertex. (Right) The CHARM II [39] experiment took high statistics data with a clear and well described coherent (white) component.

In response to Aachen-Padova's discovery, Dieter Rein and Lalit Sehgal developed a theoretical model for coherent pion production [36], building on Lackner's paper and their own recent work on resonance pion production. Their predictions agreed with the cross-section extracted by Aachen-Padova, as well as one from a retrospective re-analysis of data from the Gargamelle experiment [37].

Over the following decade five more experiments observed and measured both CC and NC coherent pion production with neutrinos and anti-neutrinos. Many giving exceptionally clean and clear signals of coherent production such as those in Figure 4.3. Over a wide range of neutrino energies all experimental data were consistent with predictions from the Rein-Sehgal model, within the resolution of the measurements (Figure 4.4).

The resurgence of neutrino physics that accompanied the discovery of oscillations at the beginning of the 21st century also brought about a series of experiments at lower neutrino energies than had been studied previously. In stark contrast to previous experiments, K2K's search for CC coherent pion production at E_ν of 1.3 GeV found no evidence for its existence. This surprising result was later confirmed by SciBooNE, which also set cross-section

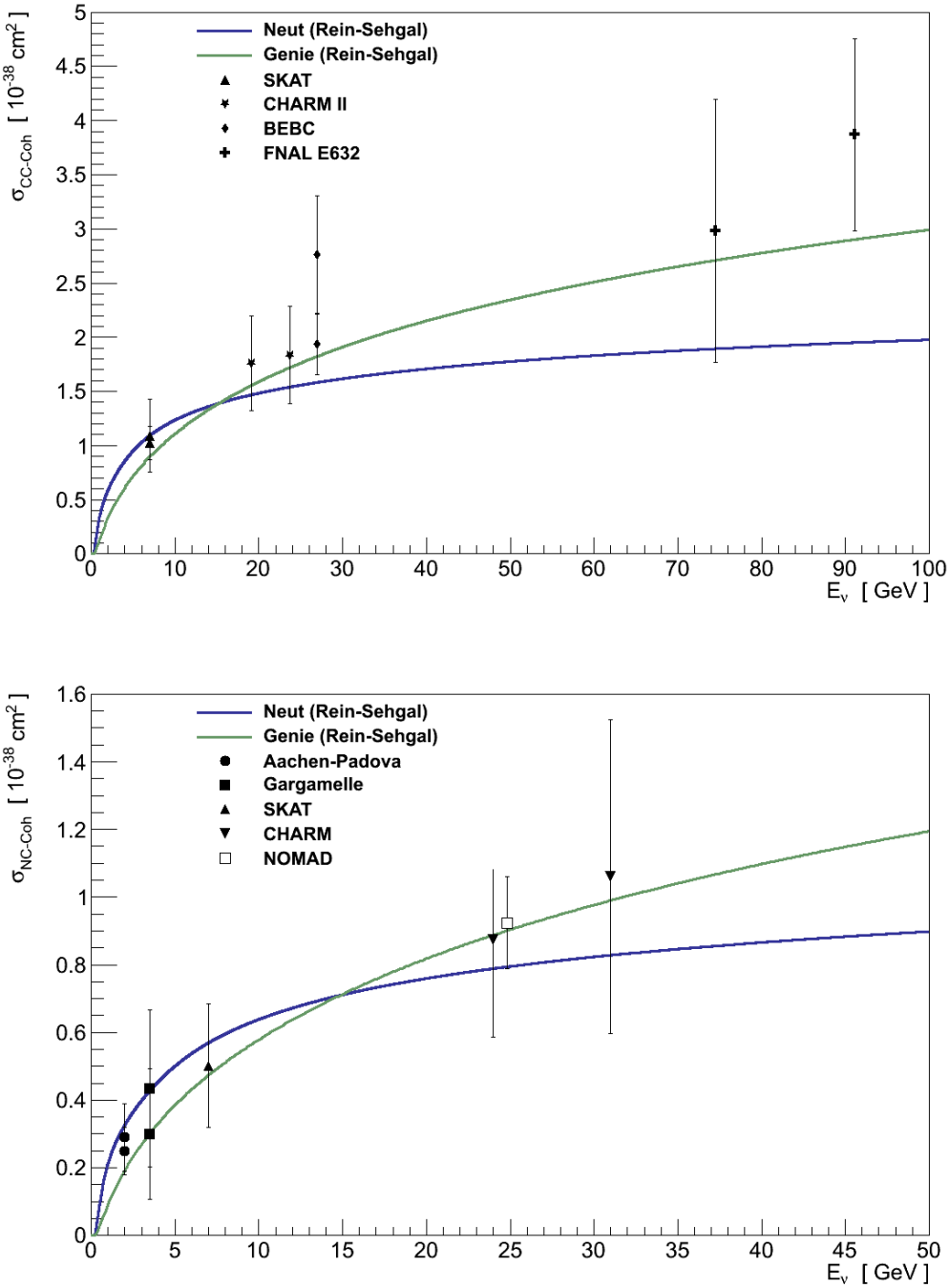

Figure 4.4: The cross-section for CC (top) and NC (bottom) coherent pion production on ^{27}Al. The data are all experimental measurements from ν_μ and $\bar{\nu}_\mu$ with $E_\nu \geq 2$ GeV. They are compared with the Rein-Sehgal predictions from GENIE and NEUT. The data and NEUT are scaled to ^{27}Al according to the approximate $A^{1/3}$ dependancy noted by Rein-Sehgal.

limits well below the level predicted by the Rein-Sehgal model implemented in NEUT (the interaction simulation both experiments were using), shown in Figure 4.5. Measurements of NC coherent pion production were successfully made in both MiniBooNE and SciBooNE, but even here the cross-sections

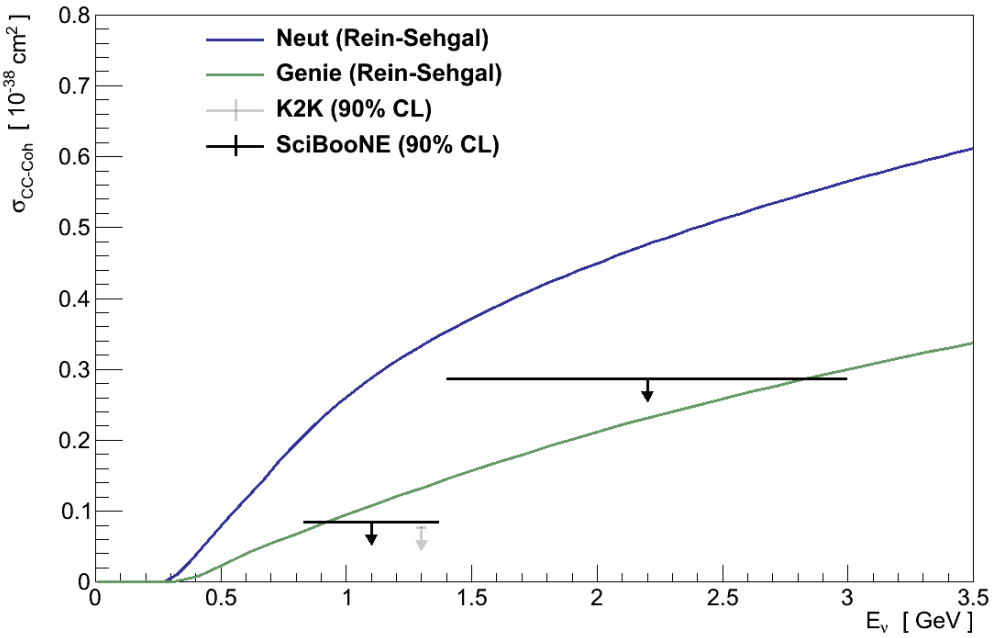

Figure 4.5: The 90% CL limits set for CC coherent pion production on ^{12}C by the K2K and SciBooNE experiments. Compared with Rein-Sehgal from NEUT and GENIE. The width of the SciBooNE limits is the RMS of the interacting neutrinos in the respective sample. The energy range of the K2K result is unpublished.

reported were a substantial reduction on the values expected from the Rein-Sehgal implementations in NEUT and NUANCE.

Table 4.1 lists all experimental data on neutrino induced coherent pion production. With measurements in multiple beamlines, on multiple targets, and across a range of neutrino energies, the experimental evidence for the existence of coherent pion production is clear and undeniable. But below neutrino energies of ~2 GeV the previously successful Rein-Sehgal model over-predicts the NC cross-section, and there is no experimental evidence for CC coherent production at all.

4.2. Rein-Sehgal Model

As mentioned above, the majority of data on coherent pion production, taken at high neutrino-energies, is satisfactorily described by the model published by Deiter Rein and Lalit Sehgal [36] and updated to account for a non-zero final-state lepton mass [49].

Experiment	Target (A^{eff})	E_ν [GeV]	Reac.	Cross-Section [10^{-40}cm^2/nucleus]	Ref
Aachen-Padova	Aluminium (27)	2	NC ν_μ	29 ± 10	[34]
Aachen-Padova	Aluminium (27)	2	NC $\bar{\nu}_\mu$	25 ± 7	[34]
Gargamelle	Freon (30)	3.5	NC ν_μ	31 ± 20	[37]
Gargamelle	Freon (30)	3.5	NC $\bar{\nu}_\mu$	45 ± 24	[37]
CHARM	Marble (20)	31	NC ν_μ	96 ± 42	[40]
CHARM	Marble (20)	24	NC $\bar{\nu}_\mu$	79 ± 26	[40]
SKAT	Freon (30)	7	NC ν_μ	52 ± 19	[41]
SKAT	Freon (30)	7	CC ν_μ	106 ± 16	[41]
SKAT	Freon (30)	7	CC $\bar{\nu}_\mu$	113 ± 35	[41]
BEBC	Neon (20)	27	CC $\bar{\nu}_\mu$	175 ± 25	[38]
BEBC	Neon (20)	27	CC ν_μ	250 ± 49	[42]
FNAL E632	Neon (20)	91.1	CC ν_μ	350 ± 80	[43]
FNAL E632	Neon (20)	74.5	CC $\bar{\nu}_\mu$	270 ± 110	[43]
CHARM II	Glass (20.7)	23.7	CC ν_μ	168 ± 41	[39]
CHARM II	Glass (20.7)	19.1	CC $\bar{\nu}_\mu$	161 ± 40	[39]
K2K	Carbon (12)	1.3	CC ν_μ	$<$ 0.077 (90% CL)	[44]
MiniBooNE	CH_2 (12)	0.7	NC ν_μ	$(0.195 \pm 0.075) \times \sigma_{NC\pi^0}$	[45]
SciBooNE	Carbon (12)	1.1	CC ν_μ	$<$ 0.0844 (90% CL)	[46]
SciBooNE	Carbon (12)	2.2	CC ν_μ	$<$ 0.287 (90% CL)	[46]
NOMAD	Carbon (12.8)	25	NC ν_μ	72.6 ± 10.6	[47]
SciBooNE	Carbon (12)	0.8	NC ν_μ	$(0.012 \pm 0.002) \times \sigma_{CC}$	[48]

Table 4.1: A summary of all experimental data on neutrino induced coherent pion production. The E_ν stated is the flux average, with the exception of MiniBooNE for which it is the flux peak, and Gargamelle which is an estimate. The values of A^{eff} are the best estimates available and are the ones used to scale the data in Figure 4.4.

The Rein-Sehgal model begins from Adler's partially conserved axial-vector current (PCAC) theorem [50], which allows the cross-section for neutrino-nucleus scattering to be described in terms of the analogous pion-nucleus interaction. This is then adapted to the specific case of coherent pion production, and modified to account for the reduction of that cross-section

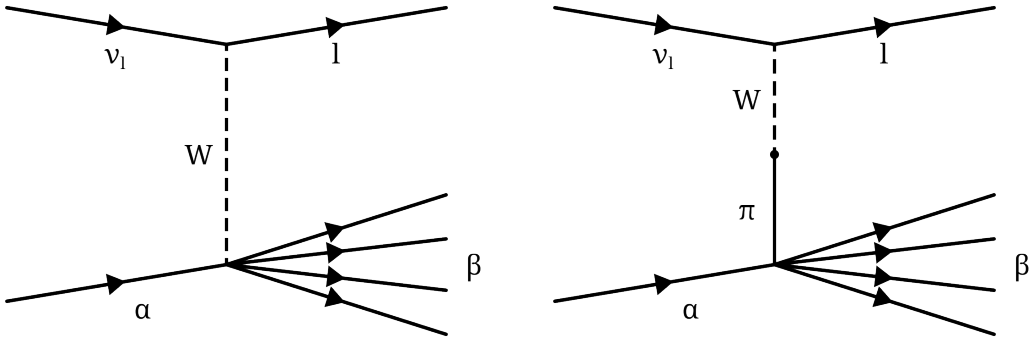

Figure 4.6: Adler's PCAC theorem relates the amplitude for $\nu_l\ \alpha \rightarrow l\ \beta$ (left) to the analogous process for pion scattering $\pi\ \alpha \rightarrow \beta$ (right).

due to the potential for intra-nuclear pion absorption (which would break coherence). In the final part of Rein-Sehgal, choices for the various inputs to the model are made, some of which can have noticeable effects on both the total and differential cross-sections predicted.

All the cross-section plots shown in this section were calculated using GENIE version 2.6.6, which was modified to fix a bug in the calculation of the pion-nucleon cross-sections which are an input to the Rein-Sehgal model.

4.2.1. Adler's PCAC Theorem

The general approach of Adler's PCAC theorem [50] can be broken into two steps. First, it is found that in the limit of small-angle scattering, where the final-state lepton is parallel to the incoming neutrino, the cross-section for neutrino-nucleus scattering depends only on the divergence of the axial-vector part of the weak current. Second, as a consequence of PCAC, the divergence of the axial-vector current can be related to the pion.

Effectively then, when the final-state lepton's scattering angle is small, the cross-section for weak scattering from an initial hadronic system, α, to a final hadronic system, β can be related to the analogous process in pion scattering, as shown in Figure 4.6.

Following the treatment of Adler, this is shown by starting with the amplitude for the process $\nu_l\ \alpha \rightarrow l\ \beta$:

$$\mathscr{M} = \frac{G_F}{\sqrt{2}} \overline{u}_l \left(\gamma_\mu - \gamma_\mu \gamma_5\right) u_\nu \left\langle \beta \;\middle|\; V^\mu + A^\mu \;\middle|\; \alpha \right\rangle \tag{4.2}$$

Assuming the final-state lepton emerges parallel to the incoming neutrino and neglecting its mass, the amplitude, squared and averaged over the lepton's spin, is:

$$\left\langle \left| \mathscr{M} \right|^2 \right\rangle = 2 {G_F}^2 \frac{E_\nu E_l}{{q_0}^2} q^2 \left| \left\langle \beta \;\middle|\; V^\mu + A^\mu \;\middle|\; \alpha \right\rangle \right|^2 \tag{4.3}$$

$$\left\langle \left| \mathscr{M} \right|^2 \right\rangle = 2 {G_F}^2 \frac{E_\nu E_l}{{q_0}^2} q_\mu \left\langle \beta \;\middle|\; V^\mu + A^\mu \;\middle|\; \alpha \right\rangle q_\nu \left\langle \beta \;\middle|\; V^\nu + A^\nu \;\middle|\; \alpha \right\rangle^* \tag{4.4}$$

Since q is the four-momentum of the weak current:

$$\left\langle \beta \;\middle|\; \partial_\mu \left(V^\mu + A^\mu \right) \;\middle|\; \alpha \right\rangle = q_\mu \left\langle \beta \;\middle|\; V^\mu + A^\mu \;\middle|\; \alpha \right\rangle \tag{4.5}$$

Substituting Equation 4.5 into Equation 4.4:

$$\left\langle \left| \mathscr{M} \right|^2 \right\rangle = 2 {G_F}^2 \frac{E_\nu E_l}{{q_0}^2} \left\langle \beta \;\middle|\; \partial_\mu \left(V^\mu + A^\mu \right) \;\middle|\; \alpha \right\rangle \left\langle \beta \;\middle|\; \partial_\nu \left(V^\nu + A^\nu \right) \;\middle|\; \alpha \right\rangle^* \tag{4.6}$$

$$\left\langle \left| \mathscr{M} \right|^2 \right\rangle = 2 {G_F}^2 \frac{E_\nu E_l}{{q_0}^2} \left| \left\langle \beta \;\middle|\; \partial_\mu \left(V^\mu + A^\mu \right) \;\middle|\; \alpha \right\rangle \right|^2 \tag{4.7}$$

Requiring the final-state lepton to be parallel to the incoming neutrino is equivalent to requiring a small momentum transfer. Recalling from Section 3.5.1 that at $Q^2 \approx 0$ the vector current is conserved (CVC), implying $\partial_\mu V^\mu = 0$, leaves just the axial part of the current:

$$\left\langle \left| \mathscr{M} \right|^2 \right\rangle = 2 {G_F}^2 \frac{E_\nu E_l}{{q_0}^2} \left| \left\langle \beta \;\middle|\; \partial_\mu A^\mu \;\middle|\; \alpha \right\rangle \right|^2 \tag{4.8}$$

This concludes the first step: showing that when a final-state lepton is parallel to the incoming neutrino, the cross-section depends only on the divergence of the axial-vector current.

The divergence of the axial-vector current can be related to another weak process: pion decay. The decay of the pion, which is almost exclusively via $\pi^+ \rightarrow \mu^+ \nu_\mu$, is a purely weak process with low-Q^2 ($= m_\pi{}^2$). The matrix element for this process is:

$$\mathscr{M} = \frac{G_F}{\sqrt{2}} \Big\langle \mu \;\Big|\; \gamma_\mu - \gamma_\mu\gamma_5 \;\Big|\; \nu \Big\rangle \Big\langle 0 \;\Big|\; \gamma_\mu - \gamma_\mu\gamma_5 \;\Big|\; \pi \Big\rangle \tag{4.9}$$

The second term, in which the pion field is coupled to the vacuum via the weak current, must be treated with a form-factor since, like nucleons, pions are compound objects which cannot simply be described:

$$\Big\langle 0 \;\Big|\; V^\mu + A^\mu \;\Big|\; \pi \Big\rangle = f_\pi P_\pi{}^\mu \Phi \tag{4.10}$$

Here Φ is the pion field, P_π is the pion four-momentum, and the form-factor f_π is known as the pion decay constant. Taking the divergence:

$$\Big\langle 0 \;\Big|\; \partial_\mu \Big(V^\mu + A^\mu \Big) \;\Big|\; \pi \Big\rangle = f_\pi P_{\pi\mu} P_\pi{}^\mu \Phi \tag{4.11}$$

$$\Big\langle 0 \;\Big|\; \partial_\mu \Big(V^\mu + A^\mu \Big) \;\Big|\; \pi \Big\rangle = f_\pi P_\pi{}^2 \Phi \tag{4.12}$$

Again, because pion decay is a low-Q^2 process with CVC, $\partial_\mu V^\mu = 0$ leaving:

$$\Big\langle 0 \;\Big|\; \partial_\mu A^\mu \;\Big|\; \pi \Big\rangle = f_\pi m_\pi{}^2 \Phi \tag{4.13}$$

This relates the divergence of the axial-vector current with the pion field and is known as the "PCAC relation" since the fact that $m_\pi \neq 0$ implies that the axial-vector current is not completely conserved. It is through this that the Goldberger-Treiman relation allows the divergence of the axial-vector current in Equation 4.8 can be equated with the corresponding scattering with a pion [50]:

$$\Big| \Big\langle \beta \;\Big|\; \partial_\mu A^\mu \;\Big|\; \alpha \Big\rangle \Big|^2 = f_\pi{}^2 \Big| \mathscr{M}\big(\pi + \alpha \rightarrow \beta \big) \Big|^2 \tag{4.14}$$

Putting Equation 4.14 into Equation 4.8:

$$\left\langle \mid \mathscr{M} \mid^{2} \right\rangle = 2{G_F}^2 \frac{E_\nu E_l}{{q_0}^2} {f_\pi}^2 \mid \mathscr{M}\big(\pi + \alpha \to \beta\big) \mid^{2} \tag{4.15}$$

Finally, the corresponding differential cross-section, in terms of Bjorken-x and inelasticity is [51]:

$$\frac{\mathrm{d}^2\,\sigma}{\mathrm{d}\,x\,\mathrm{d}\,y} = \frac{{G_F}^2 m_N E_\nu}{\pi^2} {f_\pi}^2 (1-y)\sigma\big(\pi + \alpha \to \beta\big) \tag{4.16}$$

Which is Adler's PCAC theorem, relating the cross-section for neutrino forward-scattering, to the analogous cross-section for pion scattering.

4.2.2. Coherent Pion Production Cross-Section

Adler's PCAC formula is the starting point for the Rein-Sehgal model which was initially authored to describe NC coherent pion production: ν A $\to \nu\ \pi^0$ A. Taking Equation 4.16 with α = A and $\beta = \pi^0$ A, and including the pion scattering cross-section's dependence on |t|, gives a coherent cross-section:

$$\frac{\mathrm{d}\,\sigma}{\mathrm{dxdyd|t|}} \Bigg|_{Q^2\,=\,0} = \frac{{G_F}^2 m_N E_\nu}{\pi^2} {f_{\pi^0}}^2 (1-y) \frac{\mathrm{d}\,\sigma\Big(\pi^0 A \to \pi^0 A\Big)}{\mathrm{d|t|}} \tag{4.17}$$

Here, the neutral-pion decay constant $\mathrm{f_{\pi^0}}^2 = \frac{1}{2}\mathrm{f_\pi}^2$, $\mathrm{m_N}$ is the nucleon mass, and the constraint that $\mathrm{Q}^2 = 0$ comes from the fact that Adler's theorem only applies when the final-state neutrino is scattered exactly forward. They then extrapolated beyond $\mathrm{Q}^2 = 0$ by including a dipole form-factor:

$$\frac{\mathrm{d}\,\sigma}{\mathrm{dxdyd|t|}} = \frac{{G_F}^2 m_N {f_\pi}^2 E_\nu (1-y)}{2\pi^2} \left(\frac{{M_A}^2}{{M_A}^2 + Q^2}\right)^2 \frac{\mathrm{d}\,\sigma\Big(\pi^0 A \to \pi^0 A\Big)}{\mathrm{d|t|}} \tag{4.18}$$

The corresponding cross-section for CC coherent pion production differs by a factor of 2, resulting from the change of pion-decay constant. More recently, in

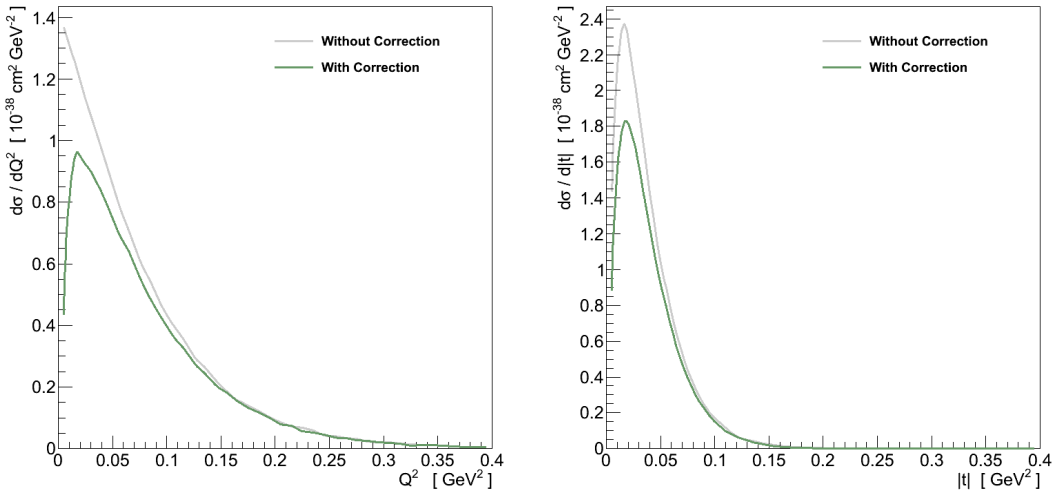

Figure 4.7: The effect of the lepton mass correction term in Equation 4.19 on CC coherent production on ^{12}C at $E_\nu = 1$ GeV. The Q^2 distribution (left) is heavily suppressed at low values, much more so than |t| (right).

response to the limit set by K2K, Rein and Sehgal published an update to this model [49] to account for the lepton mass in CC interactions. It is implemented as a multiplicative correction, C, to the cross-section in Equation 4.18:

$$C = \left(1 - \frac{\frac{1}{2}Q^2_{\text{min}}}{Q^2 + m^2_\pi}\right)^2 + \frac{1}{4}y\frac{Q^2_{\text{min}}\left(Q^2 - Q^2_{\text{min}}\right)}{\left(Q^2 + m^2_\pi\right)^2} \tag{4.19}$$

Where:

$$Q^2_{\text{min}} = m^2_l \frac{y}{1-y} \tag{4.20}$$

This results in a reduction of the CC coherent cross-section at low energies and, as can be seen in Figure 4.7, there is a dramatic suppression in the Q^2 distribution at low values. This is significant since both SciBooNE and K2K used the Q^2 distribution in their search for CC coherent rather than the more characteristic |t|, the shape of which is less affected.

4.2.3. Inputs to the Cross-Section

To use this cross-section to make calculations now requires choices to be made about inputs. The most significant of these is the choice of pion scattering cross-section, but there are also three free parameters in the model which can be tweaked.

Rein and Sehgal chose to express the pion-nucleus cross-section in terms of the pion-nucleon forward-scattering cross-section:

$$\frac{\mathrm{d}\,\sigma\left(\pi^0 A \rightarrow \pi^0 A\right)}{\mathrm{d}|\mathrm{t}|} = A^2 \mid F_A(\mathrm{t}) \mid^2 \left.\frac{\mathrm{d}\,\sigma\left(\pi^0 N \rightarrow \pi^0 N\right)}{\mathrm{d}|\mathrm{t}|}\right|_{t=0} \tag{4.21}$$

Where $\mathrm{F_A(t)}$ is a nuclear form-factor. The forward-scattering pion-nucleon cross-section was in turn related to the total cross-section for π^0-N scattering:

$$\left.\frac{\mathrm{d}\,\sigma\left(\pi^0 N \rightarrow \pi^0 N\right)}{\mathrm{d}|\mathrm{t}|}\right|_{t=0} = \frac{1}{16\pi}\left(\sigma_{\mathrm{tot}}^{\pi^0 N}\right)^2\left(1+r^2\right) \tag{4.22}$$

where r is the ratio of the real to imaginary parts of the π-N forward amplitude:

$$r = \frac{\Re\left[f_{\pi\mathrm{N}}[0]\right]}{\Im\left[f_{\pi\mathrm{N}}[0]\right]} \tag{4.23}$$

Finally, the nucleus form-factor was treated as a |t| dependent exponential, and an absorption factor:

$$\mid F_A(\mathrm{t}) \mid^2 = e^{-b|\mathrm{t}|} F_{\mathrm{abs}} = e^{-R_0 A^{1/3}|\mathrm{t}|} F_{\mathrm{abs}} \tag{4.24}$$

$$F_{\mathrm{abs}} = \exp\left(-\frac{9A^{1/3}}{16\pi {R_0}^2}\sigma_{\mathrm{inel}}^{\pi N}\right) \tag{4.25}$$

The absorption factor essentially comes from considering the mean path of a pion leaving the nucleus and the probability for it to interact and break coherence. The likelihood of such an interaction is taken from the cross-section for π-N inelastic scattering (the origin of which will also be discussed in a moment), and the nuclear radius scale, R_0, is used to estimate the nuclear radius $R = R_0 A^{1/3}$.

Putting these elements back into Equation 4.18 gives the Rein-Shegal differential cross-section as:

$$\frac{\mathrm{d}\,\sigma}{\mathrm{dxdyd|t|}} = \frac{{G_F}^2 m_N {f_\pi}^2 E_\nu (1-y)}{2\pi^2}\left(\frac{M_A^2}{M_A^2+Q^2}\right)^2 \frac{A^2}{16\pi}\left(\sigma_{\mathrm{tot}}^{\pi N}\right)^2\left(1+r^2\right)e^{-b|\mathrm{t}|}F_{\mathrm{abs}} \tag{4.26}$$

The most significant input to the Rein-Sehgal model is the choice of total and inelastic pion-nucleon cross-sections. In the original paper, the authors derived them from the corresponding pion-deuterium cross-sections:

$$\sigma^{\pi^0 N} = \frac{1}{4}\left(\sigma^{\pi^+ D} + \sigma^{\pi^- D}\right) \tag{4.27}$$

which were parametrised by making line-fits to data from CERN-HERA. The cross-sections implemented in GENIE followed a similar procedure but used more modern π-D data from the Particle Data Group (though the version is not stated). An alternative approach was taken in a standalone implementation of the Rein-Sehgal model for a paper by Berger and Sehgal [52], who took π-proton data from the Particle Data Group (2008) and fitted a superposition of Breit Wigner functions and a term motivated by Regge-theory.

In order to study the effect of these different pion-nucleon cross-sections, without other model differences obscuring, the original Rein-Sehgal and new Berger-Sehgal cross-sections were implemented in a copy of GENIE version 2.6.6. The original Rein-Sehgal cross-sections were implemented utilising the data for them hard-coded within NEUT [30]. The Berger-Sehgal cross-sections were implemented by interfacing with code provided (indirectly) by the authors. Figure 4.8 shows a comparison of these cross-sections. They agree well at high E_π but differ in the amplitude and position of peaks at lower energies. One noticeable difference in the original Rein-Sehgal cross-sections, which is

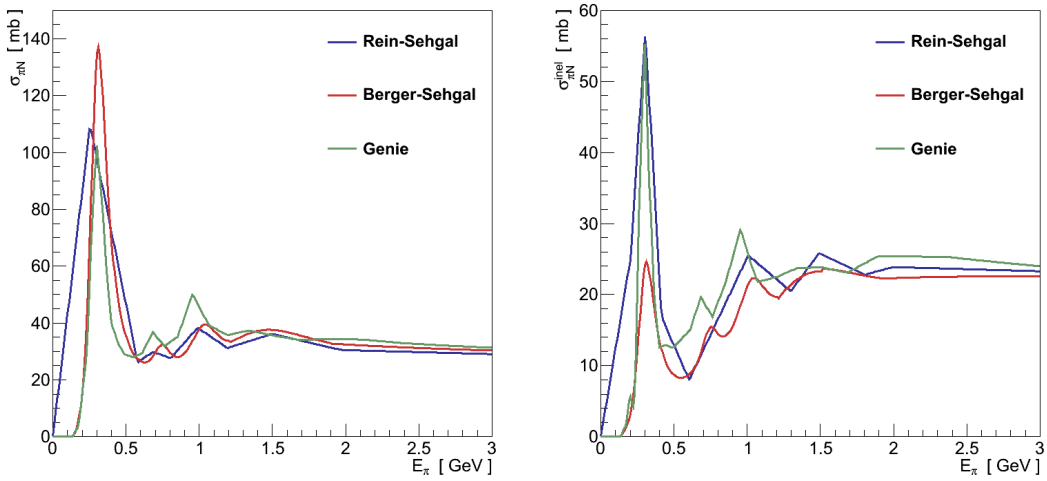

Figure 4.8: Comparison of the total (left) and inelastic (right) π-N cross-sections in the Rein-Sehgal paper and GENIE.

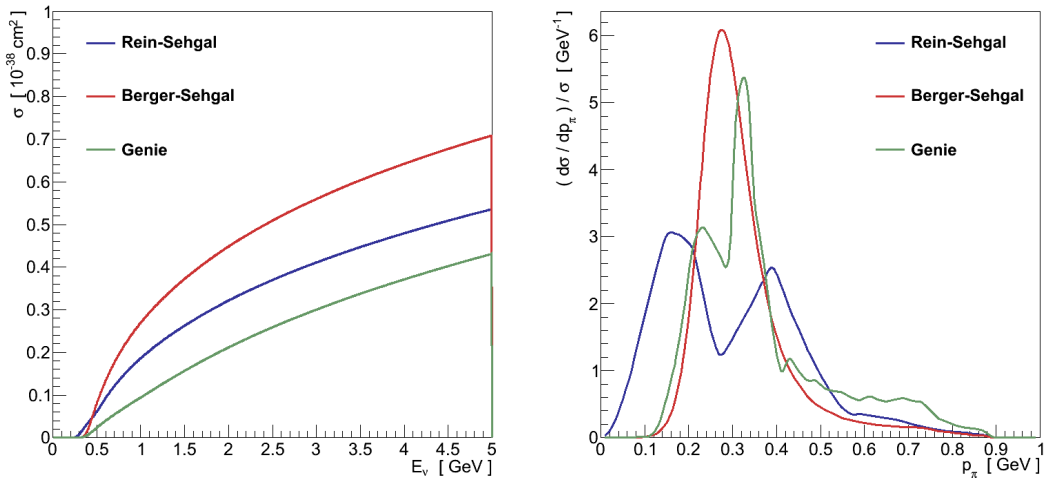

Figure 4.9: The effect of alternative parametrisations of the pion-nucleon cross-sections on the ν_μ CC coherent pion cross-section, and the pion momentum spectrum generated at $E_\nu = 1.0$ GeV, on ^{12}C.

likely to be un-physical, is the continuation of the cross-section down to $E_\pi = 0$ - a feature which becomes more significant at lower neutrino energies.

As can be seen in Figure 4.9, these different choices give vastly different total coherent cross-sections, essentially controlled by how high the total, and how low the inelastic, pion-nucleon cross-sections are. More importantly, they strongly affect the pion momentum distribution, which in turn could greatly impact an experiment's sensitivity. Note in particular the difference between the original Rein-Sehgal model (used by K2K and SciBooNE) and the more modern alternatives.

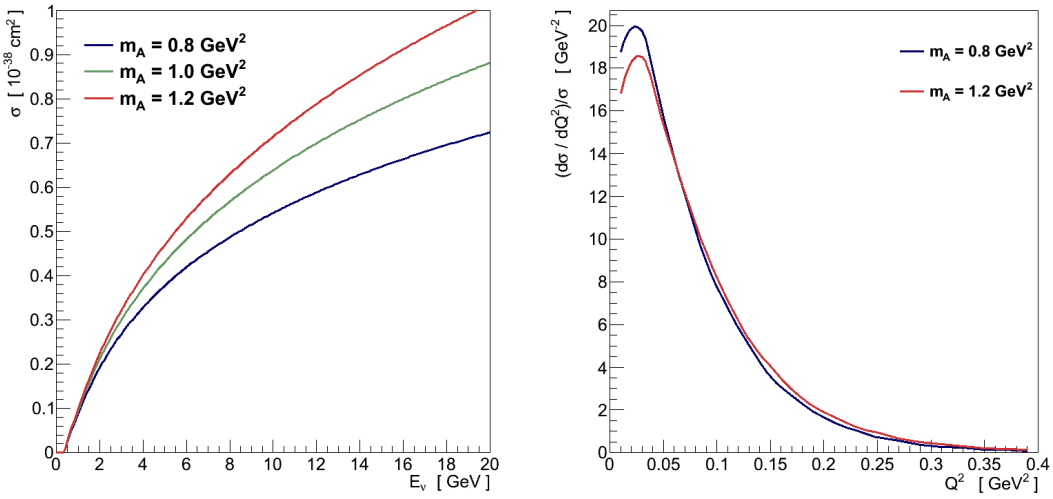

Figure 4.10: The effect of M_A on ν_μ CC coherent pion production on ^{12}C. The largest effect is on the total cross-section (left), but the normalised Q^2 distributions at $E_\nu = 1\,GeV$ (right) show that there is a also a subtle effect on the Q^2 shape.

The remaining inputs to the model are more simple to evaluate. The axial mass, M_A, mainly scales up the total cross-section, though it does make subtle changes to the shape of $d\sigma/dQ^2$ (Figure 4.10). Since existing coherent pion production data falls far short of being capable of constraining this value, M_A of 1.0 GeV is assumed by all implementations.

Likewise the dominant effect of the nuclear radius scale R_0 (Figure 4.11) is to scale the total cross-section, with larger values of R_0 resulting in smaller cross-sections. However, since it appears in the $e^{-R_0 A^{1/3}|t|}$ term it also affects the shape of the $|t|$ distribution, with higher values of R_0 causing the distribution to peak earlier and drop off faster. Although some past experiments have tried alternative values, the original Rein-Sehgal paper and every significant implementation in current use assumes R_0 to be 1.0 fm.

Finally the value of the $\Re/\Im$ ratio, r, exclusively scales the differential cross-section. The value of r was not stated in the original Rein-Sehgal paper and different implementations have taken different approaches. For example, GENIE and NEUGEN take the value to be 0.3, while NEUT and NUANCE have implemented r as a function of E_π. Using the GENIE value of 0.3 implies an increase in the total cross-section of around 10%, which is less than the resolution of the existing data.

Clearly, there can be large variations in the predictions of the Rein-Sehgal model depending on the choice of inputs used, both in the absolute cross-

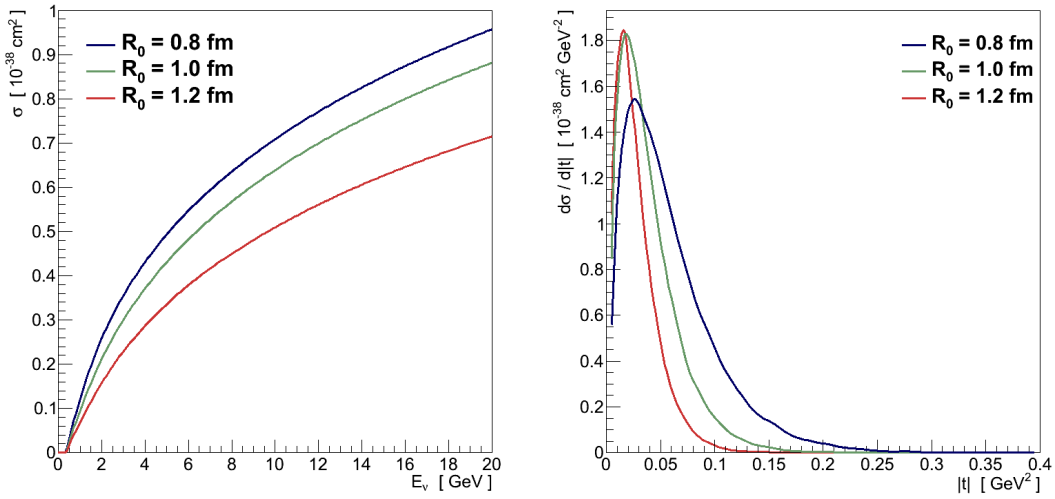

Figure 4.11: The effect of R_0 on ν_μ CC coherent pion production on ^{12}C. The largest effect is on the total cross-section (left), but the $|t|$ distribution at $E_\nu = 1\,GeV$ (right) is pushed to lower values as R_0 increases.

section and in kinematic distributions (particularly of the pion). It is important therefore, recalling Figure 4.5, when making statements about a measurement's compatibility with the Rein-Sehgal model, to keep in mind what version of the model was used in the analysis. However, even if the Rein-Sehgal model can accommodate the low energy data, it is unlikely to be able to do so while simultaneously maintaining compatibility with data at higher energies (Figure 4.4).

This is unsurprising since nuclear effects grow in importance at lower energies. It's questionable whether pion-nucleon cross-sections are appropriate to describe pion-nucleus scattering (Equation 4.27), and certainly any discrepancy in the pion-nucleon cross-sections used will become more significant at lower energies. In addition, the Adler PCAC theorem on which it is based is only valid at $Q^2 \approx 0$, which becomes a less valid approximation as the neutrino's energy becomes comparable in size to the pion mass.

Although it's unclear if the Rein-Sehgal model becomes invalid, and it has yet to be conclusively ruled out, it seems likely that an alternative model will be required to successfully describe coherent pion production at lower neutrino energies.

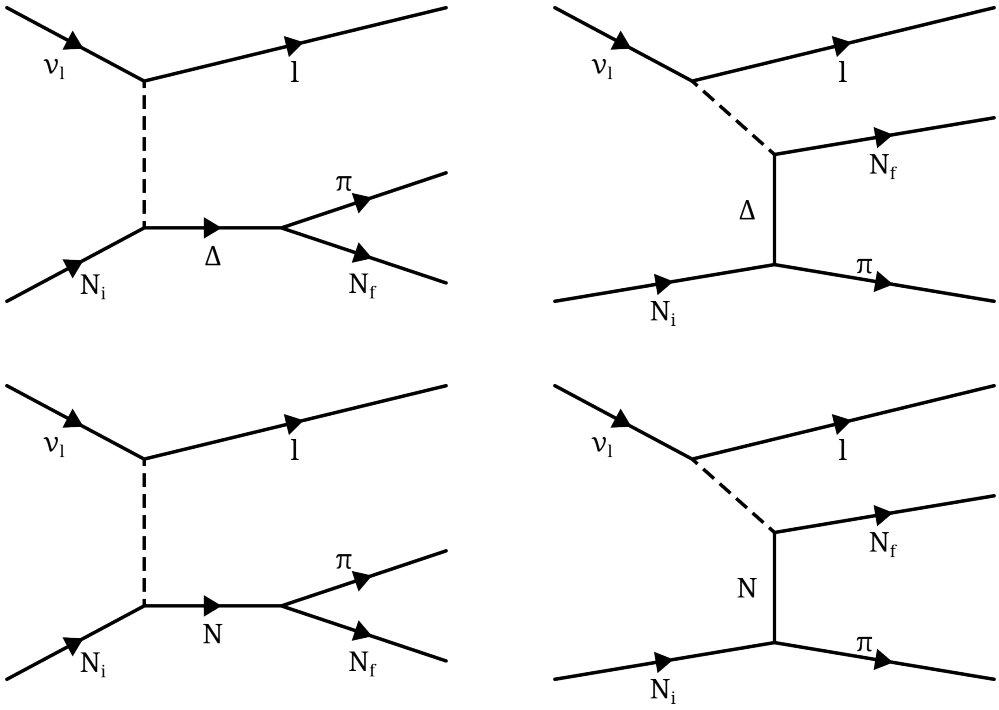

Figure 4.12: Feynman diagrams of the interaction processes which contribute to the Alvarez-Ruso cross-section. The interaction can utilise a Δ (top) or nucleon (bottom) propagator, and proceed via an s-channel (left) or t-channel (right) diagram.

4.3. Alvarez-Ruso Model

One such alternative is the Alvarez-Ruso model [53] [54] [55]. Unlike the Rein-Sehgal model, which is an example of a "PCAC model", the Alvarez-Ruso model is an example of a "microscopic model". Whereas PCAC models describe coherent pion production off of a nucleus in terms of a single interaction channel with that nucleus, a microscopic model describes the process in terms of a coherent sum of neutrino-nucleon interactions where the final-state nucleon is constrained to remain in the same quantum state.

The complete Alvarez-Ruso model includes four such neutrino-nucleon pion producing channels, shown in Figure 4.12, two of which involve the intermediate propagation of a Δ, and two the propagation of a nucleon. The first paper on the model described CC coherent pion production [53] [54], and included only the the s-channel Δ mode which dominates the reaction. This was extended to include the other three modes in the second paper on NC coherent [55], for which they become more relevant.

Two significant nuclear effects are also taken into account. First, the properties of Δ's, such as their mass and decay width, are modified by their presence inside a nuclear environment. Second, the outgoing pion is also affected by the nuclear environment, treated as a "distortion" of its wavefunction by a nuclear potential (this is effectively a more careful treatment of the pion absorption included in Rein-Sehgal, Equation 4.25, for low energy pions).

Based on the original papers and code provided by the authors, this Alvarez-Ruso model was implemented in the GENIE neutrino interaction simulation, for the purposes of comparison with the predictions from Rein-Sehgal. While alternative PCAC models have previously been implemented in interaction simulations, this represents the first such implementation of a microscopic model.

We begin by describing the Alvarez-Ruso model in the context of the original s-channel Δ description, then note the differences required for extending it to include all four-channels. The results of the implementation in GENIE are then compared with those from the Rein-Sehgal model, with a focus on the changes in experimental signatures.

4.3.1. The Model

The Alvarez-Ruso coherent pion production cross-section is expressed as a differential in the energy of the outgoing lepton, E_l, and the solid angles of the outgoing lepton and pion, Ω_l and Ω_π:

$$\frac{\mathrm{d}\,\sigma}{\mathrm{d}\,E_l\,\mathrm{d}\,\Omega_l\,\mathrm{d}\,\Omega_\pi} = \frac{1}{8}\frac{\left|\,p_l\,\right|\,\left|\,p_\pi\,\right|}{\left|\,p_\nu\,\right|}\frac{1}{(2\pi)^5}\left|\,\mathscr{M}\,\right|^2 \tag{4.28}$$

The three-momenta p_ν, p_l and p_π are those of the incoming neutrino, and outgoing lepton and pion respectively. Beginning with only the s-channel Δ production mode, the matrix element:

$$\mathscr{M}_{p\Delta^{++}} = \sqrt{3}\mathscr{M}_{n\Delta^{+}} = \sqrt{3}\frac{G_F}{\sqrt{2}}\cos\vartheta_C l_\alpha J^\alpha \tag{4.29}$$

is composed of a leptonic current, l_α, and a hadronic current, J^α. The factor $\sqrt{3}$ difference between the elements for the neutron and proton channels comes from isospin, and ϑ_C is the usual Cabibbo angle.

The leptonic current is the usual one for leptonic weak interactions:

$$l_\alpha = \overline{u}_l \left(\gamma_\alpha - \gamma_\alpha\gamma_5\right) u_\nu \tag{4.30}$$

with u_ν and u_l Dirac spinors for the initial neutrino and final-state lepton respectively.

The hadronic current is much more involved, and will be tackled in three steps. Beginning with the basic current for N W $\rightarrow \Delta$, then extending it to include the Δ decay W N $\rightarrow \Delta \rightarrow$ Nπ, and modifying the properties of the Δ in the nuclear medium. The distortion of the outgoing pion will be included last.

The basic hadronic current for N W $\rightarrow \Delta$ is:

$$J_\Delta{}^\alpha = \overline{\psi}_{\Delta\mu} A^{\mu\alpha} u_{\mathrm{N,i}} \tag{4.31}$$

where ψ_Δ is the Rarita-Schwinger spinor[1] for the Δ, $u_{\mathrm{N,i}}$ is the Dirac spinor for the initial nucleon, and as usual for composite particles the N-Δ coupling must be described with the use of form-factors:

$$\begin{aligned} A^{\mu\alpha} = & \left\{ \frac{C_3^V}{m_N}\left(g^{\mu\alpha}\gamma_\delta q^\delta - q^\mu \gamma^\alpha\right) + \frac{C_4^V}{m_N{}^2}\left(g^{\mu\alpha} q\cdot P_\Delta - q^\mu P_\Delta{}^\alpha\right) + \frac{C_5^V}{m_N{}^2}\left(g^{\mu\alpha} q\cdot P_{\mathrm{N,i}} - q^\mu P_{\mathrm{N,i}}{}^\alpha\right)\right\}\gamma_5 \\ & + \left\{ \frac{C_3^A}{m_N}\left(g^{\mu\alpha}\gamma_\delta q^\delta - q^\mu \gamma^\alpha\right) + \frac{C_4^A}{m_N{}^2}\left(g^{\mu\alpha} q\cdot P_\Delta - q^\mu P_\Delta{}^\alpha\right) + C_5^A g^{\mu\alpha} + \frac{C_6^A}{m_N{}^2} q^\mu q^\alpha \right\} \end{aligned} \tag{4.32}$$

The authors draw on various published values for these form-factors which are based on fits to electron and neutrino scattering data.

1. The Rarita-Schwinger equation is the spin-3/2 analogue of the spin-1/2 Dirac equation.

Equation 4.31 is then extended to cover both the production and decay of the Δ. The hadronic currents for W N $\rightarrow \Delta \rightarrow \pi$ N are:

$$J_{p\pi}{}^{\mu} = \sqrt{3} J_{n\pi}{}^{\mu} = \frac{f^{*}}{m_{\pi}} P_{\pi}{}^{\alpha} F\left(P_{\Delta}\right) \overline{u}_{\mathrm{N,f}} D\left(P_{\Delta}\right) \Lambda_{\alpha\beta} A^{\beta\mu} u_{\mathrm{N,i}} \tag{4.33}$$

The currents for the neutron and proton channels differ by a factor $\sqrt{3}$, again from isospin, giving a total difference between the channels of a factor 3. $\Lambda_{\alpha\beta}$ is the spin-3/2 projection operator, and the numerical factor $f^{*} = 2.13$ is required to reproduce the measured decay width of a free Δ. The Δ-Nπ vertex is described by a form-factor:

$$F\left(P_{\Delta}\right) = \frac{\lambda^{4}}{\lambda^{4} + \left(P_{\Delta}{}^{2} - m_{\Delta}{}^{2}\right)^{2}} \tag{4.34}$$

The value of $\lambda = 1.0\,\mathrm{GeV}$ comes from fits to resonance production data in electron and pion scattering.

The Δ propagator, $D(P_{\Delta})$, is:

$$D\left(P_{\Delta}\right) = \frac{1}{\left(W + m_{\Delta}\right)\left(W - m_{\Delta} + i\Gamma_{\Delta} \,/\, 2\right)} \tag{4.35}$$

With W the off-shell Δ's invariant mass, and $\Gamma_{\Delta}(E_{\Delta})$ its width. When in a nuclear medium a Δ acquires a self-energy as a consequence of two effects. First, the nucleon from the $\Delta \rightarrow$ N π decay is subject to Pauli-blocking (Section 3.6), reducing its decay width. Second, the potential for the Δ to interact with the surrounding nucleons, e.g. via absorption, affects both its mass and width. The values of m_{Δ} and Γ_{Δ} are modified to account for this, using an approach validated on pion, photon and electron scattering [56] [57]. This modification is a function of the local nuclear density, and therefore a function of position in the nucleus, and feeds into Equation 4.35.

Integrating Equation 4.33 coherently over all nucleons, the total hadronic current for the nucleus, A, is:

$$J_{\mathrm{A}\pi}{}^{\mu} = \frac{-i}{2}\int e^{i\left(\overrightarrow{q} - p_{\pi}\right)\cdot r}\left(\rho_p(r) + \frac{\rho_n(r)}{3}\right)\frac{f^*}{m_{\pi}} P_{\pi}{}^{\alpha} F\left(P_{\Delta}\right) D\left(P_{\Delta}\right) \mathrm{Tr}\left\{\bar{u}_{\mathrm{N,f}} \Lambda_{\alpha\beta} A^{\beta\mu} u_{\mathrm{N,i}}\right\} \mathrm{d}^3 r \tag{4.36}$$

where r is the three-vector position in the nucleus, and $\rho_{\mathrm{n,p}}$ are the densities of neutrons and protons. Finally, the effect of the nuclear environment on the outgoing pion is included, by substituting a more realistic wavefunction for the planewave solution used in Equation 4.36:

$$e^{-ip_{\pi}\cdot r} \rightarrow \varphi^*\left(p_{\pi}, r\right) \tag{4.37}$$

This wavefunction can take one of two forms. The full Alvarez-Ruso model calculates φ^* as the solution to the Klein-Gordan equation in an optical potential:

$$V_{\mathrm{optical}} = \frac{\Pi(r)}{2E_{\pi}} \tag{4.38}$$

where Π is a pion self-energy which is a function of nucleon density and hence position in the nucleus. This self-energy is calculated using the so called "Δ-hole" model [56], in which pion-nuclear interactions at these energies are dominated by the creation of Δ resonances. While well validated in other scattering fields, the Δ-hole model is only valid for π-N interactions with centre-of-mass energies around the Δ resonance, this limits the Alvarez-Ruso model's validity to $\mathrm{E}_{\nu} < 3.0\,\mathrm{GeV}$.

However, since solving the Klein-Gordon equation in a potential is a computationally expensive procedure, an alternative "eikonal" approximation was also assessed. Here the pion wavefunction is instead given by:

$$\varphi^*_{\mathrm{eikonal}} = e^{-ip_{\pi}\cdot r} \exp\left[-i\int_r^{\infty} \frac{\Pi(r')}{2p_{\pi}}\,\mathrm{d}\,r'\right] \tag{4.39}$$

using the same pion self-energy, Π, from before. The effect of these two choices is shown in Figure 4.13, for CC interactions on ^{12}C at $\mathrm{E}_{\nu} = 1\,\mathrm{GeV}$. The inclusion of either pion effect reduces the overall cross-section and shifts the pion momentum to lower values, both as a result of the optical potential strongly absorbing pions around the Δ resonance. The simpler eikonal model

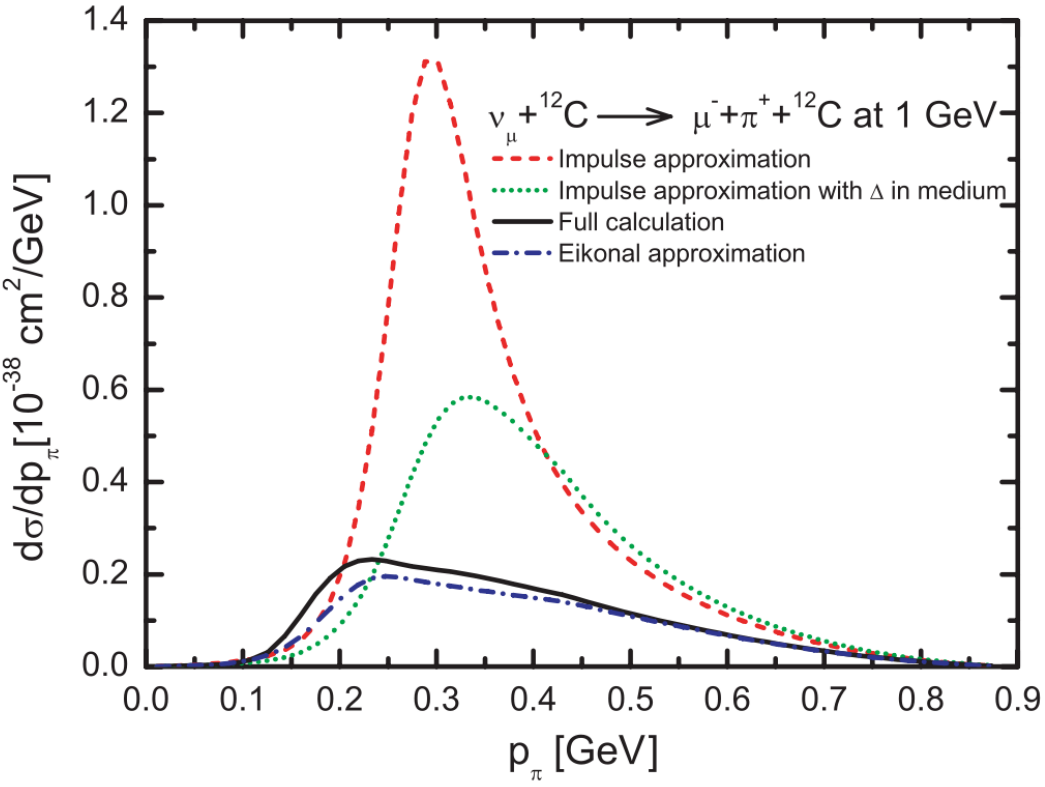

Figure 4.13: The effect of various nuclear effects on the pion momentum distribution. The red line includes no nuclear effects. The green line includes just the Δ self-energy. The black and blue lines are the full model with the Klein-Gordon and eikonal pion distortions respectively. From [54].

matches well the more complete Klein-Gordon calculation until p_π drops below around 0.25 GeV.

This completes all the ingredients of the model. To add the additional diagram for t-channel Δ production from Figure 4.12, the only substitution required is $P_{\Delta,s} = q + P_{N,i}$ becomes $P_{\Delta,t} = P_{N,i} - P_\pi$. The corresponding nucleon diagrams require additional changes. Clearly the appropriate masses must be used in Equation 4.34 and Equation 4.35, but no in-medium effects are required. The spin-3/2 projection operator and hadronic matrix are also replaced with:

$$\Lambda_{\alpha\beta} A^{\beta\mu} \rightarrow \gamma_\alpha \gamma_5 \left(\gamma_\delta P_N^{\ \delta} + m_N \right) B^\mu \tag{4.40}$$

Where B^μ is the nucleon analogue of $A^{\alpha\mu}$:

$$B^{\mu} = \gamma^{\mu} F_1 + \frac{i q_{\nu} \sigma^{\mu\nu}}{2 m_N} F_2 - \gamma^{\mu} \gamma_5 F_A - q^{\mu} \gamma_5 F_P \tag{4.41}$$

which should be familiar from Equation 3.25 and Equation 3.26. The values for the vector form-factors are taken from fits to electron scattering data [58], $\mathrm{F_A}$ takes the usual dipole form with $\mathrm{M_A} = 1.0\,\mathrm{GeV}$, and PCAC is used to relate it to $\mathrm{F_P}$ as in Equation 3.28. The total cross-section is then a coherent sum of the four resulting currents.

When making calculations for the neutral current channel the relevant changes due to the weak couplings need to be accounted for, a factor $\sqrt{2}$ on the vertices due to the coupling strength, and in the form-factors:

$$\begin{aligned} C_i^V &\rightarrow \left(1 - 2\sin^2\vartheta_W\right) C_i^V \\ F_i^V &\rightarrow \left(1 - 2\sin^2\vartheta_W\right) F_i^V \end{aligned} \tag{4.42}$$

4.3.2. Comparison with Rein-Sehgal

Utilising the original papers describing this model, the references therein, and the original Fortran implementation developed by the authors, the Alvarez-Ruso model was re-implemented into the GENIE interaction simulation (version 2.6.6).

For the treatment of the outgoing pion distortion the simpler eikonal approximation was used. Computationally, the eikonal approximation is significantly less intensive, which is an important consideration for interaction simulations being utilised in experiments. Although the approximation under-predicts the full calculation at lower pion momenta (Figure 4.13) the shape, which in many respects is more important for experiments, is very similar.

Initially the model was implemented as standalone C++ and validated against the authors' original code. This was then interfaced into the GENIE framework, to enable the generation of events for comparison with GENIE's Rein-Sehgal model. Below, such a comparison is made of their respective predictions for ν_μ induced CC coherent pion production on ^{12}C.

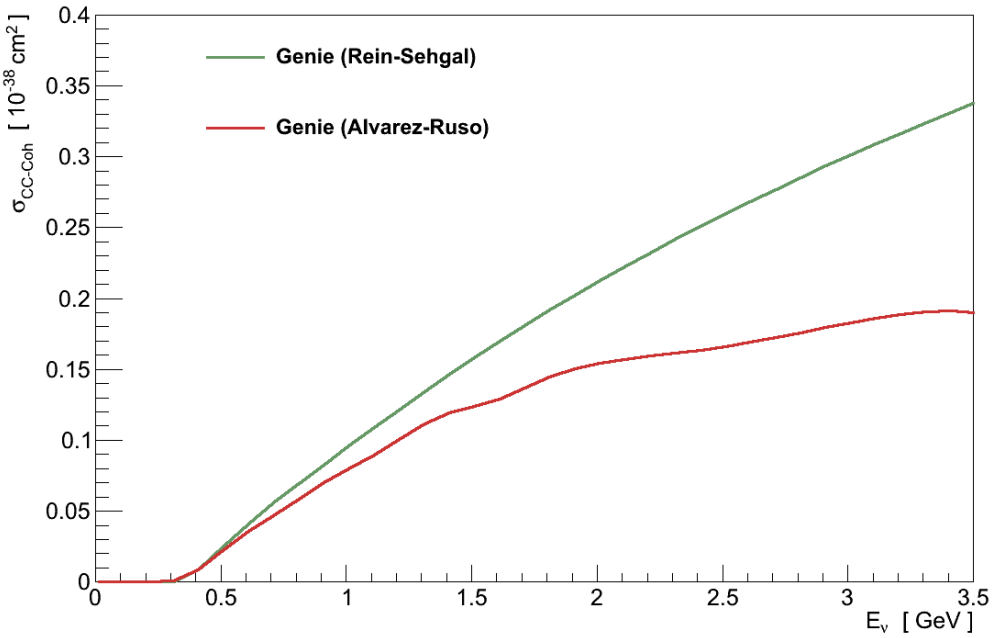

Figure 4.14: Comparison of the total ν_μ CC coherent pion production cross-sections on ^{12}C from Rein-Sehgal and Alvarez-Ruso.

Figure 4.14 shows the total cross-sections predicted by both models. The Alvarez-Ruso model gives a lower cross-section than Rein-Sehgal, which is a first requirement to explain the K2K, SciBooNE and MiniBooNE results. The difference becomes increasingly extreme as the energy increases, though this is also where the validity of the Alvarez-Ruso model drops off.

The remaining comparisons of the models' differential distributions are all made at $E_\nu = 1.0\,\text{GeV}$, which is comparable to the energies of many recent and current experiments, and where the Alvarez-Ruso model is completely valid. Figure 4.15 shows the momentum distributions predicted by the two models, which are broadly similar overall. The Alvarez-Ruso model's pion distortion results in a smoother pion momentum distribution than for Rein-Sehgal. It is also slightly softer on average, and if the full Klein-Gordon solution was used for the pion distortion the spectrum would be softer still. This in turn results in a correspondingly smooth, and slightly harder muon momentum spectrum. The double peak structure seen in Rein-Sehgal, as a result of the structure in the pion-nucleon cross-sections, is not reproduced by Alvarez-Ruso which models only one type of pion interaction.

Figure 4.16 shows the models' angular distributions, the most significant difference being that the pion angular distribution is more forward peaked in the Alvarez-Ruso model. This is also true, to a lesser extent, in the muon

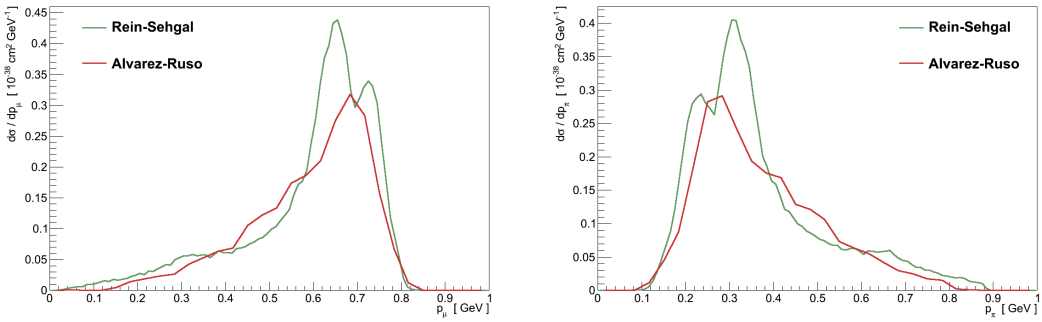

Figure 4.15: Comparison of p_μ (left) and p_π (right) from Rein-Sehgal and Alvarez-Ruso on ^{12}C at $E_\nu = 1.0\,GeV$.

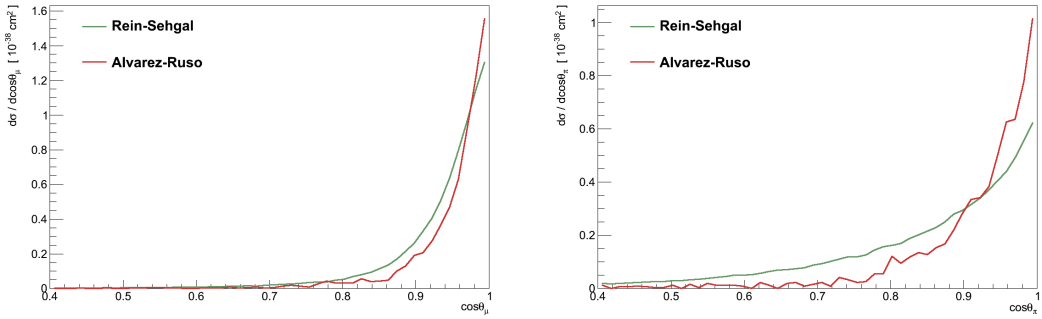

Figure 4.16: Comparison of $\cos\vartheta_\mu$ (left) and $\cos\vartheta_\pi$ (right) from Rein-Sehgal and Alvarez-Ruso on ^{12}C at $E_\nu = 1.0\,GeV$.

angle. One possibility for this difference could be the fact that the Alvarez-Ruso model requires the entire momentum transfer to the nucleus to be absorbed by a single nucleon - which must remain in the same quantum state after the interaction - while Rein-Sehgal allows the entire nucleus to recoil. Reducing the momentum which can be transferred to the nucleus would in turn reduce the scattering angles.

Finally the |t| distribution, which is the characteristic experimental signature of coherent interactions is shown in Figure 4.17. Predominantly as a result of its more forward-going preference, though also due to its slightly softer pion momentum spectrum, the Alvarez-Ruso model predicts a distribution more sharply peaked at lower values than Rein-Sehgal. It is useful to note that any search for coherent pion production at low |t| developed using Rein-Sehgal would be at least as sensitive to the Alvarez-Ruso model.

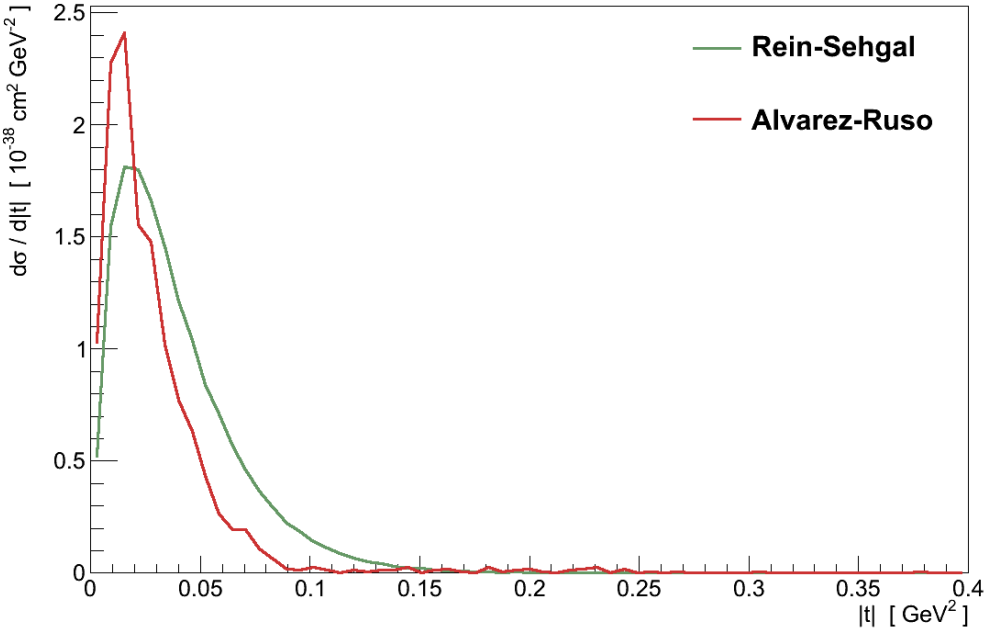

Figure 4.17: Comparison of the |t| distributions from Rein-Sehgal and Alvarez-Ruso on ^{12}C at $E_\nu = 1.0\,\text{GeV}$.

4.4. Other Models

Before concluding the chapter a brief comparison with other models is made. This is achieved by utilising data from a recent study [59], comparing alternative neutrino-nucleus interaction models, which made the model predictions gathered publicly available[2].

Figure 4.18 shows the total CC cross-section and pion momentum distributions predicted by these models on ^{12}C at $E_\nu = 1.0\,\text{GeV}$.

Rein-Sehgal, Berger-Sehgal [52], and Schalla-Paschos [60] are all examples of PCAC based models. Amongst other differences, the latter two implement more realistic descriptions of the pion-nucleus interactions. Hernandez [61] and Nakamura [62] are both examples of microscopic models similar to the Alvarez-Ruso model described here.

It was noted in the comparison study, that a large part of the differences in total cross-section could be attributed to different choices of axial-vector

2. To aid comparison, the GENIE and Alvarez-Ruso data from the original study have been replaced with the predictions calculated here.

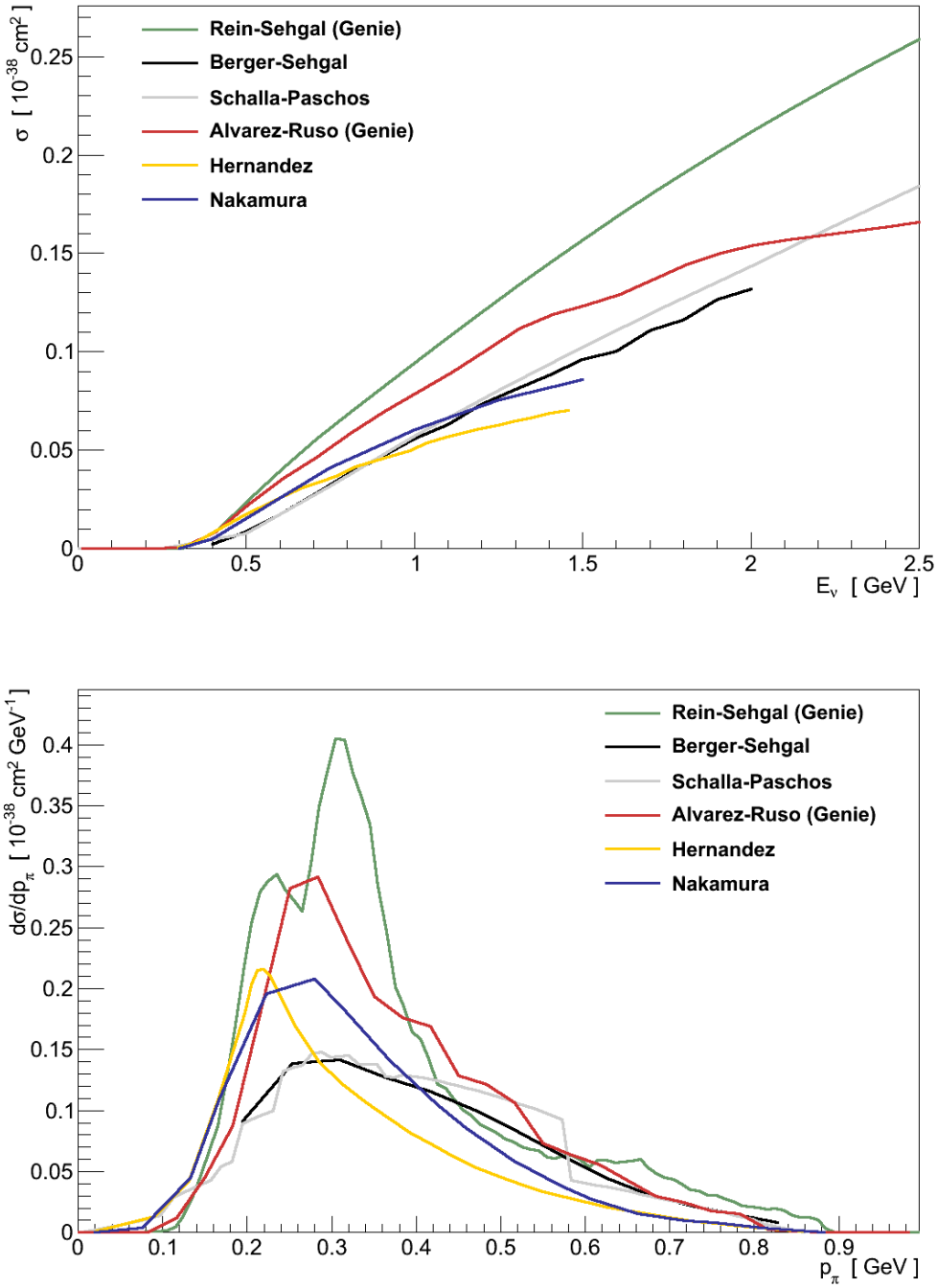

Figure 4.18: Overview of predictions for ν_μ CC coherent pion production on ^{12}C. (top) The total cross-section. (bottom) The p_π distribution at $E_\nu = 1$ GeV.

form-factors. Even so there are few notable features, either in the total cross-section or pion momentum, which would allow experimental discrimination between the models without precise differential data. However, the comparison study did not gather angular differential cross-sections which in Section 4.3.2 appeared to provide a more discernible difference between the PCAC and microscopic models.

4.5. Summary

Neutrino induced coherent pion production is an important channel for neutrino physics to understand, both because of its potential to be a background in ν_e oscillations and for its integral part in our understanding of total pion production.

The signals seen in high energy experiments show remarkably clear signatures of the process, leaving no doubt of its existence. And the coherent model of Rein-Sehgal matches well those distributions in multiple experiments.

However it has been found across many neutrino-nucleus interaction channels that at low neutrino energies nuclear effects come into play and old assumptions break down. So it is unsurprising that recent low energy searches for coherent pion production reported either limits or significantly reduced cross-sections with respect to Rein-Sehgal.

Nevertheless, it is worth noting that:

- K2K reported their CC coherent limit at $E_\nu \sim 1.3\,\mathrm{GeV}$ using an early version of the model which did not take account of the muon's mass.
- Both SciBooNE and K2K searched for CC coherent in the Q^2 distribution, instead of the more characteristic $|t|$.
- The cross-section and pion kinematics predicted by the Rein-Sehgal model can vary significantly depending on the inputs used.

so it may be premature to completely rule out the Rein-Sehgal model.

Still, difficulty in achieving simultaneous agreement with data at high and low energies, coupled with frailties of Rein-Sehgal at lower energies, suggest an alternative model may be required. One such alternative is the Alvarez-Ruso microscopic model, which was implemented in GENIE. In comparisons with Rein-Sehgal it was found to give a lower cross-section, smoother momentum distributions, and more forward-peaked angular and $|t|$ distributions. There are several other models on offer however, at present, existing experimental data is nowhere near sufficient to discriminate between them.

New data on coherent pion production is necessary. The T2K experiment delivers an intense ν_μ beam through a near detector designed, in part, for neutrino interaction studies. This presents an ideal opportunity to contribute to the understanding of coherent pion production.

5. The T2K Experiment

T2K [63] is a long-baseline neutrino oscillation experiment designed to make precision measurements of ϑ_{13}, ϑ_{23} and Δm^2_{32}. It does this by firing a beam of mostly ν_μ along a baseline of 295 km and measuring the resulting ν_μ and ν_e energy spectra.

The ν_μ beam is generated at the J-PARC facility in Tokai, on the East coast of Japan, and detected by the famous Super-Kamiokande water-Cherenkov detector near Kamioka. The Super-Kamiokande detector is well suited for this task. Its 50 kT water volume ensures a sufficient number of the neutrinos which reach it will interact, and reconstructing a primary lepton's Cherenkov ring allows it to determine the timing, direction, energy and flavour of the incident neutrino. Timing and direction are essential to identify the neutrino's origin as being the T2K beam, while flavour and energy are required to measure the energy spectra for ν_μ and ν_e separately. T2K is also notable as the world's first off-axis neutrino experiment with the J-PARC beam directed such that the far-detector is 2.5 ° off the beam's axis.

In addition to the production and detection of neutrinos, the experiment requires several other studies.

The beam's direction, normalisation and energy spectrum all need to be known accurately to correctly predict the un-oscillated flux at Super-Kamiokande. For example, a shift of the beam direction by 1 mrad would result in a ~20 MeV change in the peak of the neutrino energy spectrum[1]. In addition, the initial beam is not composed purely of ν_μ but also contains small amounts of $\bar{\nu}_\mu$, ν_e and $\bar{\nu}_e$. It is important for T2K to know this flavour composition if it is to separate those in the initial beam from those that appear due to oscillations. Since the beam direction is determined by the state of the hardware and, as will be discussed briefly in Section 5.1, neutrino production is difficult to simulate, all of these need to be determined experimentally.

Additionally, as discussed in previous chapters, T2K will need a good knowledge of neutrino-nucleus interactions if it is to successfully understand

1. This can be determined from Figure 5.5, where the fluxes at 2.5 ° and 2.0 ° peak at approximately 0.6 GeV and 0.75 GeV respectively.

selection efficiencies, reconstruction of neutrino energies and backgrounds. Since there is so little data over T2K's neutrino energy range this also needs to be done experimentally. Finally, because photons can mimic an electron at Super-Kamiokande, NC π^0 production is a particularly dangerous background for ν_e detection, so the cross-section for this process in water needs to be accurately determined.

In order to satisfy these requirements T2K built a near-detector facility 280 m downstream of the beam target which contains two separate detectors (Figure 5.1). The on-axis "INGRID" is primarily responsible for measuring the beam's normalisation and direction, while the off-axis "ND280" [2] measures the beam's flavour composition, and studies neutrino-nucleus interactions including NC π^0 production.

5.1. The J-PARC Neutrino Beam

The Japanese Proton Accelerator Research Complex (J-PARC) in Tokai on the East coast of Japan is a new facility built on the site where Japan developed their first nuclear reactors (Figure 5.2). The accelerator chain begins with a linear accelerator (LINAC) which boosts H^- ions up to a kinetic energy of 181 MeV before passing through charge-stripping foils. The resulting protons are then injected into a 3 GeV Rapid-Cycling Synchrotron (RCS) which in turn feeds a 30 GeV Main Ring (MR) from which the protons destined for the neutrino beamline are extracted.

Fast kicker magnets extract protons from the MR so that they can be bent inside the ring and along the neutrino beamline. As they approach the target the protons are focused and directed downwards by 3.6 ° with respect to the horizontal. Although the direction to Super-Kamiokande is actually only 1.3 ° downwards, this additional vertical offset forms part of the 2.5 ° off-axis angle of Super-Kamiokande with respect to the beam.

2. T2K's naming convention for "ND280" is ambiguous, and is used to refer both to the entire near detector complex and specifically to the off-axis near detector. In this thesis I refer to the former as the "near detector complex", reserving "ND280" exclusively for the off-axis near detector.

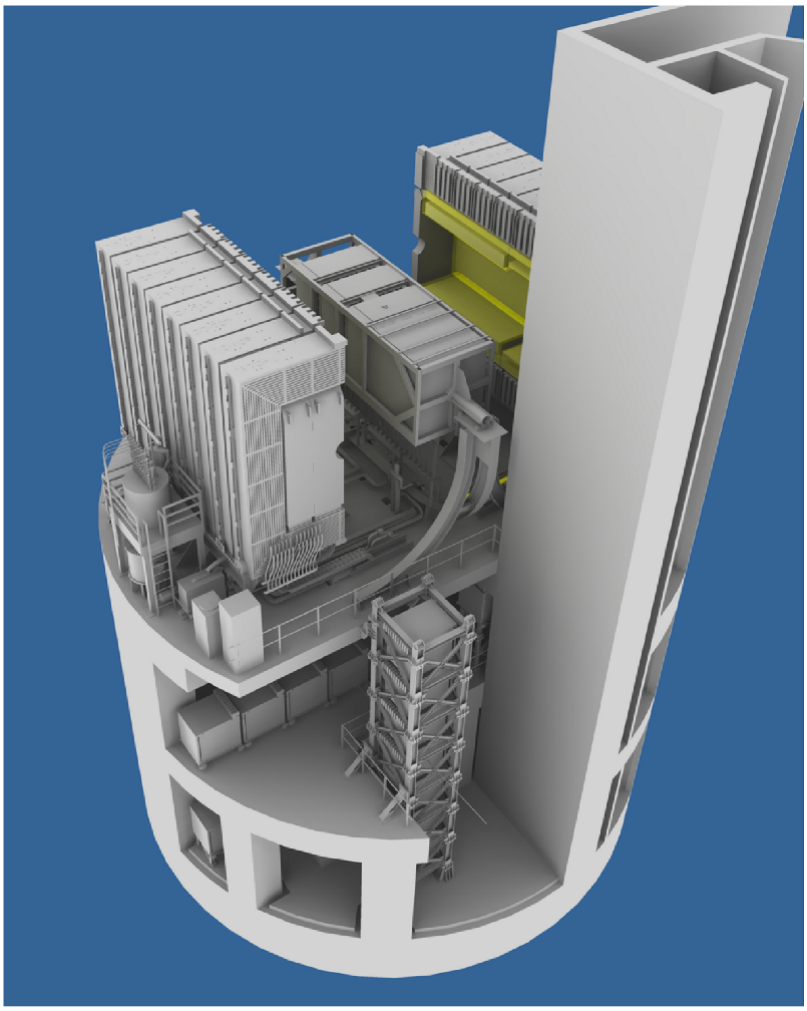

Figure 5.1: The near detector complex. On the top floor stands the off-axis ND280, shown with the magent open to expose the inner detectors. The floor below holds the horizontal arm of INGRID, in-front of which stands the vertical arm. [63]

The protons then collide with the target which is a graphite rod 914 mm long and 26 mm in diameter, with a density of 1.8 g cm^{-3}. It is cooled with helium gas and is designed to operate at a beam power of 750 kW, though to date the maximum delivered has been 200 kW.

The target is located inside the first of three magnetic horns which select and focus the secondary particles (mostly π^+) produced in the target (Figure 5.3). The first horn is primarily responsible for "collecting" the pions, while the second and third horns further downstream focus them down a 96 m decay volume.

Positive pions are the most common neutrino-producing particles which enter the decay volume though there are also a significant number of positive kaons. In addition, a small number of wrong-sign pions and kaons are unavoidable

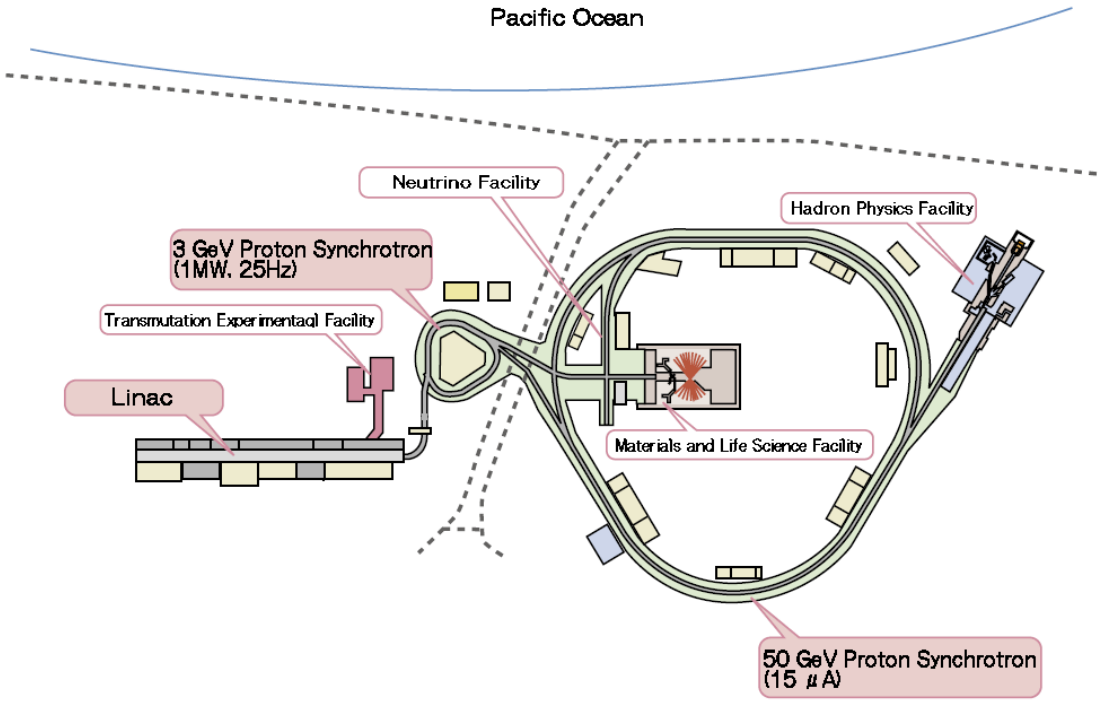

Figure 5.2: An overview of the J-PARC accelerator chain [http://j-parc.jp]

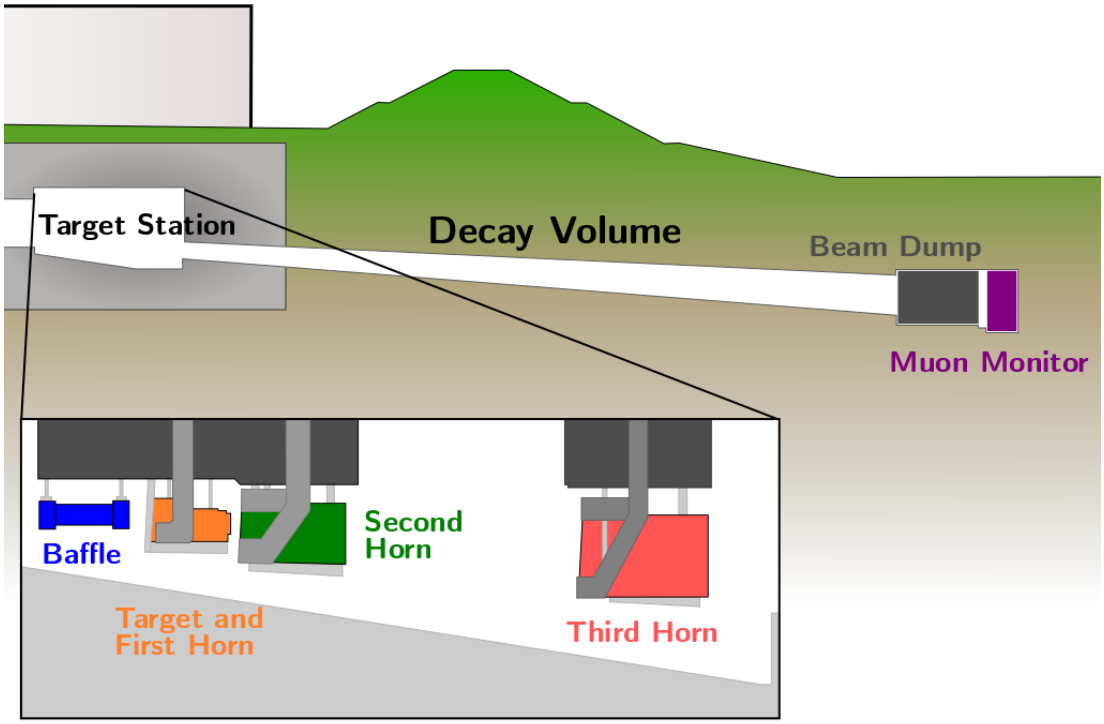

Figure 5.3: Schematic of the neutrino-beamline from the target onwards.

Neutrino	Decay	Fraction (%)
ν_μ	$\pi^+ \to \mu^+ \nu_\mu$	73
	$K^+ \to \mu^+ \nu_\mu$	13
	$K^+ \to \pi^0 \mu^+ \nu_\mu$	12
	$K^0 \to \pi^0 \mu^+ \nu_\mu$	2
	$\mu^- \to e^- \bar{\nu}_e \nu_\mu$	0.02
$\bar{\nu}_\mu$	$K^- \to \mu^- \bar{\nu}_\mu$	42
	$K^- \to \pi^0 \mu^- \bar{\nu}_\mu$	21
	$\pi^- \to \mu^- \bar{\nu}_\mu$	14
	$K^0 \to \pi^0 \mu^+ \bar{\nu}_\mu$	13
	$\mu^+ \to e^+ \nu_e \bar{\nu}_\mu$	9
ν_e	$K^+ \to \pi^0 e^+ \nu_e$	50
	$\pi^+ \to e^+ \nu_e$	38
	$K^0 \to \pi^- e^+ \nu_e$	8
	$\mu^+ \to e^+ \nu_e \bar{\nu}_\mu$	4
$\bar{\nu}_e$	$K^- \to e^- \bar{\nu}_e$	57
	$K^0 \to \pi^+ e^- \bar{\nu}_e$	33
	$\pi^- \to e^- \bar{\nu}_e$	9
	$\mu^- \to e^- \bar{\nu}_e \nu_\mu$	2

Table 5.1: The fraction of each decay mode which contributes to neutrinos of each neutrino flavour under the flux peak ($0.4\,\text{GeV} \leq E_\nu \leq 1.0\,\text{GeV}$)

and it is also possible for μ^+ produced from π^+/K^+ decays to also decay and contribute to $\bar{\nu}_\mu$ and ν_e contaminations (Table 5.1).

The decay volume ends 117.5 m from the target with two muon monitoring detectors which provide valuable data for validating the beam simulation.

One of the notable features of the T2K neutrino beam is that it is the world's first off-axis neutrino beam. As was mentioned earlier, the beam is directed such that the Super-Kamiokande detector is situated 2.5° off the

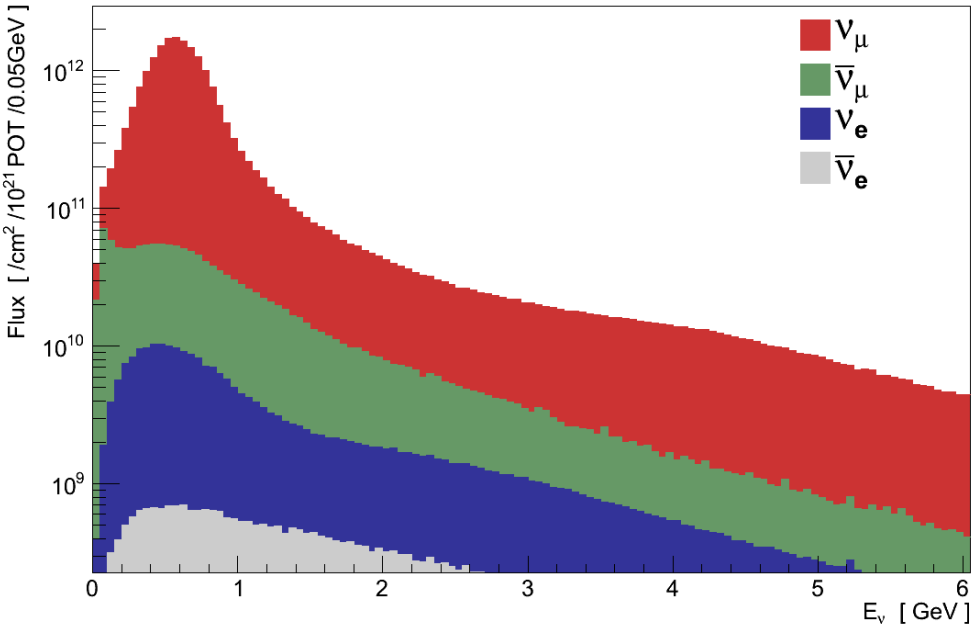

Figure 5.4: Simulated neutrino flux at ND280 as a function of neutrino energy.

beam's primary axis. Directly along the beam's axis, a detector is exposed to a broad range of decay kinematics giving a correspondingly broad neutrino energy spectrum. At fixed angles off-axis however, only a more select range of decay kinematics contribute resulting in a beam with a much narrower energy spectrum (Figure 5.5). There are two good reasons for doing this. The first is that the peak of an off-axis spectrum is lower than for an on-axis beam, allowing T2K to push the peak energy down towards the oscillation maximum energy of ~600 MeV - giving higher statistics where it matters most. The second advantage comes from the removal of a large flux of higher energy neutrinos. These neutrinos do not contribute to the oscillation signal at Super-Kamiokande but will generate background interactions - in particular NC interactions - which can be reconstructed in the signal region. For oscillation analyses then, an off-axis beam delivers higher statistics with lower backgrounds.

At the end of T2K Run 4, in May 2013, the beam had delivered a total of 2.57 $\times$ 10^{20} POT (Table 5.2). This is delivered in ~5 µs long "spills" of 8 (6 in T2K Run 1) "bunches" each of which is approximately 15.0 ns wide (Figure 5.6).

Although designed to take a currents of 320 kA, thus far all T2K physics data has been taken while operating the horns at 250 kA, with the exception of T2K Run 3b when they were operated at 205 kA. The effect of this reduction in

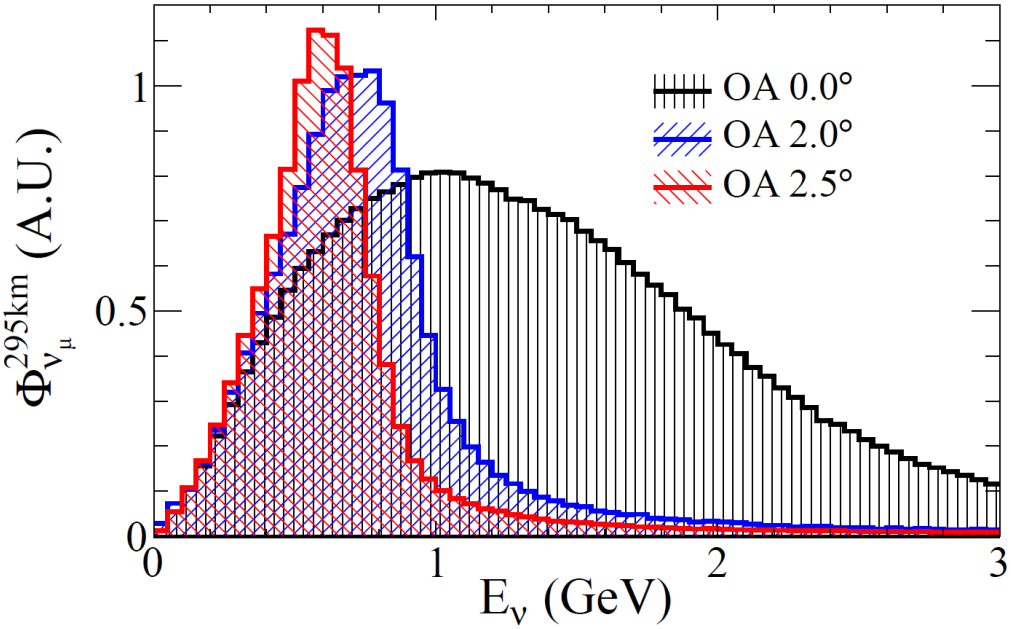

Figure 5.5: The effect of moving off-axis on the ν_μ energy spectrum. [64]

T2K Run	Bunches per Spill	Horn Current (kA)	Run POT (10^{20})	Total POT (10^{20})
1	6	250	0.31	0.31
2	8	250	1.12	1.43
3b	8	205	0.22	1.65
3c	8	250	1.37	3.02
4	8	250	3.37	6.40

Table 5.2: Conditions and performance of the T2K beam up to May 2013.

horn current is mainly a reduction of around 10 % in the total flux at the peak (Figure 5.7)·

5.2. Super-Kamiokande

Super-Kamiokande is perhaps the most famous experiment in the history of neutrino physics and played an important part in establishing evidence for both solar and atmospheric neutrinos oscillating. It also holds the world's

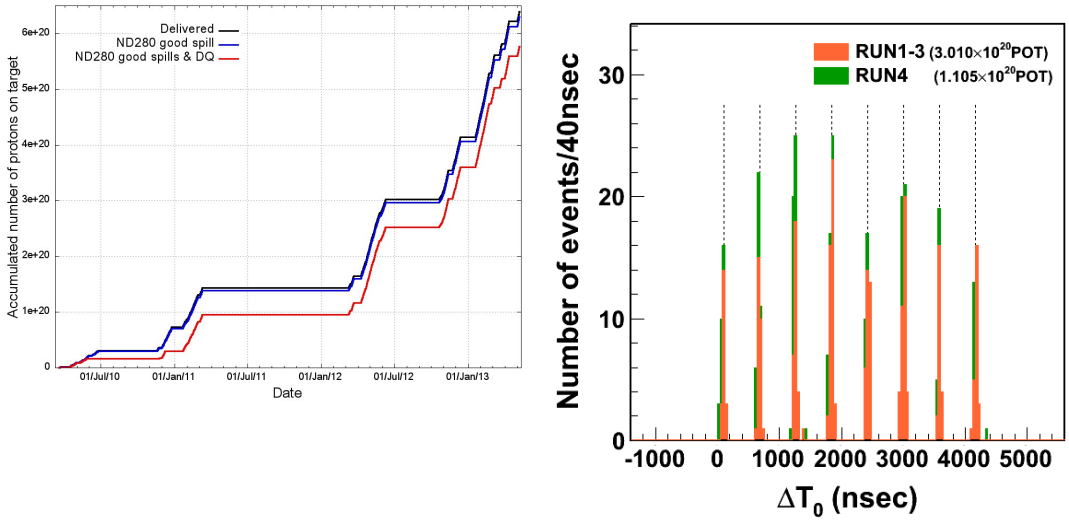

Figure 5.6: (left) The POT delivered by the beam up to the end of T2K Run 4 in May 2013, and the amount of that recorded by ND280. (right) The 8 bunch structure of a beam spill with respect to the beam trigger can be clearly seen in Super-Kamiokande's initial ν_e selection. [T2K official plots]

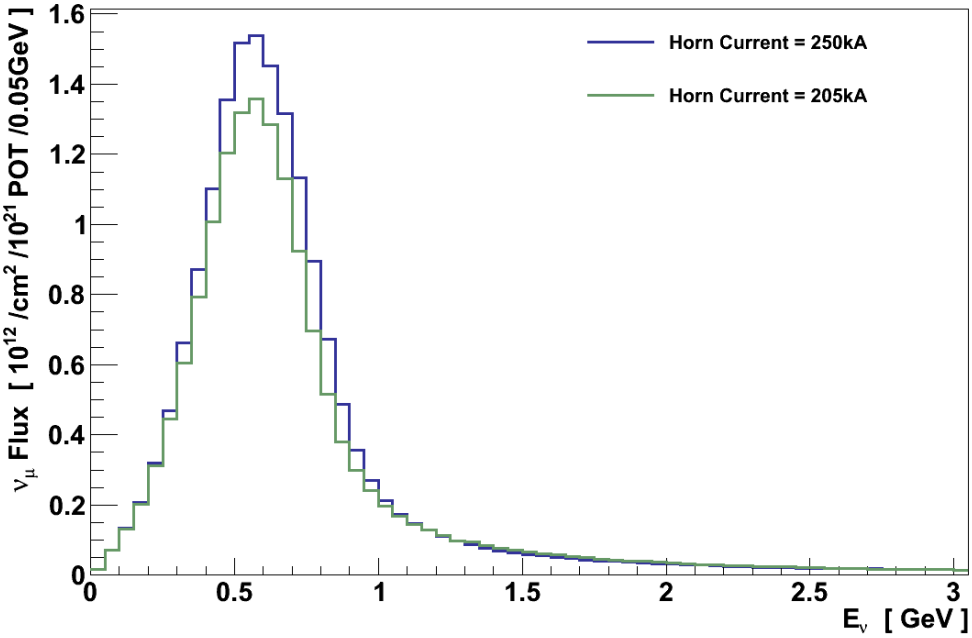

Figure 5.7: The effect of changing the horn current on the ν_μ flux at ND280.

leading limit on proton decay [65]. Now in it's fourth running configuration, Super-Kamiokande is being re-utilised as the far detector for T2K.

The device itself is a large water-Cherenkov detector within a vertical cylindrical tank. A stainless steel frame forming a smaller cylinder within the tank separates the volume into two regions known as the inner and outer

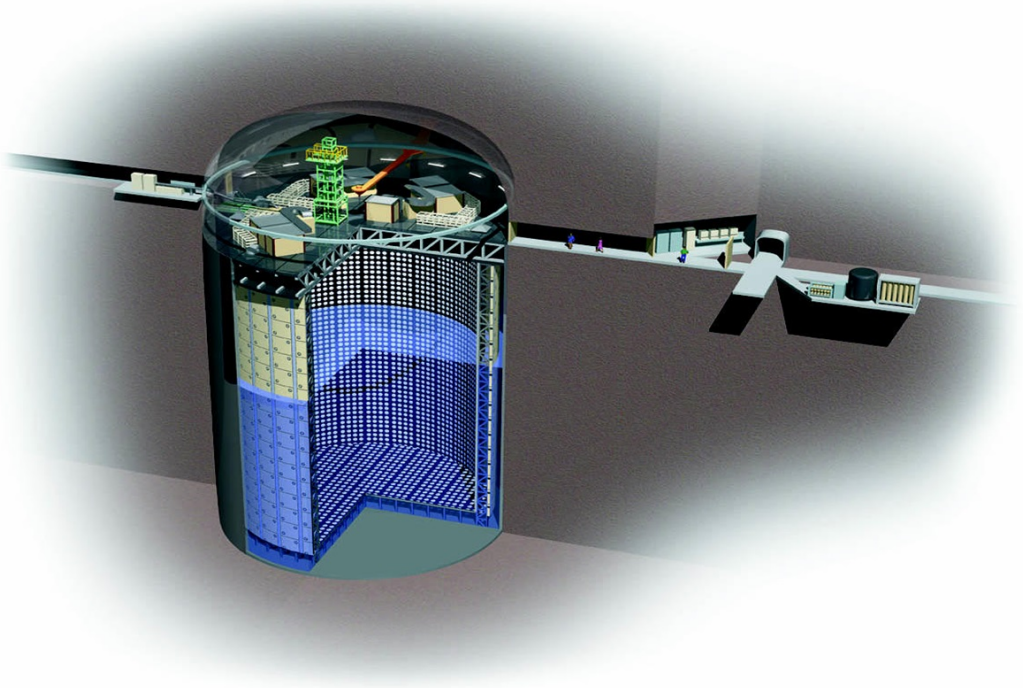

Figure 5.8: Schematic of the Super-Kamiokande detector. [http://www-sk.icrr.u-tokyo.ac.jp/sk/index-e.html]

detectors. The entire volume is filled with 50 kT of ultra-pure water though, in practice, the fiducial mass is somewhat smaller.

The inner detector is the target region, and it is instrumented on all sides by 11129 inward-facing photo-multiplier tubes (PMTs) which cover ~40 % of the surface area. Particles produced in the inner detector which are above the Cherenkov threshold produce rings of light which can be detected by these PMTs and from which the event can be reconstructed. The position of the interaction vertex can be determined from the position, shape and diameter of the ring. The thickness of the light ring is a measure of the distance the particle travelled, with exiting particles generating a completely filled circle. Finally, primitive particle identification for separating showering and non-showering particles (effectively electron-muon separation) can be done using the diffuseness of the outer part of the ring (Figure 5.9). It is the fact that this particle identification cannot discriminate between a showering electron or photon that makes NC π^0 production such an important background for ν_e selection.

The outer detector was designed as a veto for incoming (mostly cosmic-ray) particles and is essentially a 2 m thick region surrounding the inner detector. The outwards facing wall is also instrumented with PMTs albeit much more

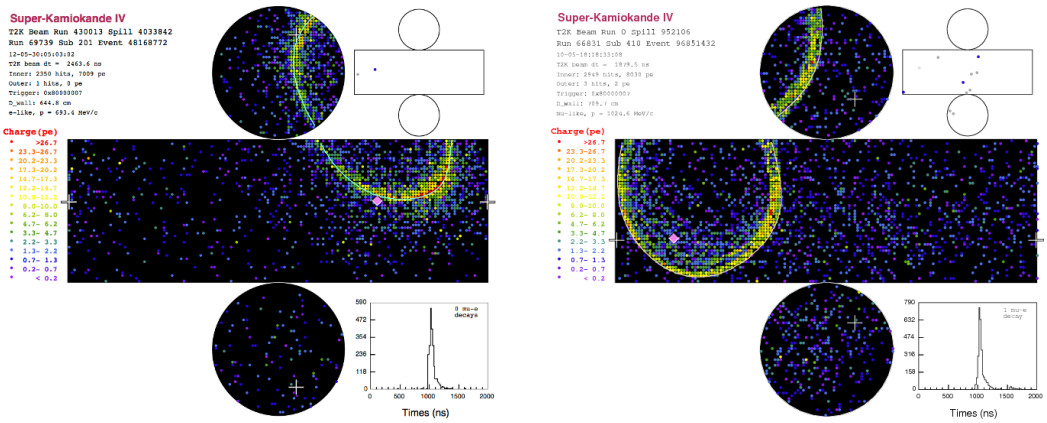

Figure 5.9: Event displays from T2K beam interactions in Super-Kamiokande. The outer part of the Cherenkov ring resulting from an electron (left) is much "fuzzier" than one from a muon (right). [T2K official plots]

sparsely - the tubes are fewer and smaller. In T2K however, because the direction and timing requirements are already quite effective at selecting beam events, interactions in the outer detector can also contribute to the oscillation analysis.

- Inner Detector:
  - 11129 × 0.5 m diameter PMTs
  - Cylindrical volume 33.8 m diameter, 36.2 high
- Outer Detector:
  - 1885 × 0.2 m diameter outward-facing PMTs on inner wall
  - Cylindrical tube, outer diameter 39 m, inner diameter ~34.3 m

5.3. INGRID

The Interactive Neutrino Grid (INGRID) [66] is the on-axis near detector primarily designed to constrain the beam normalisation and direction. It achieves this by placing identical modules at a variety of off-axis angles in a plane perpendicular to the beam. The direction can then be determined from the beam's profile across this plane, and the normalisation from the rate of interactions.

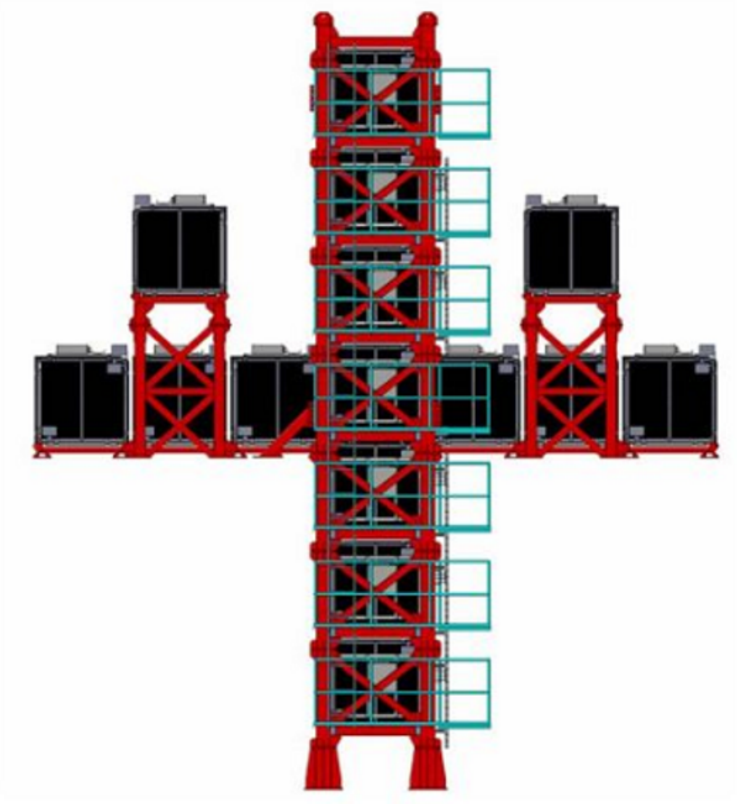

Figure 5.10: The layout of the INGRID modules. 14 modules are arranged in a cross-shape: 7 vertical modules in front of 7 horizontal modules. 2 additional modules are placed in off-axis positions. The proton module is located in the centre of the cross, between the vertical and horizontal arms. [63]

The baseline design consists of 16 identical modules (Figure 5.10). 14 of these are placed in a 10 m $\times$ 10 m cross-shape, centred on the beam's axis. This is formed of a vertical stack of 7 modules, which sits in front of a horizontal row of a further 7 modules. In between these two sets are two modules located above the horizontal row and on either side of the vertical stack. These off-axis modules assist in characterising any asymmetries in the beam shape - which is important for an off-axis beam.

Each standard module is primarily constructed of a central tracking region surrounded by veto planes (Figure 5.11). The tracking region is approximately 1.2 m square and is comprised of 9 $\times$ 65 mm thick iron plates, separating the first 10 of 11 planes of plastic scintillator. Each of these planes contains 2 layers of 10 mm $\times$ 50 mm bars arranged in an x-y configuration. The central tracking region is surrounded above, below and on the sides by veto planes of 22 plastic scintillator bars aligned perpendicular to the beam.

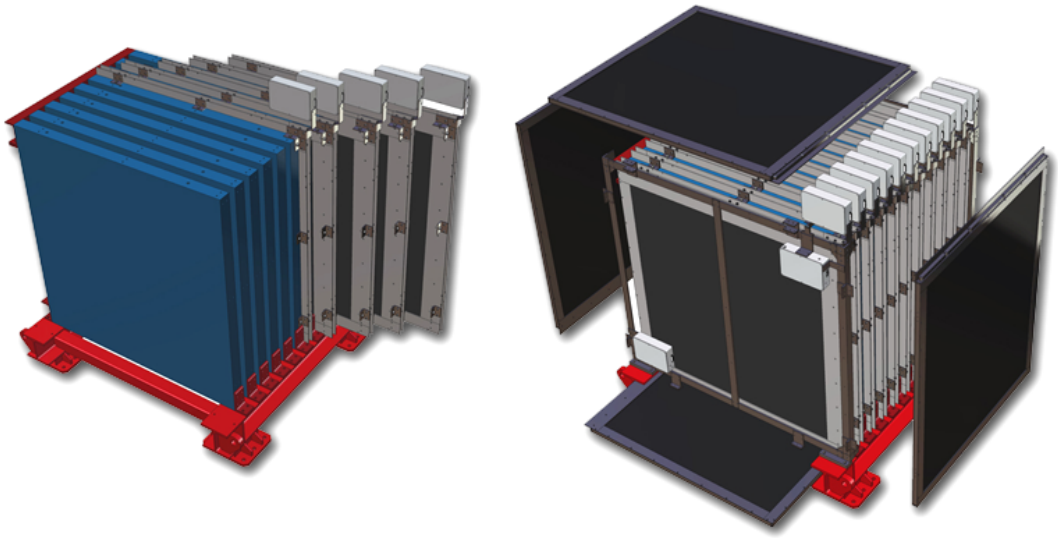

Figure 5.11: An exploded view of one of the standard INGRID modules. The left diagram shows the central tracking region consisting of 9 iron plates and 11 x-y scintillator planes. The right diagram shows the addition of the surrounding veto planes. [63]

Because of the large amount of iron dead-material and low tracking granularity, INGRID modules are unable to reconstruct much more than a primary μ^-, though this is sufficient for its task of profiling the beam. After the construction of INGRID, additional components were assembled in to a scintillator-only module which is referred to as the "proton module" - so named because its totally active design allows it, for example, to also reconstruct a proton from a CC QE interaction. This module was placed centrally and between the vertical and horizontal arms (inline with the off-axis modules).

During T2K Runs 1 and 2 INGRID consistently recorded a mean event rate of $1.5 \,/\, 10^{14}$ POT, agreeing with the predicted rate from simulation within uncertainty: data / simulation $= 1.06 \pm 0.04$. Fitting the number of events in each module as a function of off-axis angle allowed it to measured the direction of the T2K beam to an accuracy of around 0.4 mrad, well below the target resolution of 1.0 mrad (Figure 5.12).

5.4. ND280

ND280 is the experiment's off-axis near-detector, located in the near-detector facility 280m downstream of the target, and slightly downstream of INGRID.

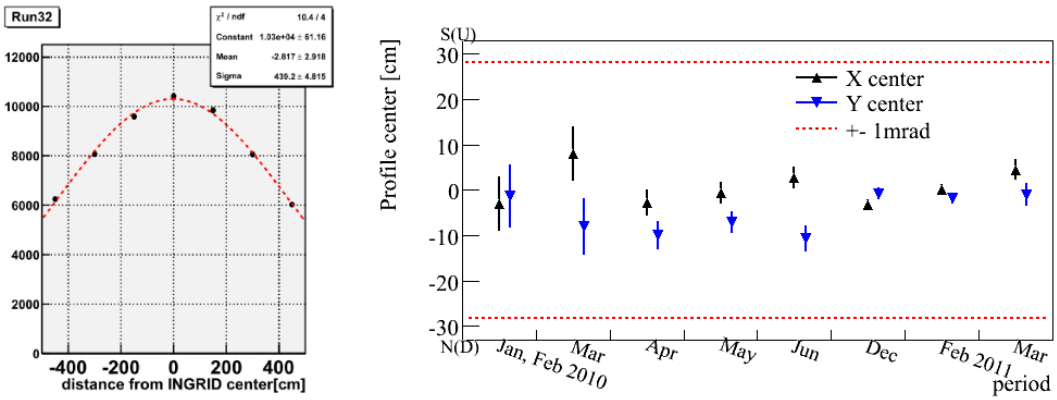

Figure 5.12: (left) An example INGRID beam profile measurement showing number of events in Beam Run 32 as a function of horizontal distance from the centre. (right) The beam direction is measured and stable well within the experiment's target of ± 1.0 mrad. [66]

As discussed earlier, the primary requirements of the detector are:

- Measurement of NC π^0 production on water
- Studies of inclusive and exclusive CC ν_μ interactions, on nuclear targets and specifically on water
- A measurement of the ν_e contamination of the initial beam

The first goal requires a target of water on which neutrinos can interact to produce π^0s. Almost immediately after creation these pions will decay via $\pi^0 \rightarrow \gamma\gamma$ requiring the presence of high density material to encourage the photons to shower if they are to be detected.

Meanwhile, the study of CC ν_μ interactions requires precise measurements of the primary lepton's angle and momentum, in addition to the ability to observe secondary particles emerging from the nucleus. The former drives the design towards lower-densities and the latter requires an active target.

In an ideal world a neutrino detector should have a single target region but, unfortunately for ND280, the dual requirements of efficiently converting photons while maintaining good position resolution cannot be simultaneously satisfied. The same is true for the requirements of having a water target, and an active target. As a result the detector is a compromise of multiple sub-systems.

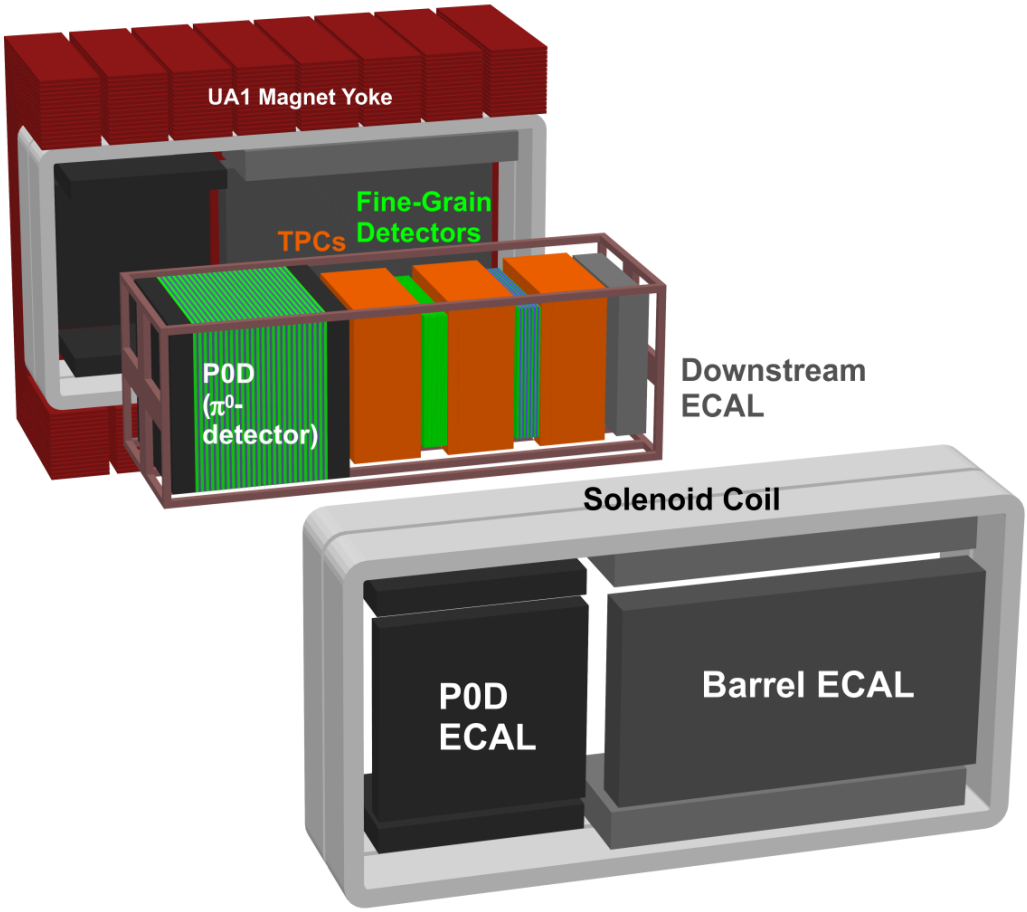

Figure 5.13: An exploded view of the ND280. The central 'basket' region contains the P0D, TPCs, FGDs and Ds ECal. They are surrounded by the Barrel ECal and P0D ECal, and the whole detector is enclosed by the UA1 magnet. [63]

Another significant influence on the design of ND280 is the need for a magnet. Due to their penetrating nature, the momentum of muons cannot practically be measured calorimetrically in such a confined space but must instead be done via curvature in a magnetic field. Such a field also brings the added capability to distinguish μ^- from μ^+ - valuable when $\bar{\nu}_\mu$ make up ~6% of the total flux and the majority of cosmic-ray muons are μ^+.

The design conceived to meet all these requirements (Figure 5.13) placed the primary detectors in a central region, known as the "basket", and surrounded them on all but the upstream-side with electro-magnetic calorimeters. Upstream-most in the basket is the Pi-Zero Detector (P0D) which combines water, metal foils and plastic scintillator to provide the target, photon conversion and reconstruction required for the study of NC π^0s. Downstream of the P0D is the "tracker", in which three Time Projection Chambers (TPCs) sandwich two plastic scintillator detectors referred to as Fine Grained

Detectors (FGDs). The FGDs act as the target for ND280's interaction studies - offering sufficient mass for a reasonable interaction rate in addition to an active target to access some of the activity near an interaction vertex. The argon-gas TPCs give excellent tracking, for direction and momentum reconstruction, and particle identification from *dE/dx*. They serve both the FGDs and the P0D, tracking any forward-escaping particles.

The surrounding electromagnetic calorimeters (ECals) consist of two types with very different remits. The more substantial Tracker ECals provide particle identification and energy measurements for final-state particles leaving the tracker. The much more limited P0D ECals which surround the P0D are there only to catch muons and photons escaping at high angles, and to veto incoming backgrounds.

All these systems are enclosed within a magnet which generates a 0.2 T magnetic field and houses the Side Muon Ranging Detector (SMRD) - planes of scintillator between the plates of the iron yoke - that acts primarily as a cosmic trigger. However encasing the detector within the former UA1 and NOMAD magnet which was available substantially restricts the available space to a box approximately 7 m long $\times$ 3.6 m wide $\times$ 3.5 m high.

5.4.1. The Pi-Zero Detector

The P0D [67] is the upstream-most detector in the ND280 basket with a central water target region sandwiched by two ECal regions (Figure 5.14). The water targets alternate with plastic scintillator modules and brass foils to encourage the photons to convert. The ECal regions meanwhile alternate lead sheets between the plastic scintillator modules to maximise photon conversion and containment. As a final feature, the water targets of the P0D can be filled and drained during running to aid in separating the water contribution to interactions in the fiducial volume. In its most recent technical note [68] the P0D reported a π^0 reconstruction efficiency of 3.6 % (though updated analyses are reporting improvements upon this).

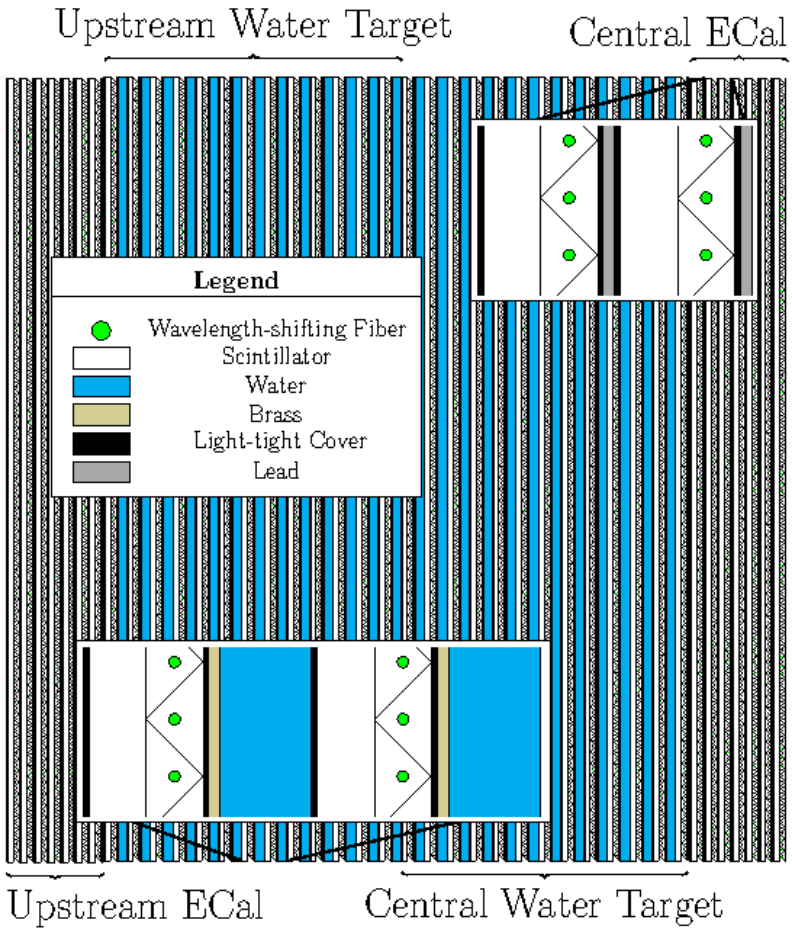

Figure 5.14: A schematic diagram showing a side-on view of the P0D's design. [63]

5.4.2. The Fine Grained Detectors

The two Fine Grained Detectors (FGDs) [69] are the most important target masses for studies of neutrino-nucleus interactions. The upstream FGD, referred to as FGD 1 consists only of plastic scintillator modules, while the downstream FGD, FGD 2, includes six 25 mm thick water targets in addition to plastic scintillator bars.

The FGD plastic scintillator bars are sufficiently dense to provide a good interaction rate (~1.6 / 10^{16} POT), but the bars' 9.61 mm square cross-section also give reasonably good position resolution. This allows FGD 1 in particular to give good vertex position resolution and to reconstruct final-state particles in addition to the primary lepton. For particles which are contained, particle identification is also possible by comparing the range and energy deposited. While predominantly composed of carbon-12 the scintillator, coatings, fibres and glue in FGD 1's active region also bring along small fractions of oxygen,

hydrogen, titanium, silicon and nitrogen, which collectively average to give an $A^{effective} = 12.10$ [70].

FGD 1 has 30 plastic scintillator layers, each with 192 $\times$ 1864.3 mm long bars, alternating between horizontal and vertical orientations. There are 14 identical layers in FGD 2, two of which lie either side of each water target. Because of its water targets FGD 2 does not have quite the same vertex resolution, but it does provide a comparable environment to FGD 1. This will enable studies of neutrino-carbon interactions from FGD 1 to be compared with neutrino-water interactions in FGD 2 for a better understanding of interactions in Super-Kamiokande.

5.4.3. The Time Projection Chambers

The three Time Projection Chambers (TPCs) [71] are placed immediately downstream of each of the three target sub-detectors (P0D, FGD 1 and FGD 2) to provide tracking of the particles which emerge. For all but the highest-angle tracks they achieve position resolutions < 1.0 mm, allowing them to accurately determine the charge and momentum of particles from their curvature in the magnetic field (with transverse momentum resolution $\sigma_p/p^2 \sim 0.1\,\%$).

They also provide particle identification by vertically segmenting tracks, and calculating the mean rate of energy loss (dE/dx) from the path-length corrected energy deposited in each segment (after truncating off the highest 30 %). This is then compared with the expected value from simulation to identify the particle (Figure 5.15). The resolution on the mean dE/dx is better than 8 % for MIPs, making the TPCs the ND280's primary particle identification tool [71].

The TPCs are all constructed identically (Figure 5.16). A central cathode separates two drift chambers containing an argon-based gas, and readout electronics are placed on the lateral sides. Each drift chamber has twelve 342 mm $\times$ 359 mm "micromegas" readout tiles, each of which provides a grid of 48 $\times$ 36 pads.

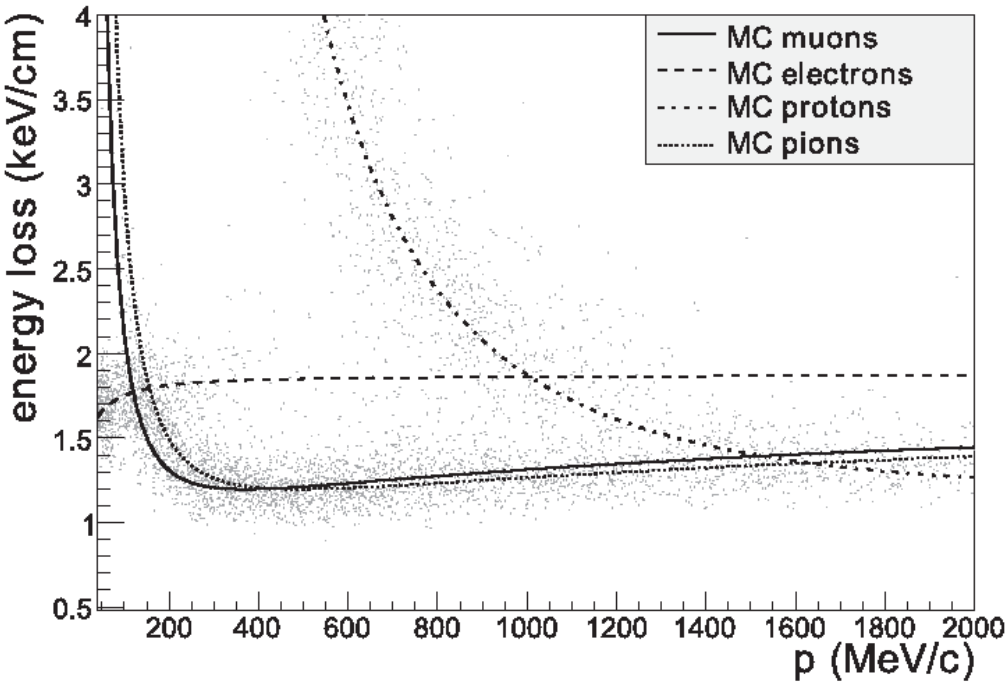

Figure 5.15: The truncated mean dE/dx for particles in T2K Run 1 data, with the fitted curves for simulated muons, protons, pions and electrons overlaid. [63]

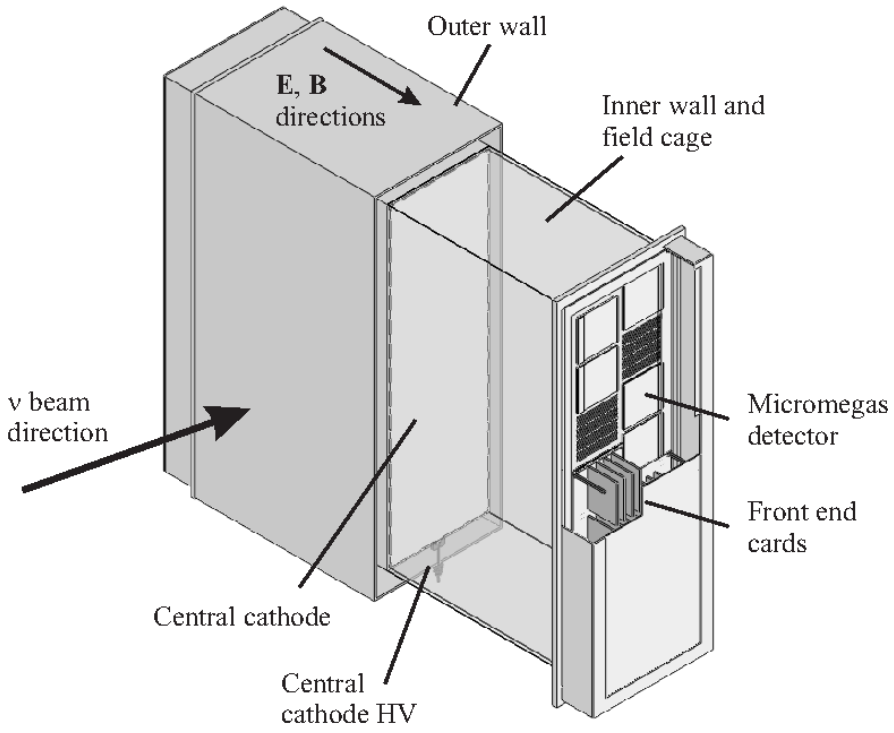

Figure 5.16: Diagram showing the design of a TPC. [63]

5.4.4. The Electromagnetic Calorimeters

The ND280 ECals are really two different sub-systems: the Tracker ECal, comprising the Downstream ECal (Ds ECal) and Barrel ECals, surrounds the tracker (FGDs and TPCs), while the P0D ECal surrounds the P0D.

The Tracker ECal was designed to convert photons generated in the FGDs, provide particle identification (particularly for muon-pion separation), make energy measurements of showering particles, and track anything escaping the FGDs at high-angle. Because this requires a full reconstruction, the Tracker ECal modules have many thin lead sheets separated by layers of plastic scintillator bars which alternate between two views perpendicular to the tracker.

The P0D ECal is significantly less sophisticated since the P0D is capable of converting most of the photons generated within it, and has the tracker downstream for more penetrating particles. Instead the P0D ECal serves only to catch muons and photons escaping the P0D at very high-angles, and to veto incoming activity. These tasks can be performed by just 6 layers of uni-directional plastic scintillator, separated by much thicker lead sheets.

One thing in common between the Barrel ECal and P0D ECal is the need for 6 modules to cover the 4 sides of the basket. Each of the lateral sides can be covered by one module, but the top and bottom sides require 2 modules each to allow the magnet to open.

Module(s)	Layer	Bars per layer	Bar length (m)	Readout ends	Lead Thickness (mm)
Ds ECal	17 Horizontal	50	2.04	2	1.75
	17 Vertical	50	2.04	2	
Barrel ECal Top/ Bottom	16 Perpendicular	96	1.52	1	
	15 Parallel	38	3.84	2	
Barrel ECal Side	16 Perpendicular	96	2.36	1	
	15 Parallel	57	3.84	2	
P0D ECal Top/ Bottom	6 Parallel	38	2.34	1	4.0
P0D ECal Side	6 Parallel	96	2.34	1	

Table 5.3: Specifications of the ECal modules. Layer names relate to the direction along which the longest dimension of the bars lie with respect to to the beam or the world.

The construction of the 6 P0D ECal modules was a year-long project which took place at the University of Warwick. The first (left-side) module was built over the final months of 2009, and represented a whole-group effort to understand the construction process. Between January and July 2010 I led the day-to-day construction of the remaining five modules.

The first step of building a module was to construct the primary aluminium bulkheads around a carbon fibre base. Into this would be inserted a layer: an aluminium frame holding a 4 mm thick sheet of lead, under which were glued the plastic scintillator bars. Once inside the module the optical fibres would be inserted.

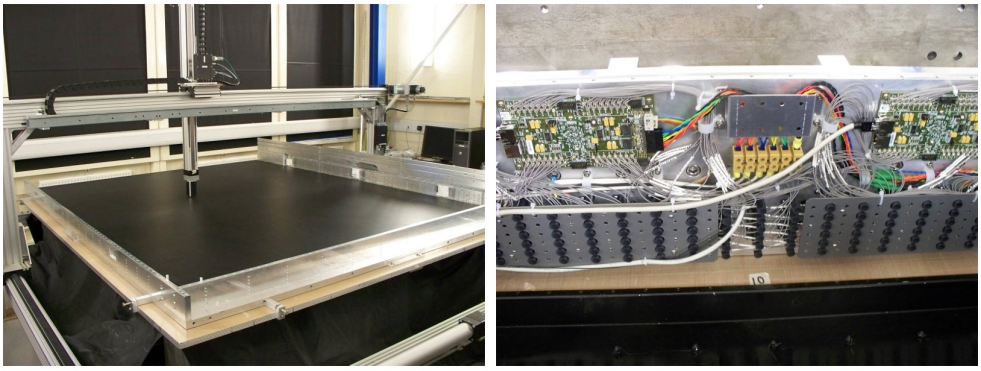

Figure 5.17: (left) The 2-dimensional scanner moving a Cs source across the first layer of the Left Side module. (right) A section of the readout bulkhead on the Bottom Right module. The large electronics boards are TFBs, the coloured cables provide power, and the black cases at the bottom house the MPPCs.

After the installation of each layer, it would be temporarily instrumented with photo-sensors (MPPCs), and a 2-dimensional scanner would position a Cs source at multiple points above each bar. A visual scan of the resulting response profile along each bar was used to check for cracks in the bars or breaks in the optical fibre.

Once all layers had been installed in this way, all the optical fibres were instrumented with their final MPPCs, which were in turn connected to the readout electronics boards (TFBs) that had been mounted onto the bulkhead at the readout end. Each of these boards were wired up to the external power supply, and shielded ethernet cables for communication with the readout management modules in ND280. Temperature sensors, water cooling pipes and dry air pipes also had to be installed. Final checks before shipping included initialising all the TFBs, and taking dark-noise readings from all MPPCs.

All six modules were installed in September 2010 and started taking beam data from T2K Run 2.

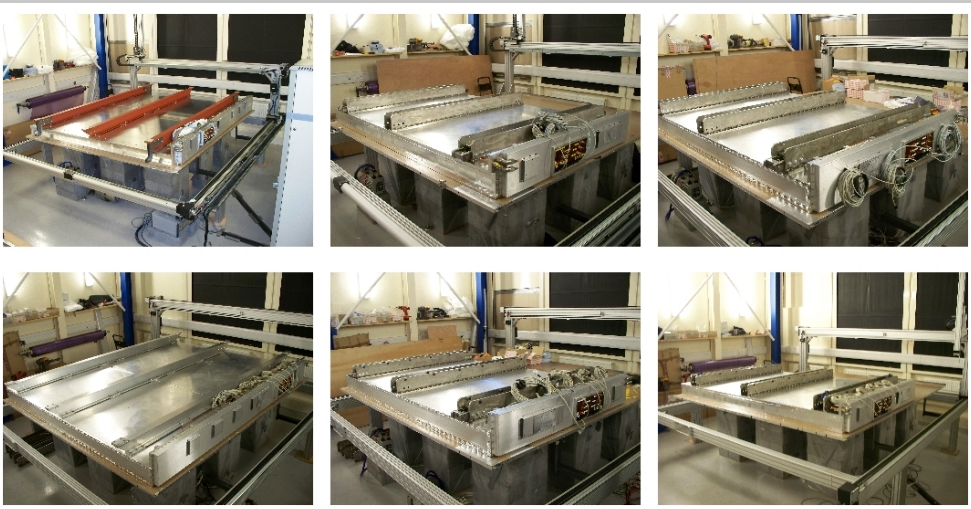

Figure 5.18: The six P0D ECal modules built at the University of Warwick. Clockwise from top-left: Left Side, Left Top, Left Bottom, Right Bottom, Right Top, Right Side.

The construction project was completed ahead of schedule and within budget, and represented the first major hardware contribution to be made by Warwick's particle physics group to an experiment.

5.4.5. The Magnet & SMRD

A muon's energy cannot practically be measured calorimetrically in such a confined space, since they are so highly penetrating, so this must be done from curvature in a magnetic field. A magnetic field also gives ND280 the ability to measure the charge of a particle track - a valuable capability for distinguishing μ^- from μ^+ and π^+ from π^-. For this reason T2K acquired a 0.2 T magnet from CERN which had previously been used in the NOMAD and UA1 experiments.

The magnet's coil runs vertically and parallel to the beam to generate a magnetic field which, from the view of an observer standing upstream of the detector, would point horizontally to the right. This results in negatively charged particles which are initially travelling downstream being bent downwards. The coil is surrounded by a yoke assembled from plates of iron.

Finally, some of the gaps between the iron plates are instrumented by plastic scintillator planes, with optical fibres running through them. These planes form the Side Muon Ranging Detector (SMRD). In concert with the P0D and Ds ECal, the SMRD primarily acts as the detector's cosmic trigger and veto, though its hits from escaping muons can also be associated with a reconstructed track from the inner detectors.

5.5. Common Components

The P0D, FGDs, ECals, SMRD and INGRID all contain plastic scintillator as their active components. The extruded plastic scintillator was produced at Fermilab and is composed of polystyrene doped with wavelength shifting scintillators PPO (1 %) and POPOP (0.03 %) which results in blue light emission (420 nm). The plastic was co-extruded with a 0.25 mm thick reflective layer of TiO_2 to keep scintillation light in and external light out.

This scintillation light is then collected and transported by 1 mm diameter optical fibres which are strung down 3 mm diameter extruded holes in the centre of the bars (or laid in a groove in the SMRD planes). These fibres, manufactured by Kuraray, are also wavelength shifting and convert the blue

light spectrum to a green (476 nm) that is well matched to the light sensors attached to the ends.

These light sensors are Multi-Pixel Photon Counters (MPPC) [72] manufactured by Hamamatsu which, unlike photomultiplier tubes, can still be operated in a magnetic field. They consist of 667 pixels arranged accross a 1.3 mm × 1.3 mm active area, and boast a photon detection efficiency of ~20 % for the light received from the optical fibres.

5.6. Simulations

As with all complex experiments it is necessary for T2K to run simulations in order to understand how the measurements recorded by its detectors correspond to the physics which occurred.

The J-PARC neutrino beam is simulated for the purpose of providing flux predictions [64] to the near and far detectors using software collectively known as "JNUBEAM". The simulated beamline geometry includes the target, horns, decay volume and beam monitors. 30 GeV protons are directed onto the graphite target, and the resulting particles are tracked until they decay to neutrinos or stop. The simulation of primary interactions inside the target are based on data from the NA61/SHINE [73] experiment, secondary interactions are simulated with FLUKA [74], and interactions outside the target use GEANT3/GCALOR [75].

The simulation of the near detector geometries is done in GEANT4 [76] as is the passage of final-state particles emerging from neutrino-nucleus interactions. The neutrino interactions themselves can be simulated with either the GENIE or NEUT generators (see Chapter 3), which propagate neutrinos from the beam flux simulation through the geometry exported from the GEANT4 simulation. After the particles have been propagated through the near detectors a custom software package, called "ELECSIM", simulates the response of the detector and its electronics to the energy deposited. In the scintillator sub-detectors this includes simulating the light emitted in response to energy deposition, the light's transport through the bar and down the optical fibres, the response of the MPPCs to that light and the electronics chain thereafter. For the TPCs ELECSIM simulates the electron

drift, response of the micromegas and, again, the electronics chain which follows.

Super-Kamiokande's "SKDETSIM" is a fortran-based software package which is responsible for the geometry and final-state particle simulations. Again, the neutrino interactions can be generated with GENIE or NEUT using the neutrino flux from the beam simulation.

5.7. ND280 Software & Reconstruction

The first processing stage in the ND280 software chain is calibration, and is the last stage at which simulation and data are treated differently. For data the goal is to correct for the various effects introduced by the scintillator bars, optical fibres and readout electronics. For simulation the goal is to replicate the output from this process. In both cases the result is a collection of calibrated "hits" with a position, time and information on the energy deposited (often referred to as "charge").

The ND280 reconstruction software is essentially a two-stage process as a result of the very different time/space/charge information provided by the different sub-detector systems, which makes a unified reconstruction algorithm unsuitable. Instead, each sub-detector has its own dedicated reconstruction algorithm which groups associated hits together, fits the resulting objects, and calculates properties for use by analysers (such as the TPC particle identification, or FGD vertex activity). The last of these to be run is the TPC reconstruction, which needs to find matching objects in neighbouring detectors in order to determine the time at which the track was created.

The results from the individual sub-detector reconstructions are then passed to a "global" reconstruction, which matches objects with compatible start/end points and directions between detectors. These combined objects are re-fitted using a Kalman filter from the Recpack [77] toolkit, utilising geometric and magnetic field models, to create final "reconstructed objects" with position, direction and momentum measurements..

6. A Search for Coherent Pion Production at T2K

In Chapter 4 it was discussed how searches for CC coherent pion production at $E_\nu < 2\,\text{GeV}$ have found no evidence for its existence. This is in conflict with the predictions of the established model and additional experimental data is required to resolve the situation. The T2K experiment described in Chapter 5 provides an excellent environment in which to study neutrino interactions at a mean ν_μ energy of 0.856 GeV, using its near detector ND280. The opportunity was therefore taken to conduct a ν_μ CC coherent pion production analysis of the ND280 data.

Since there is no experimental evidence that the interaction even exists at these energies, it was decided that the analysis should be conducted as a search, rather than a measurement. The approach was to make a selection of events which should contain any coherent pion interactions which occur, and the events selected in data can then be compared with the non-coherent background predicted by simulation. Any significant excess of events over the background prediction would then indicate that coherent pion production is occurring at an observable rate.

It is always good practice when making physics selections, wherever possible, to focus on the characteristic properties of the sample you wish to select rather than features of the model used to simulate it. This becomes essential when the signal model is considered unreliable, such as in this case where the existing data and model are in conflict. The defining characteristics of ν_μ CC coherent pion production are:

- Production of exactly one μ^- accompanied by one π^+
- No fragmentation of the target nucleus
- Low transfer of momentum to the target nucleus, resulting in:
  - Little nuclear recoil
  - Angles of μ^- and π^+ with respect to the incoming neutrino are peaked in the forward direction

It is events which match this description, that the analysis must select. This will also improve the reproducibility of the selection by those outside of T2K. If the results of the analysis are to benefit the understanding of coherent pion production, other experiments must be able to perform comparable selections, and theorists must be able to compare them to their predictions.

6.1. Overview

The FGD 1 sub-detector was chosen as the interaction target. It is dense enough to offer a sufficiently high interaction rate, but not so dense as to prevent the majority of π^+ from escaping into TPC 2 downstream. It also provides an active volume for better resolving additional activity at the interaction vertex to reject backgrounds. Approximately 0.8 % of the CC ν_μ interactions in the FGD 1 fiducial volume are predicted to be coherent pion production (using the default Rein-Sehgal model in GENIE).

The first step is the selection of CC ν_μ interactions, by finding events with a μ^- originating from FGD 1. To do this the analysis follows the ND280 ν_μ Inclusive selection [78] [79], an approved selection used extensively within T2K [80] (Section 6.3). Basing the analysis on this selection gives it a well validated foundation, and improves compatibility with other studies, such as those relating to systematic uncertainties.

The second step is the selection of those CC ν_μ interactions which also contain a single π^+, for which a custom selection was developed (Section 6.4). Finally two cuts are made on the net transverse momentum (Section 6.6) and vertex activity (Section 6.7) in order to reject backgrounds and focus on a more coherent-like sample.

The search for evidence of CC coherent pion production is then performed by looking for an excess over background in the $|t|$ distribution of selected events which, as discussed in Chapter 4, is the characteristic distribution where coherent signals are found.

T2K Run	POT Analysed (10^{20})
1a	0.29
2a	0.13
2b	0.65
3b	0.21
3c	1.35
Total	2.64

Table 6.1: The quantity of data analysed in each T2K Run, measured in the number of protons delivered onto the T2K beam target in spills which met the "good spills" requirements (see Section 6.3).

6.2. Implementation Details

The analysis was implemented in dAnalysis: a self-authored framework, designed for ND280 analyses and written in python. Its interface design focused on simplicity for the user, creating an accessible framework which has been easily utilised by multiple undergraduate project students, and allows rapid prototyping of initial studies. However it also supports more complex requirements and is highly flexible, and is therefore also capable of full analyses, such as this one. The primary drawback of the framework is performance due to being written in a very high-level language. This makes the processing of large numbers of files time consuming. Fortunately, this was only a relevant concern for the initial "skimming" of the full simulated data-set down to a manageable size - a task performed only twice in the development of the analysis.

The data and simulation used come from the official ND280 processing referred to as "production 5", which at the time of writing is that currently recommended by the ND280 Computing group. The data in this production suitable for analysis is from T2K Runs 1a, 2b, 2c, 3b, and 3c, and was processed through ND280 software version 10.11.21. The quantity of data from each of these runs is measured in terms of protons-on-target (POT), the quantity of protons delivered by the T2K beam onto the target, and is shown in Table 6.1.

The simulation was produced using the neutrino flux prediction from JNUBEAM version 11a (which provided three separate fluxes based on the conditions during T2K Runs 1, 2, and 3), interactions from GENIE version 2.6.6, and ND280 software version 10.11.17. The interactions in this simulation then had three corrections applied:

- **Flux correction**
  The neutrino flux was updated to JNUBEAM version 11b, which was tuned based on the beam conditions recorded during data running. This is done by taking four histograms of neutrino energy, one for each neutrino flavour, calculating the ratio between the JNUBEAM 11a and 11b predictions for each bin, and weighting every simulated interaction according to the applicable ratio. For ν_μ interactions these weights range in value from 0.87 to 1.43.

- **GENIE coherent pion correction**
  For ν_μ CC coherent pion interactions in FGD 1 a correction is applied to compensate for a bug in the Rein-Sehgal coherent pion production model implemented in versions of GENIE $\leq$ 2.8.0 (there was a bug in the interpolation of the pion-nucleon scattering cross-sections, see Figure 6.1). Samples of ν_μ CC coherent pion interactions were generated on ^{12}C at 100 MeV increments in neutrino energy between 400 and 2000 MeV - both with and without the bug included - each containing 10^6 events. For each of these samples, a 2D histogram of pion momentum verses angle was made, and the ratio between fixed and unfixed versions is taken to give a weight by which the interactions from simulation are corrected. Typical weights are found within $\pm 30\,\%$.

- **Momentum resolution correction**
  The last correction applied to the simulation compensates for the observation that the reconstructed momentum resolutions in data and simulation do not match. Defining p_B as the momentum perpendicular to the magnetic field, the resolution on $1/p_B$ was found to be $32 \pm 10\,\%$ wider in data [81]. Following the prescription in [81], this is accounted for by taking the initial reconstructed $1/p_B$ of selected tracks in simulation and pushing them 32 % further away from their true value such that:

$$\frac{1}{p_B^{\text{corrected}}} = \frac{1}{p_B^{\text{true}}} + 1.32\left(\frac{1}{p_B^{\text{initial}}} - \frac{1}{p_B^{\text{true}}}\right) \tag{6.1}$$

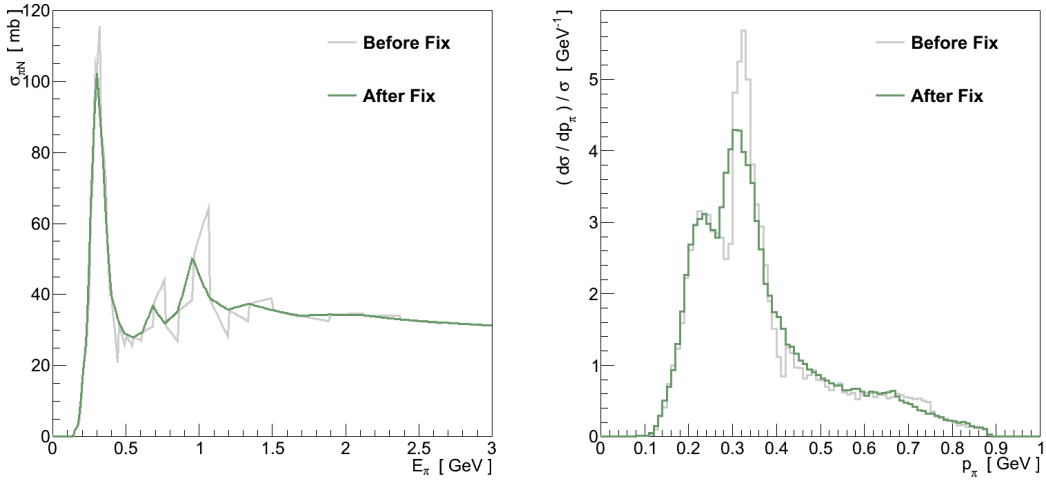

Figure 6.1: Cause and effect of the bug in GENIE's Rein-Sehgal coherent pion production model. (left) The total pion-nucleon scattering cross-section. The inelastic cross-section contains an identical bug. (right) The effect on the pion momentum spectrum for ν_μ CC coherent pion production on ^{12}C at $E_\nu = 1.0$ GeV.

The reconstructed momentum of the track is then re-calculated from the corrected value of $1/p_B$. The uncertainty on the resolution difference will appear as a systematic uncertainty in Section 6.10.3.1.

The analysis is also applied to the predictions from two other simulations. Although its coherent pion production model is more dated than that in GENIE, analysing T2K's other interaction simulation, NEUT, provides both an alternative set of background models and a useful reference for those T2K analysers who use NEUT as their primary simulation. NEUT was also the simulation used in the K2K and SciBooNE analyses. The files from production 5 were made with NEUT version 5.1.4.2, to which the same flux and momentum resolution corrections are applied as for Genie.

Additionally the Alvarez-Ruso coherent pion production model which was implemented in GENIE (Section 4.3) allows an assessment of how the signal selection efficiency might by impacted in an alternative model. A sample of 5654 Alvarez-Ruso ν_μ CC coherent pion events was generated in the FGD 1 fiducial volume and processed through the ND280 software used for production 5. This was merged with the standard production 5 GENIE sample with all Rein-Sehgal coherent events stripped out. The Alvarez-Ruso events were weighted such that the ratio of total Alvarez-Ruso events to total Rein-Sehgal events, was the same as the ratio of their flux-averaged cross-sections, i.e.:

$$\frac{\left\langle \sigma_{\text{Alvarez-Ruso}} \right\rangle}{\left\langle \sigma_{\text{Rein-Sehgal}} \right\rangle} = \frac{N_{\text{Alvarez-Ruso}}}{N_{\text{Rein-Sehgal}}} \tag{6.2}$$

This ensures that the number of events from the Alvarez-Ruso model is normalised appropriately for the analysis, based on the ND280 flux and the model's cross-section.

In this chapter, unless otherwise specified:

- The "signal" is ν_μ-induced CC coherent pion production inside the fiducial volume defined in Section 6.3
- Data is from T2K Runs 1a, 2b, 2c, 3b and 3c combined
- Simulation is from T2K Runs 1a, 2b, 2c, 3b and 3c combined, scaled run-by-run to match the POT recorded in data, produced with GENIE and with the corrections detailed above applied
- Plots show both data and simulation as histograms, simulation represented by solid boxes, and data by crosses (the horizontal width indicating the extent of the bin, and the vertical height a Gaussian statistical uncertainty)
- The abbreviation OOFV refers to interactions which occurred outside of the fiducial volume

6.3. The ν_μ Inclusive Selection

The ν_μ Inclusive selection was developed within the ND280 ν_μ analysis group and was re-implemented for this analysis based on its description in two internal technical notes [78] [79]. However the selection was originally developed for production 4, and the benefits from reconstruction and calibration improvements in production 5 have resulted in a few notable differences between this implementation and the original:

- The momentum for tracks is taken from the global ND280 reconstruction instead of the TPC reconstruction.

- The *dE/dx* values provided by the TPC reconstruction no longer require correcting.
- The fiducial volume is modified from that in the original (see below).

The ν_μ Inclusive selection is made by passing through the following steps:

1. **Require good data quality**
   For each beam spill the T2K Beam Group determine whether or not the spill was of good quality by requiring stable operation of the beam magnets and horns, and the signal in the muon monitors being in the correct direction and within a target intensity. Likewise the ND280 Data Quality group assess whether the ND280 was operating correctly by checking the operation of all five sub-detector systems and the magnet. For data from a spill to be included in the analysis, both of these groups must have approved it for use.

2. **Separate trigger into bunches**
   The ND280 detector is triggered once per beam spill so the tracks must be separated out into the bunches they belong to (Figure 6.2). A track is deemed to belong to a bunch if its start time lies within 60 ns of the mean bunch time (in data bunches are approximately 15 ns wide separated by around 550 ns). From here on, the term "event" will be taken to mean the contents of a single bunch.

3. **Select a candidate muon track**.
   The signature feature of a ν_μ CC interaction is the presence of a muon - a negatively charged particle which will likely be highly penetrating and leave a long, clean track. So the first selection requirement is to search the event for reconstructed tracks which:

   - **Are negatively charged**
   - **Include a "good" component in TPC 2**
     A "good" TPC component is one formed of hits on 18 or more of the micromegas' readout columns. Because the TPC reconstruction is based on first clustering hits vertically, this ensures that the track is of sufficiently high quality that the charge and PID information are reliable.

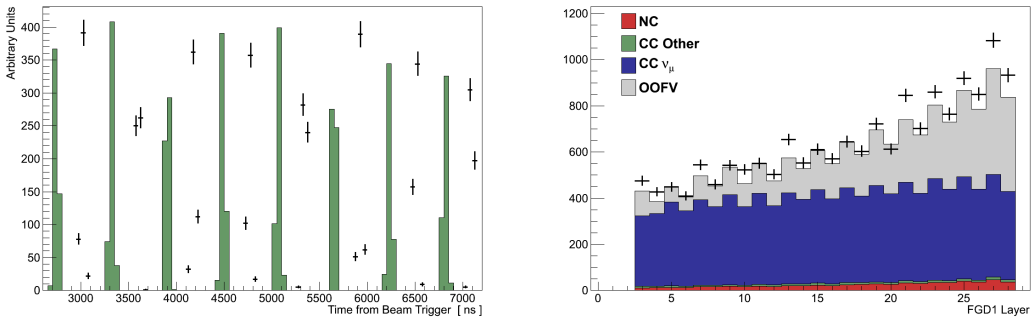

Figure 6.2: (Left) The time relative to the beam trigger of selected muon candidates. The bunches in each T2K run and simulation occur at different times, so for the sake of clarity only data from T2K Run 2b is shown. (Right) The FGD 1 layer in which the starting position of selected muon candidates is found. The simulation is broken down by the true interaction.

- **Start within the FGD 1 fiducial volume**
  The original ν_μ Inclusive selection defined the fiducial volume to exclude the first two upstream layers, and the outer-most five bars at either end of each subsequent layer (Figure 6.2). In this analysis the fiducial volume was modified to also exclude the final two downstream layers, which was necessary to ensure the vertex activity could be measured consistently (Section 6.7).

If no reconstructed tracks are found to meet these requirements the event is rejected. If one or more tracks is found the one with the highest momentum is chosen. This reconstructed track is referred to as the "muon candidate".

4. **Veto backwards-going tracks**
   If the end position of the muon candidate is upstream of its start position then the event is rejected. This cut was added in response to the observation that most negative tracks which were reconstructed as backwards-going were in fact forward-going positive tracks[1]. Due to improvements in the reconstruction this is no longer necessary, however the cut has been left in the analysis for consistency with the original ν_μ Inclusive selection. It removes only 0.2 % of tracks which, in any case, are likely to be mis-reconstructed (Figure 6.3).

1. The reconstruction determines the direction of a track based on which alternative provides a better fit for the Kalman filter it uses.

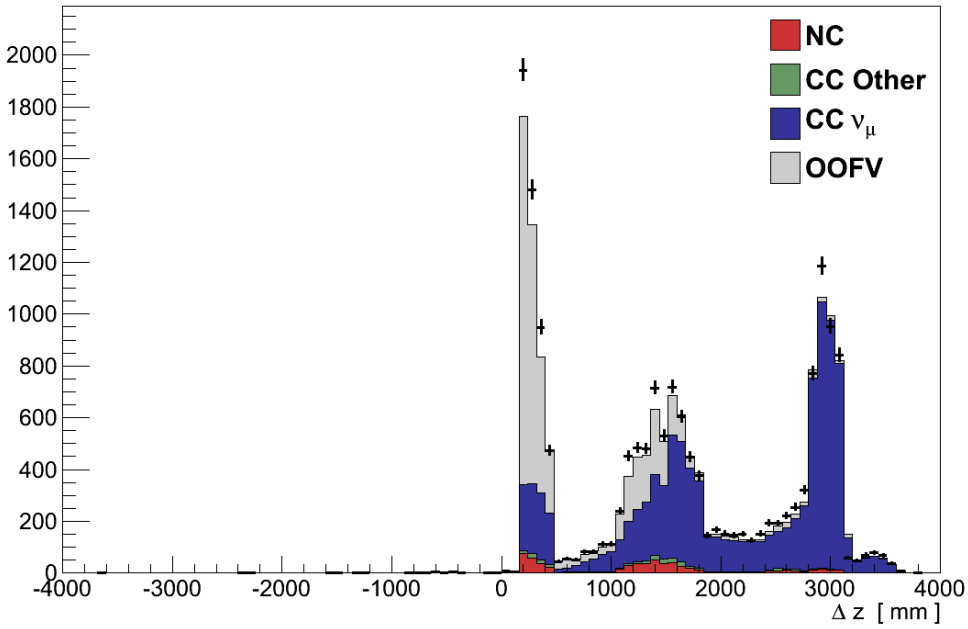

Figure 6.3: The difference in z-position of the front and back of the muon candidate track. The first peak contains low-momentum tracks curving quickly out of TPC 2, the central peak comes from tracks stopping in FGD 2, and the last peak stopping in the Ds ECal. Events with $\Delta z < 0.0$ are rejected.

5. **Veto tracks coming from upstream**
   This cut attempts to remove events which originated further upstream than FGD 1 but resulted in a separate reconstructed track emerging from FGD 1. To do this, all the other tracks in the event (same beam-bunch as the muon candidate) that have a good TPC component are selected. Then the highest momentum track in this selection is chosen. If the start position of that track is >150 mm upstream of the muon candidate's start position, then the event is rejected (Figure 6.4).

6. **Require muon candidate track to be muon-like**
   As discussed in Section 5.4.3, the TPCs provide discriminating variables for particle identification (PID). First, the truncated mean of the energy deposited in the TPC is taken to be the measured dE/dx of the track. Pull variables P_i are then formed by comparing this to the dE/dx expected at the track's momentum for four particle hypotheses, i (proton, charged pion, muon and electron). Finally, likelihoods formed from these pulls are combined into discriminating variables X_i for each particle hypothesis:

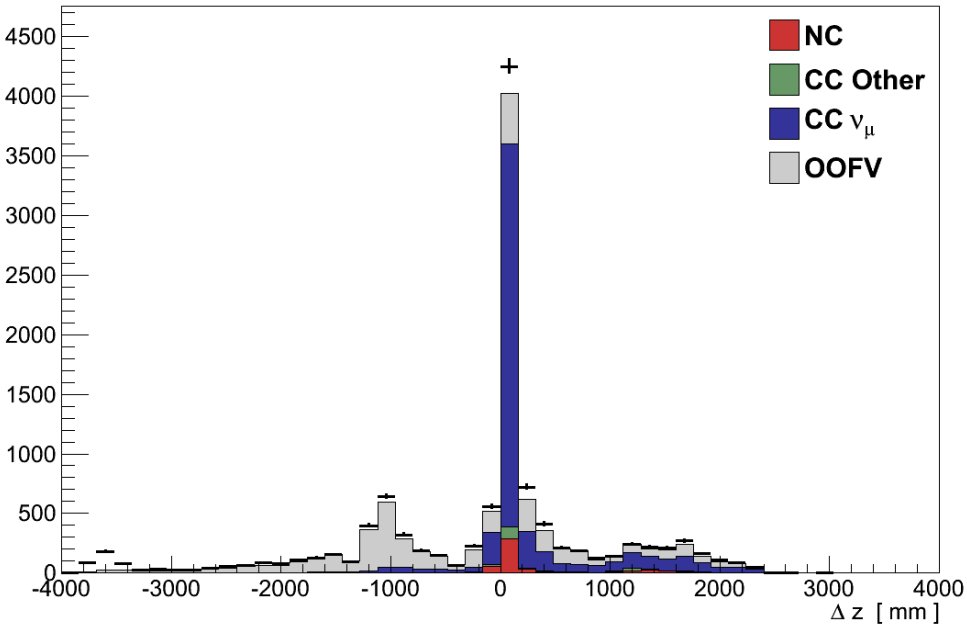

Figure 6.4: The difference in z-position of the front of the muon candidate track and the front of the second track. If $\Delta z <$ -150 mm the event is rejected. The un-simulated bump in data at $\Delta z \approx$ -3600 mm is likely due to muons from interactions upstream of the detector, known as "sand muons", which are not included in the standard simulation.

$$X_i = \frac{e^{-\frac{1}{2}\mathrm{P_i}^2}}{\Sigma_j e^{-\frac{1}{2}\mathrm{P_j}^2}} \tag{6.3}$$

which give values ranging from 0 (indicating that particle hypothesis is worse than the others) to 1 (indicating that particle hypothesis is better than the others). In addition, for tracks with momentum $<$ 500 MeV an additional PID discriminator is calculated:

$$Y_{\mathrm{MIP}} = \frac{X_\mu + X_\pi}{1 - X_p} = \frac{X_\mu + X_\pi}{X_\mu + X_\pi + X_e} \tag{6.4}$$

This is to separate electrons from minimally ionising particles (MIPs, i.e. muons and pions) whose *dE/dx* profiles overlap at low-momenta (see Figure 5.15).

Cuts are then applied using these discriminators calculated for the muon candidate. For events where the candidate has momentum $\geq$ 500 MeV the event is rejected if $X_\mu \leq 0.05$. For events where the candidate has

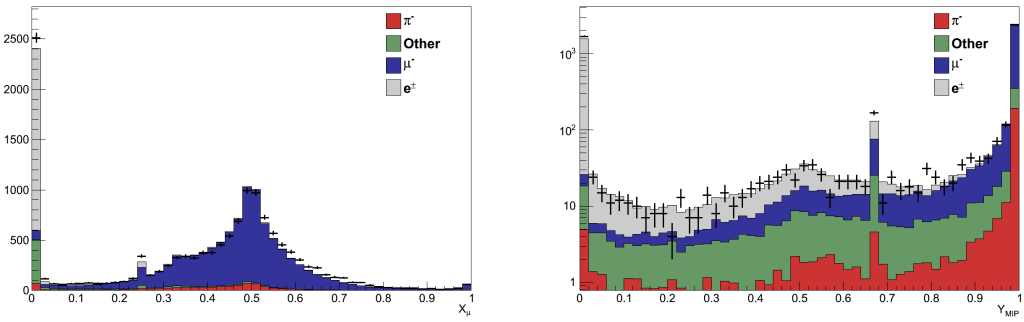

Figure 6.5: (left) Plot of X_μ for all muon candidates. (right) Plot of Y_{MIP} for muon candidates with momentum $< 500\,\text{MeV}$, shown on a log scale because the distribution is dominated by the spikes at 0 and 1.

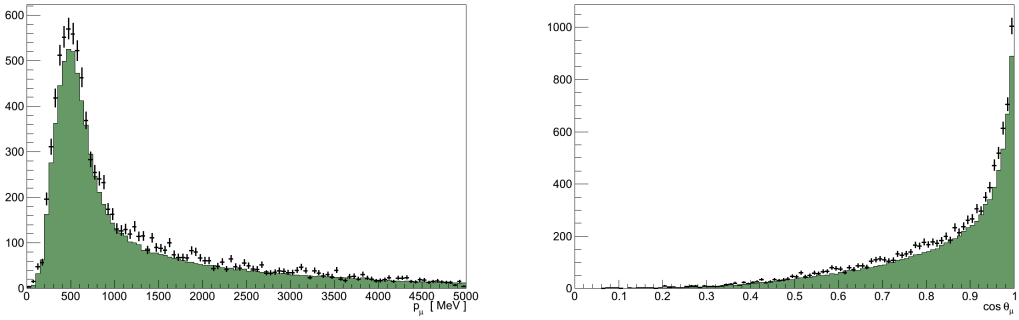

Figure 6.6: Kinematic plots for all muon candidates in the ND280 ν_μ Inclusive Selection. (left) The magnitude of the reconstructed momentum. (right) The reconstructed angle of the track's direction with respect to the detector's z-axis.

momentum $< 500\,\text{MeV}$ the event is rejected if $X_\mu \leq 0.05$ or $Y_{MIP} \leq 0.8$ (Figure 6.5).

The events which pass these requirements are referred to as the ND280 ν_μ Inclusive Selection, and in data it contains 10318 tracks. According to the simulation, in which the selection contains 9005 tracks, this is a 90 % pure sample of muons. Aside from the overall normalisation difference, the momentum and angular distributions are well described by the simulation (Figure 6.6).

6.4. The Coherent Initial Selection

After selecting CC ν_μ events, the selection now needs to be refined to those which match the appearance of coherent pion production. Specifically that

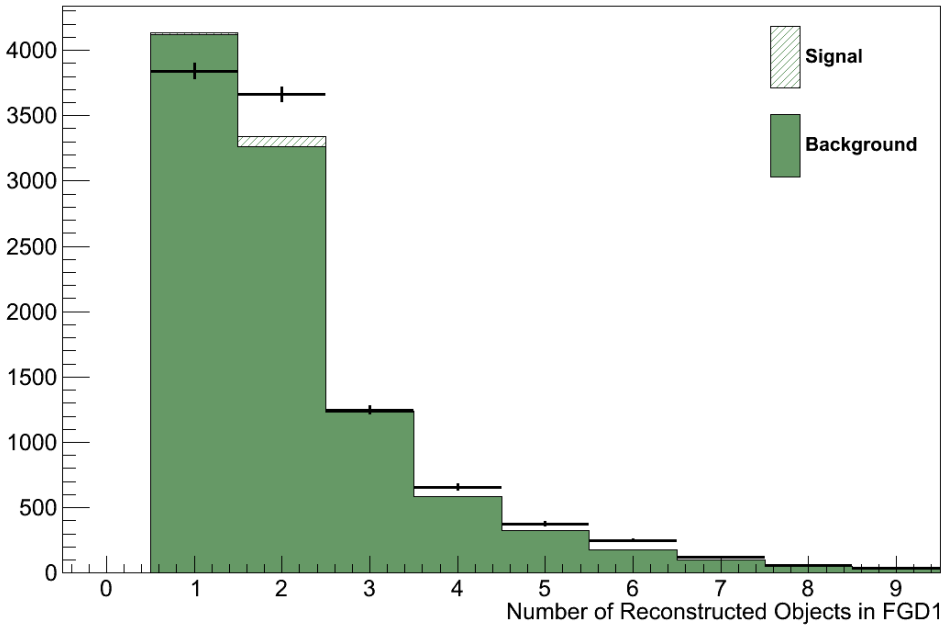

Figure 6.7: The number of reconstructed objects in FGD 1

means a μ^- and π^+ originating within FGD 1, travelling downstream, and unaccompanied by other particles. This is done by applying the following requirements to each event:

1. **Veto excessive tracks in FGD 1**
   True coherent interactions should produce exactly one muon and one pion, so the presence of any additional tracks in the target detector is a strong indicator that this is not a coherent interaction. Therefore, events in which FGD 1 contains more than two reconstructed objects are rejected (Figure 6.7).

2. **Select a candidate pion track**
   In addition to the muon, for which a candidate track has already been selected, coherent interactions should also produce a π^+. So the event is searched for tracks which:

   - **Are positively charged**
   - **Include a "good" component in TPC 2**
     Where "good" is defined the same as for the muon candidate.
   - **Are pion-like**
     The track is rejected if $X_\pi \leq 0.05$

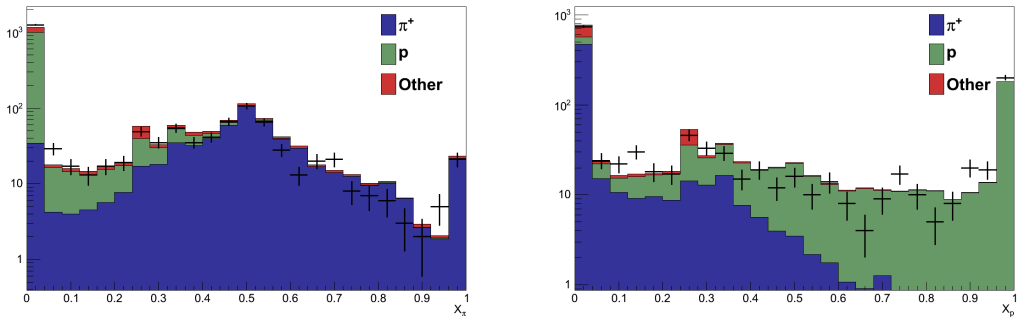

Figure 6.8: (left) Plot of X_π for all potential pion candidates. Candidates with $X_\pi \leq 0.05$ are rejected. (right) Plot of X_p for all potential pion candidates. Candidates with $X_p \geq 0.5$ are rejected. Both are shown on log scales because the distributions are dominated by the spikes at 0.

- **Are not proton-like**
  As can be seen in Figure 6.8, the largest background when selecting secondary positive tracks is protons, so this is mitigated by rejecting tracks where $X_p \geq 0.5$

Note that there is no requirement that the tracks include a component in FGD 1. Because it is a challenging task for the FGD reconstruction to separate two close, parallel tracks (such as a forward-going muon-pion pair), no requirement is placed on the track being reconstructed in FGD 1 or being associated with the muon candidate's vertex.

If no tracks are found which meet these criteria the event is rejected. If more than one track is found the event is also rejected, on the grounds that coherent events should not contain multiple tracks. If exactly one track is found, that track is referred to as the "pion candidate".

The events which pass these requirements form the coherent initial selection, of which there are 620 in data. This compares with the prediction from simulation of 704 events which, for the default Rein-Sehgal coherent model, is expected to include 42 % of the true coherent interactions which took place (Table 6.2).

Of the signal events lost, 38 % were discarded by the ν_μ Inclusive Selection, predominantly as a result of failing to find a good negative track in both FGD 1 and TPC 2. The remaining 62 % lost were discarded by the coherent pion selection. The largest single drop comes in failing to find a good positive track in TPC 2 - a result of pions being absorbed in FGD 1 or escaping out of the sides of the detector. In future productions, as the ND280 reconstruction

Step	Data	Simulation			
		Total	Signal	Efficiency	Purity
ν_μ Inclusive selection	10303	10016	96	78 %	1.0 %
FGD 1 veto	5275	4821	83	67 %	1.7 %
Positive track in TPC 2	627	711	52	43 %	7.3 %
Pion PID	620	704	52	42 %	7.4 %

Table 6.2: Event numbers and performance measures after steps in the coherent initial selection.

	Good Muon	Bad Muon
Good Pion	71%	5%
Bad Pion	19%	5%

Table 6.3: Fraction of simulated events in the initial selection for which the track identified as the muon/pion candidate was (good) or was not (bad) actually caused by a muon/ pion.

Particle	π^+	p	μ^+	e^-	e^+	K^+	Other
Fraction	78 %	14 %	4 %	1 %	1 %	1 %	< 1 %

Table 6.4: The true particles associated with the reconstructed tracks of the pion candidates in simulation, reported as a fraction of the 704 selected.

improves, it may become possible to recover some of the lost efficiency by selecting tracks which are contained within FGD 1, or escape into the surrounding ECals.

Thus far the focus of the selection has been on finding signal events, those containing just a muon and a pion, rather than removing any backgrounds. As can be seen in Table 6.3, the primary cause of failure of that goal is in mis-identification of the candidate pion track. The biggest single contamination (Table 6.4) is of protons which can be seen in Figure 6.9 to be mostly found at $p > 1000\,\text{MeV}$ where the TPC PID is less able to distinguish protons from pions (Figure 5.15). Likewise, contaminations of electrons and positrons can mostly be found at $p < 300\,\text{MeV}$ where again the TPC PID curves overlap.

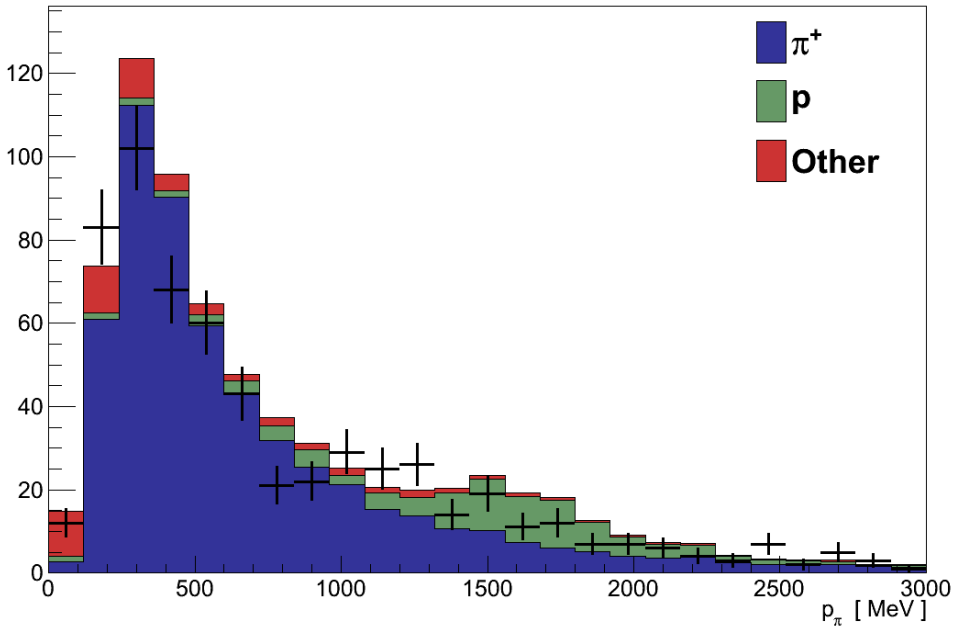

Figure 6.9: Momentum spectrum of pion candidate tracks, with the simulation broken down by the true particle type which caused the track.

With a selection of coherent-like events, the next task is to reduce the background contamination. This is achieved by cutting on variables which highlight characteristic features of coherent pion production, and separate it from background interactions.

Two such cuts are applied. First, a cut on the net transverse momentum of the muon-pion system exploits the kinematic requirements on a predominantly two-body interaction. Second, a cut on the amount of energy deposited near the vertex attempts to exclude events which generated additional particles which were un-reconstructed.

6.5. Neutrino Direction Correction

Before proceeding a small correction is made to the track directions output by the ND280 reconstruction, in both data and simulation, to account for the difference between the detector's co-ordinate system and the direction defined by the incoming neutrino. As can be seen in Figure 6.10, neutrinos in the fiducial volume are peaked at an angle of $\vartheta_\nu \approx 1.7^\circ$ with respect to the detector's z-axis. In the transverse plane they are found with -180 ° <

Final State Particle Topology	Fraction of Events
Muon + Pion	32 %
Muon + Proton + Pion	23 %
Muon + Pion + X	19 %
Muon + Proton	8 %
Muon + X (no pion)	7 %
NC + Pion + X	4 %
OOFV	4 %
Anti-Muon + Pion + X	1 %
Muon + Nothing	1 %
Other	< 1 %

Table 6.5: Final-state topology of simulated interactions in the coherent initial selection. "Pion" refers exclusively to charged pions. X represents any combination of particles, with the exception of charged pions where stated, and such that there is no overlap between categories. Only particles with momentum > 200 MeV are counted.

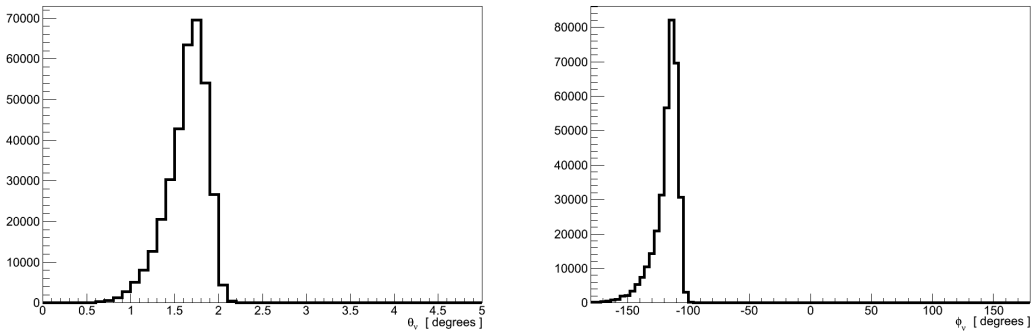

Figure 6.10: Angles in the ND280 co-ordinate system of true ν_μ undergoing CC interactions in the fiducial volume. (Left) The azimuthal angle ϑ_ν shows neutrinos peaked at around 1.7 ° away from the detector's z-axis. (Right) The polar angle φ_ν showing the origin of the asymmetry in the transverse plane.

$\varphi_\nu < -100$ °: corresponding to travelling upwards and to the right if looking downstream.

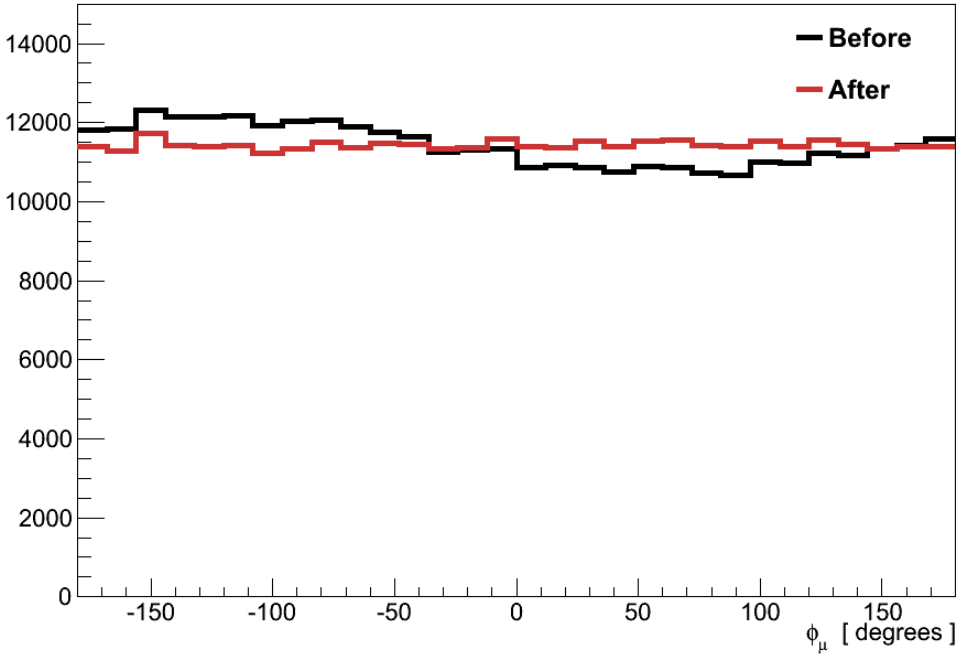

Figure 6.11: The true transverse polar angle φ_μ of primary muons from CC ν_μ interactions before and after the direction correction. Before the correction the muons are biased towards the region where φ_ν is peaked in Figure 6.10. After the correction the distribution is much flatter.

On average the final-state particles resulting from a neutrino interaction are produced isotropically in the plane perpendicular to the direction of the incoming neutrino. However the offset described above results in anisotropy when measured in the detector's co-ordinate system. For most measurements this difference is negligible, however it is more significant when dealing with transverse distributions.

Since this analysis will make a cut on transverse momentum, a correction is made to reduce this effect by rotating the directions/momenta of reconstructed objects to align with the mean neutrino direction. Using a large sample of true CC ν_μ interactions in the fiducial volume, the mean neutrino direction is calculated as u_ν = (-0.0127 , -0.0253 , 0.9996), with an angle $\vartheta_u = 1.62\,^\circ$.

As shown in Figure 6.11, this correction flattens out the anisotropy in the transverse angle of primary muons. More importantly, in Figure 6.12, this correction results in a more accurate measurement of the transverse momentum of the muon-pion system (defined in Section 6.6) for events in the coherent selection, reducing the RMS from 97 to 86 MeV, a roughly 10% improvement.

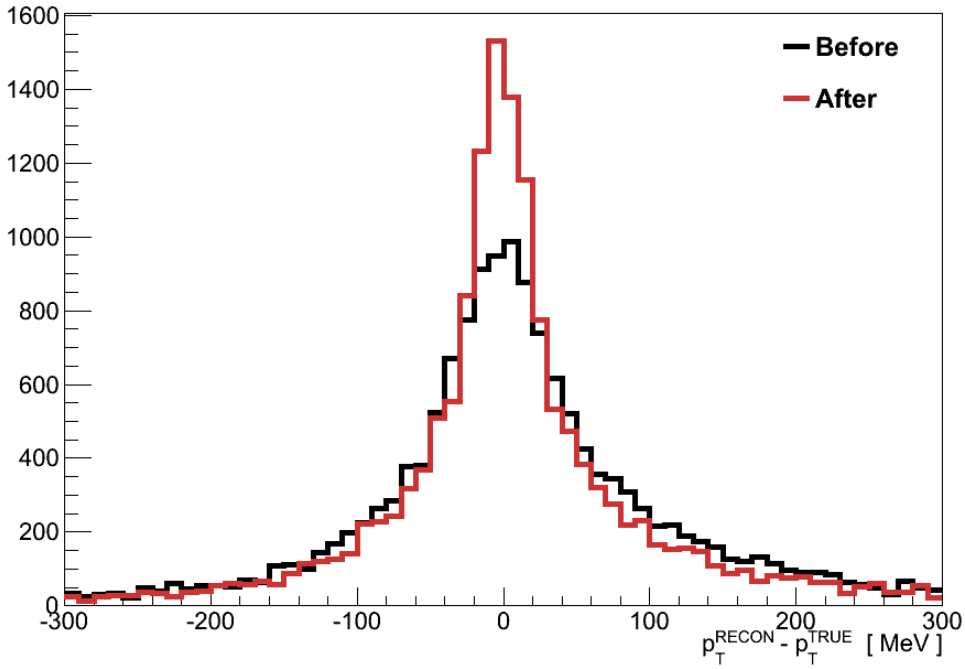

Figure 6.12: The resolution on the total transverse momentum in the muon-pion system before and after the direction correction. The frame of the true neutrino direction for each individual interaction is used to calculate ${p_T}^{\mathrm{TRUE}}$, while ${p_T}^{\mathrm{RECON}}$ uses the average direction as is done in data.

6.6. Transverse Momentum Cut

With the coherent selection made the next task is to reduce the amount of background that has come with it. This is done by cutting on two distributions, the first of which is on the total transverse momentum of the muon-pion system, p_T.

Under the assumption that the target nucleus with which a neutrino interacts is stationary, conservation of momentum requires that the complete system of final-state particles has no net momentum transverse to the incoming neutrino's direction. Although coherent interactions can transfer some momentum to the nucleus any large transfer would break coherence, so p_T tends to be small. Meanwhile background interactions which generated additional, unreconstructed particles can give larger values of p_T since the muon and pion no longer represent the complete final-state.

The value of p_T is calculated by taking the magnitude of the transverse component, of the vector sum of the muon and pion reconstructed momenta:

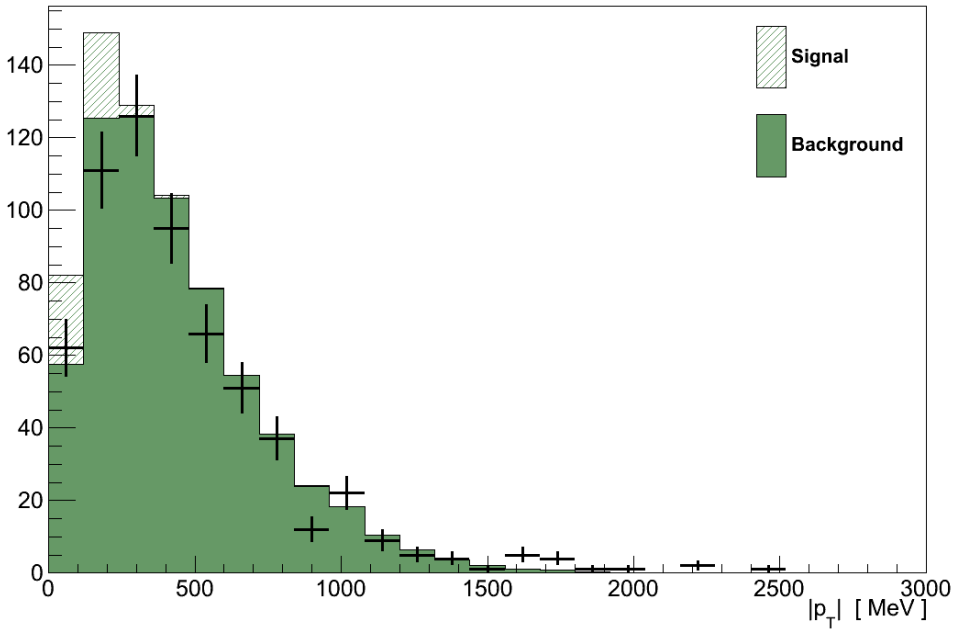

Figure 6.13: Net transverse momentum of the reconstructed muon and pion tracks. Events with $p_T \geq 190\,\text{MeV}$ are rejected.

$$p_T = \sqrt{\left(p_\mu^x + p_\pi^x\right)^2 + \left(p_\mu^y + p_\pi^y\right)^2} \tag{6.5}$$

As can be seen in Figure 6.13, coherent interactions tend to have low p_T while the background distribution extends to higher values. By maximising the product of signal efficiency and purity a cut value of 190 MeV was set, above which events are rejected.

6.7. Vertex Activity Cut

The second cut is made on the "vertex activity" (VA) in FGD 1 - a measure of the energy deposited around the vertex. This includes deposition from particles which produced reconstructed tracks and, crucially, also from short ranged particles which could not be reconstructed. The value of VA therefore is sensitive to the existence of additional final-state particles which exited the nucleus after a neutrino interaction, but did not have enough momentum to travel a sufficient distance in the detector to be reconstructed. Coherent interactions, which generate only a muon and pion, should have low VAs. Background events meanwhile may have generated any number of low

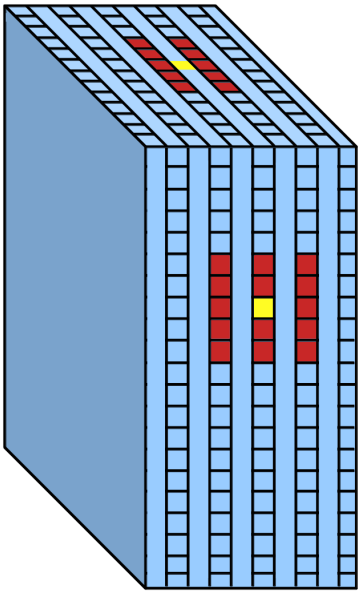

Figure 6.14: An illustration of how the FGD vertex activity is calculated. The yellow square represents the vertex position in the two detector views. The bars highlighted in red, and the vertex bar, contribute to the VA.

momentum protons or pions which, if they exited the nucleus, will have deposited their energy in the surrounding bars and increased the VA.

The VA is calculated for every track which starts inside the detector. Its calculation is illustrated by Figure 6.14. The 3D fitted position of the track's start is taken to be the vertex. Then a box is formed centred on the vertex, 5 layers deep and 5×5 bars high/wide, and all the bars in that volume are selected. The attenuation-corrected energy deposited in each of these bars is then summed to give the VA at the start of that track. No attempt is made to subtract the contributions from the muon and pion tracks to the energy deposited. Since there are two tracks associated with each event, the muon and pion candidates, the VA for the event is taken from the track with the upstream-most starting position.

The high VA tail generated by background events can be clearly seen in Figure 6.15, with coherent events all found peaked at lower values. By maximising the product of signal efficiency and purity a cut value of 290 PEU was set, above which events are rejected.

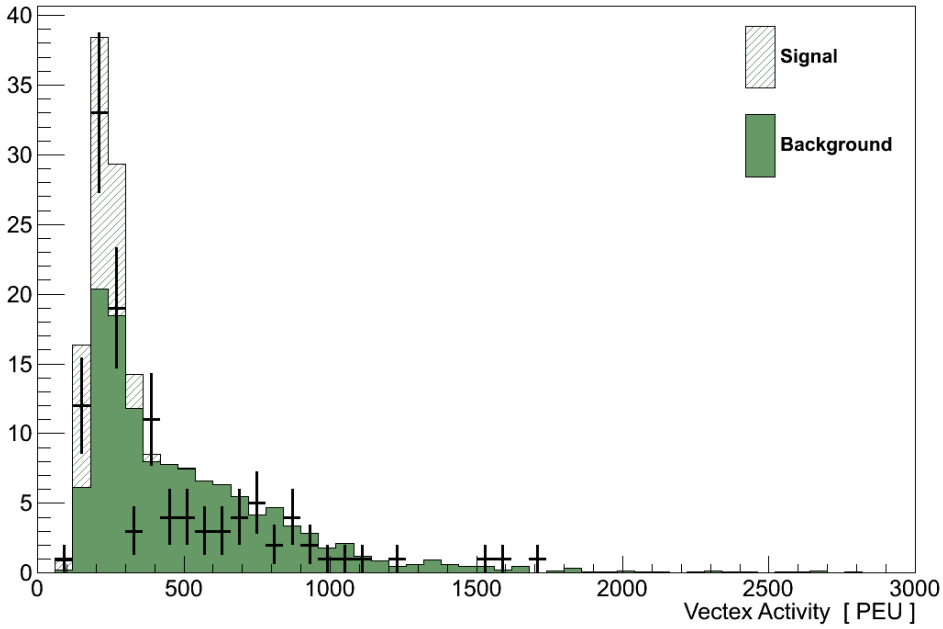

Figure 6.15: Vertex activity at the reconstructed vertex. Events with VA ≥ 290 PEU are rejected.

Step	Data	Simulation			
		Total	Signal	Efficiency	Purity
ν_μ Inclusive selection	10303	10016	96	78 %	1.0 %
Coherent Initial selection	620	704	52	42 %	7.4 %
p_T cut	122	169	43	35 %	25.3 %
VA cut	65	81	39	32 %	47.8 %

Table 6.6: Event numbers and performance measures after steps in the coherent initial selection, from data and simulation.

6.8. Selection Performance

The events which remain after these cuts are the coherent selection, which comprises 65 events in data. This compares with 81 events in the POT-scaled simulation, 39 of which are coherent signal interactions - an efficiency of 32 % and a purity of 48 % (Table 6.6).

Topology	Fraction
Muon + Pion	65 %
Muon + Proton	13 %
Muon + Pion + X	10 %
Anti-Muon + Pion + X	3 %
Muon + X (no pion)	2 %
Muon + Nothing	2 %
OOFV	2 %
NC + Pion + X	2 %
Muon + Proton + Pion	1 %
Other	< 1 %

Table 6.7: Final-state topology of simulated interactions in the coherent selection. "pion" refers exclusively to charged pions. X represents any combination of particles, with the exception of charged pions where stated, and such that there is no overlap between categories. Only particles with momentum > 200 MeV are counted.

As can be seen in Table 6.7, 76 % of the interactions selected were ones which included both a muon and pion. Ultimately, if an interaction produces a forward-going muon-pion pair with little or no momentum carried away by other particles, there is no way to separate it from a true coherent event.

Approximately half of the remaining background comes from events containing only a muon and a proton. At high-momentum the dE/dx of protons is similar to that of pions, making it difficult to separate this background out using the TPC PID. In future productions, where the ECal PID information is available, it may be possible to reduce this component. Some of the remaining topologies, such as OOFV or a lone muon, are likely the result of failures in the reconstruction, which again could be reduced by improvements in future versions of the ND280 software.

The interaction modes used by GENIE to generate the simulated events in the coherent selection are listed in Table 6.8. You may recall that the discussion in Chapter 3 concluded that experiments should be concerned with particle topologies, rather than simulator interaction models. However the interaction

Interaction	Fraction
CC ν_μ Coherent	48 %
CC ν_μ Resonance	21 %
CC ν_μ QE	12 %
CC ν_μ DIS	12 %
CC $\bar{\nu}_\mu$	3 %
OOFV	2 %
NC	2 %
CC ν_e / CC $\bar{\nu}_e$	< 1 %

Table 6.8: The interaction channel used by GENIE to generate simulated interactions in the coherent selection.

model used to simulate the background becomes relevant when considering the systematic uncertainties on that background prediction (Section 6.10.2).

Finally, Figure 6.16 shows the momenta and angles of the muon and pion candidate tracks from the coherent selection. Critically, there are no concerning features in these plots that would suggest the presence of an unaccounted background.

6.9. The Result Calculation Procedure

The goal of this analysis is to conduct a search for coherent pion production, and so far a sample of events which is tuned to select such interactions (if they take place) has been made. If coherent pion production is not taking place, or is doing so at a rate below the resolution of this analysis, the data in this selection should be consistent with the background prediction from simulation. If however there is a signal from coherent pion production, an excess of data above the background prediction could be observed. The remaining task then, is to define a method of assessing whether or not there is an excess of data above the background prediction, and if so how significant that excess is.

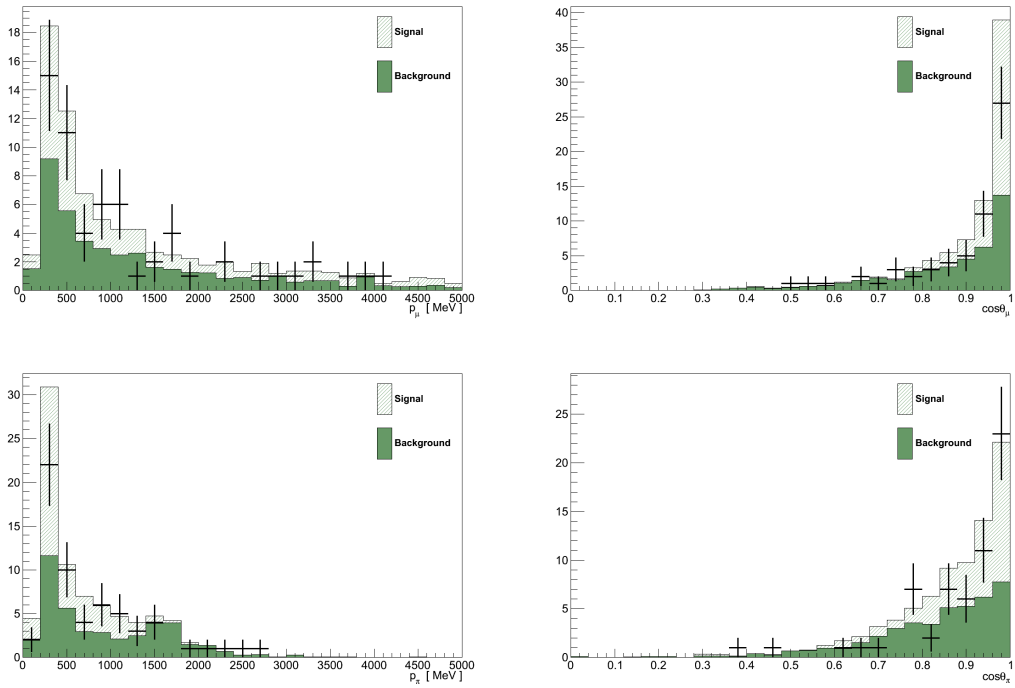

Figure 6.16: Kinematics plots of the muon and pion tracks from the coherent selection. (top) The candidate muon track. (bottom) The candidate pion track. (left) The candidate track's momentum. (right) The direction-corrected angle of the candidate track with respect to the incoming neutrinos.

As discussed in Chapter 3, there are significant uncertainties surrounding the simulation of our background processes, so the method should attempt to reduce its sensitivity to such uncertainties. It is also important that any excess detected should be consistent with the type of excess expected of a coherent signal - not just a general excess in the number of events selected.

The method chosen was to pick a kinematic distribution in which coherent pion production has a characteristic behaviour. This distribution is then separated into a "signal region", where coherent events would be expected to appear in addition to some background, and a "control region" which contains only background events. The number of events in the control region can then be used to constrain the expected number of background events in the signal region - removing uncertainties from the absolute normalisation of the background. Using this constrained background prediction, an excess of events can be sought in the signal region.

A distribution which meets these requirements is $|t|$:

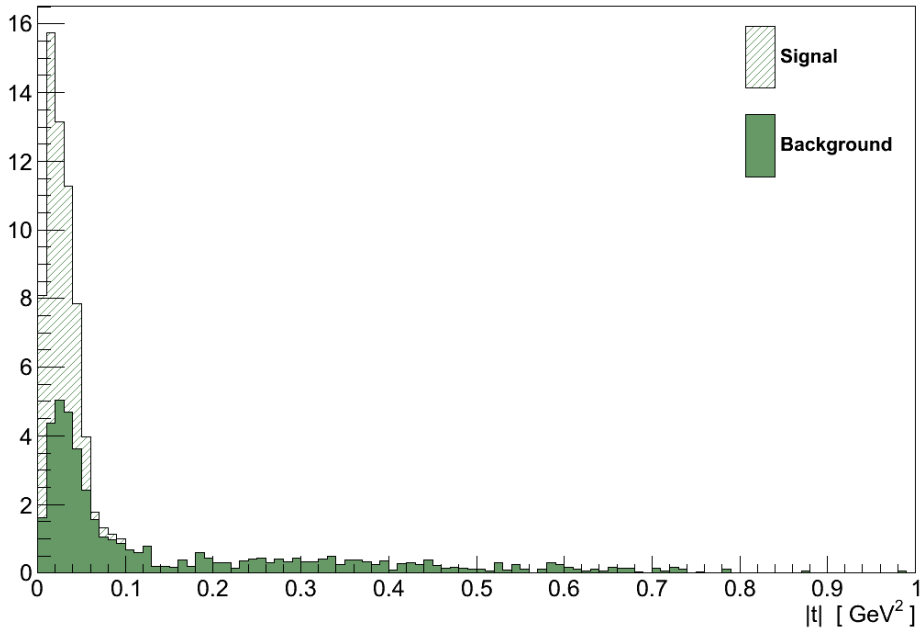

Figure 6.17: The |t| distribution from simulation. The signal region is defined as |t| $< 0.09\,\mathrm{GeV}^2$

$$\mid t \mid \;=\; \left| \left(q - P_{\pi}\right)^2 \right| \;=\; \left| \left(\left(P_{\nu} - P_{\mu}\right) - P_{\pi}\right)^2 \right| \tag{6.6}$$

The four-momenta of the muon and pion, P_{μ} and P_{π}, can be determined from the three-momenta measured in the detector, however the neutrino's four-momentum, P_{ν}, must be inferred. By making the assumption that the recoiling nucleus takes only momentum, and no energy, from the interaction - an assumption commonly referred to as the "infinitely heavy nucleus" - the neutrino's four-momentum is taken to be:

$$P_{\nu} = \left(E_{\nu},\, 0,\, 0,\, E_{\nu}\right) = \left(E_{\mu} + E_{\pi},\, 0,\, 0,\, E_{\mu} + E_{\pi}\right) \tag{6.7}$$

which gives all the information required to calculate |t|.

Recalling Chapter 4, |t| is a measure of the momentum transfer to the nucleus, small values of which is a characteristic feature of coherent interactions as can be seen in Figure 6.17. This makes |t| an ideal match to the requirements set out above.

The position of the split between the signal and control regions was set as $0.09\,\mathrm{GeV}^2$ by finding the largest possible control region which remains $\geq 99\,\%$ background-pure.

The result calculation, which follows a prescription by Glen Cowan et al. [82], begins by taking the counts in each of the two regions measured in data:

- n_D - total number of events in signal region
- m_D - total number of events in control region

A model of the underlying physics is then constructed using four parameters:

- s - number of signal events in the signal region
- b - number of background events in the signal region
- τ - ratio of background events in signal and control regions
- μ - signal strength, a multiplicative factor which scales s

This model then returns the expected counts in the signal and control region as:

- $n_E = \mu s + b$
- $m_E = \tau b$

The likelihood of the measured data being produced by a given choice of model is then the product of Poisson probabilities for the counts, and a Gaussian probability for τ compared with its nominal value and uncertainty:

$$\mathrm{L}\left(\mu,\, \tau,\, b\right) = \left(\frac{{n_E}^{n_D} e^{-n_E}}{n_D!}\right)\left(\frac{{m_E}^{m_D} e^{-m_E}}{m_D!}\right) e^{\frac{-\left(\tau - \tau_{\mathrm{nominal}}\right)^2}{2{\sigma_\tau}^2}} \tag{6.8}$$

This is more convenient to calculate by taking the natural logarithm which, up to a constant which is irrelevant for maximisation and will cancel in a forthcoming ratio, is approximately:

$$\ln\ \mathrm{L}\left(\mu,\ \tau,\ b\right) = \left[n_E - n_D\left(1 - \ln\left(\frac{n_D}{n_E}\right)\right)\right] + \left[m_E - m_D\left(1 - \ln\left(\frac{m_D}{m_E}\right)\right)\right] + \left[\frac{\tau - \tau_{\text{nominal}}}{\sigma_\tau}\right]^2 \tag{6.9}$$

Using this definition, the model can be fit to the data by finding the values of the parameters which maximise the likelihood.

In this analysis the signal count in the signal region, s, is taken directly from that predicted in simulation and kept constant throughout (i.e. it was not allowed to vary during fitting). It is the signal strength, μ, which allows its contribution to vary. The simulation also provides the value of τ_{nominal}. The uncertainty on τ_{nominal}, σ_τ, will be determined in Section 6.10, and represents the sole source of systematic uncertainty.

In general, when maximising the likelihood the values of b, τ and μ are allowed to vary. The first term in Equation 6.9 measures the degree of agreement in the signal region - the principle measure of how well the model describes the data. Meanwhile, the second and third terms in Equation 6.9 control the expected background in the signal region. Though b is allowed to vary, the data count in the control region, m_D, constrains it in the second term, since $b = m_E/\tau$. While some freedom is allowed for the value of τ to vary from the nominal value predicted in simulation, the third term penalises large excursions relative to the uncertainty on it.

This is an important feature of the calculation that's worth emphasising. The result is independent of the absolute normalisation of the background in simulation. Only the shape of the background, between the signal and control regions, is taken from simulation. It is the data in the control region, m_D, which provides the background normalisation.

With the likelihood defined, and the procedure for maximising it determined, there are three statistical tests which could be made for this analysis:

- **Search for an excess**. This is the primary output of the analysis, measuring the significance of any excess found above the background prediction.

  Using Equation 6.8 the likelihood of a given set of model values producing the observed data can be calculated. Fixing the signal strength according

to a hypothesis, and allowing the remaining parameters to vary until they maximise the likelihood gives the maximum likelihood of that hypothesis producing the data. But this does not reveal how good a match that hypothesis is relative to others.

To do this a measure of how well a hypothesis fits the data relative to the best possible fit, the maximised likelihood-ratio, is calculated:

$$\lambda\left(\mu\right) = \frac{\mathrm{L}\left(\mu,\, \tau',\, \mathrm{b}'\right)}{\mathrm{L}\left(\mu',\, \tau',\, \mathrm{b}'\right)} \tag{6.10}$$

Here, the presence of a prime on μ, τ or b indicates that the value of those parameters are those which maximise the likelihood. So $\mathrm{L}(\mu',\tau',\mathrm{b}')$ takes the values of μ, τ and b which best-fit the data, while $\mathrm{L}(\mu,\tau',\mathrm{b}')$ is calculated at the value of τ and b which best describes the data for a given value of μ.

When testing the background-only hypothesis, it must be determined how significant any deviation of μ' from 0 is. To do this the value of $\ln\lambda(0)$ from data can be compared with the distribution of values that would be expected. So called "pseudo-experiments" are generated by drawing randomised values for $\mathrm{m_D}$, $\mathrm{n_D}$ (from Poisson distributions with means $\mathrm{m_E}$ and $\mathrm{n_E}$ respectively) and τ (from a Gaussian distribution centred at τ_{nominal} with width σ_τ). For each pseudo-experiment the value of $\ln\lambda(0)$ is then calculated. The resulting distribution is that to be expected if the background-only hypothesis were true. Taking the fraction of pseudo-experiments with $\ln\lambda(0)$ greater than that measured in data is a P-value for the data, which indicates the compatibility of the data with $\mu = 0$ (a smaller P-value indicating a more significant excess).

This P-value can be converted to a more intuitive statistical significance by finding the number of standard deviations at which a normal distribution gives that same P-value. The larger the value of this significance the stronger the indications that there is an excess of data in the signal region.

- **Set an upper-limit**. In the case that no significant excess is observed, it would be interesting to calculate the largest possible signal strength which could still produce a result that is compatible with the background.

By generating the $\ln\lambda(\mu)$ distribution with pseudo-experiments, the P-value for the distribution below the value from data indicates how compatible such a signal strength would be with the background. A 90 % upper-limit, for example, can then be set by finding the largest value of μ for which this lower P-value is 0.9.

- **Measure the signal strength**. In the case that a significant excess is found, the signal strength which best matches the data can be found trivially. It is the value of μ' from the denominator in Equation 6.10, where all the free parameters were allowed to vary to find the maximum likelihood.

Using this procedure it is possible to assess the significance of any excess of events found in the coherent selection, and to provide some interpretation of that significance whether it is large or small. It is important to note however, that any interpretation made of the significance, is done in the context of the coherent model which provided the value of s.

Before proceeding with the result calculations, there is one remaining undetermined input: the uncertainty on the background ratio, σ_τ, through which systematic uncertainties enter into the analysis.

6.10. Systematic Uncertainties

Systematic uncertainties deal with uncertainty in the accuracy of the simulation at describing the data, and therefore reflect variation that can result from differences between the two. For this analysis they can be classified under three categories:

- The flux systematic is a result of uncertainties in the predicted neutrino flux at ND280.
- Interaction systematics deal with uncertainties in the models contained within GENIE, including the nuclear model, neutrino interaction cross-section models and final-state interaction models.
- Detector systematics deal with uncertainties stemming from the simulation of the experiment, including the description of the detector

and magnetic fields, the passage of particles through the detector and the response of the detector's electronics to the energy deposited.

In some cases these systematics can be studied by the variation of underlying parameters in the models used, in others they come from studying the possible variations on the resulting properties which are measured. Regardless, systematic uncertainties only affect the analysis when they cause changes in the value of τ, the nominal value of which is $\tau_{\text{nominal}} = 1.43$. For the systematics studied below, only background events are used, and only changes in the shape of the backgrounds need be considered.

6.10.1. Flux Systematic

The systematic uncertainty in the predicted neutrino flux is assessed by the T2K Beam group, predominantly using NA61/SHINE data, and provided to analysers in the form of a covariance matrix binned by neutrino flavour and energy [83].

In order to assess this effect, the analysis was re-run 10000 times. Each time the analysis was re-run, weights for each neutrino flavour-energy bin were generated according to the size and correlations of the uncertainty in each bin described by the covariance matrix. Every event was given a weight based on the flavour and energy bin to which the initial neutrino belonged, effectively simulating the effect of a variation in the flux. In each re-run the value of τ was calculated and recorded.

A Gaussian fit was made to the resulting distribution of τ values (Figure 6.18), and the systematic uncertainty from the flux taken to be the standard deviation, $\sigma_\tau^{\text{FLUX}} = 0.042$.

6.10.2. Interaction Systematics

As discussed in Chapter 3, there is a great deal of uncertainty in our knowledge of neutrino interaction physics. As a consequence the models used in

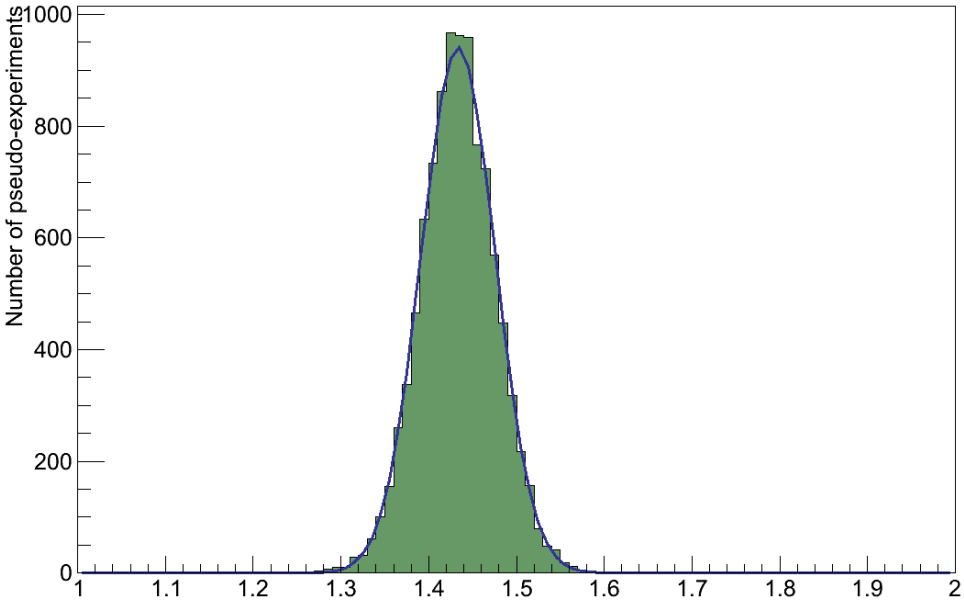

Figure 6.18: The values of τ resulting from 10000 variations of the flux, with its Gaussian fit overlaid.

interaction simulations, such as the GENIE simulation [31] used in this analysis, also carry a great deal of uncertainty with them.

The GENIE simulation provides re-weighting tools which, for a given neutrino interaction, calculate weights corresponding to the effect of varying the values of underlying parameters used in GENIE's models. The GENIE collaboration have also determined estimates of the uncertainties on these model parameters, by comparing the outputs from GENIE under variations of those parameters with a large body of experimental data. The GENIE models and their parameters are described in detail in its user manual [84] and the value of the uncertainties placed on each parameter are discussed along with the procedure by which they are treated in a T2K technical note [85].

Most of the parameters can be classified as belonging to the models for the basic cross-sections (GXSec), the creation of hadrons from fragmented nucleons (GHadr), the interactions of final-state particles as they travel through the nucleus (GINuke), or the decay of particles within the nucleus (GRDcy).

For some parameters GENIE provides two alternatives for the study of their effects. For example the axial mass (M_A) in the CC QE model can either be

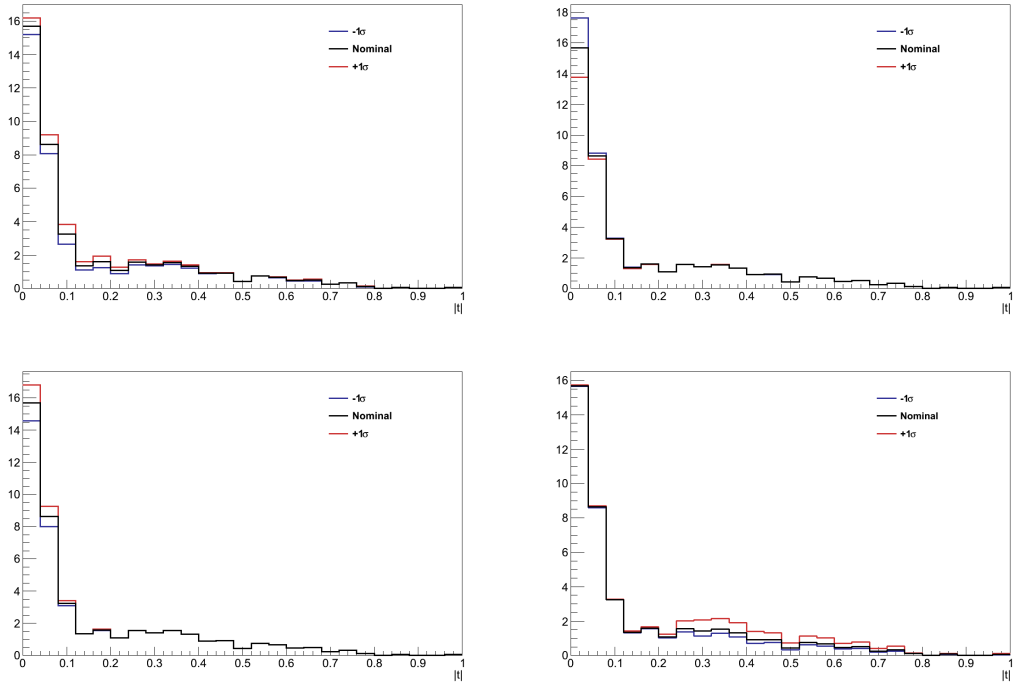

Figure 6.19: Variations in the |t| distribution resulting from re-weighting of four of the more significant parameters. (top left) GXSec_RvnCC1pi - the fraction of DIS events generating a single pion final-state. (top right) GRDcy_Theta_Delta2Npi - choice between Δs decaying isotropically or an-isotropically. (bottom left) GINuke_FrAbs_N - The cross-section for nucleon absorption in the nucleus. (bottom right) GXSec_MaCCQE - The M_A parameter from the axial-vector form-factor in the CC QE cross-section.

studied directly as a single parameter, or by decomposing its effects to two separate parameters - one for the effect on normalisation of the CC QE cross-section, and one for the effect on its Q^2-shape. In such instances, only the combined single parameters were used in this study.

Software developed within the T2K collaboration, "T2KReWeight" [86], provides an interface to the GENIE re-weighting functionality, allowing the re-weighting of simulated neutrino interactions selected in ND280 analyses.

The procedure adopted for assessing the effect of the uncertainty on these parameters was to run the analysis twice for each parameter, once varying that parameter by $+1\sigma$, and once varying it by -1σ. In each case, T2KReWeight was used to retrieve weights for the true interaction selected in the analysis, and that weight was applied to the event. Figure 6.19 shows the effect on the |t| distribution of re-weighting in this way, for examples of four of the more significant parameters.

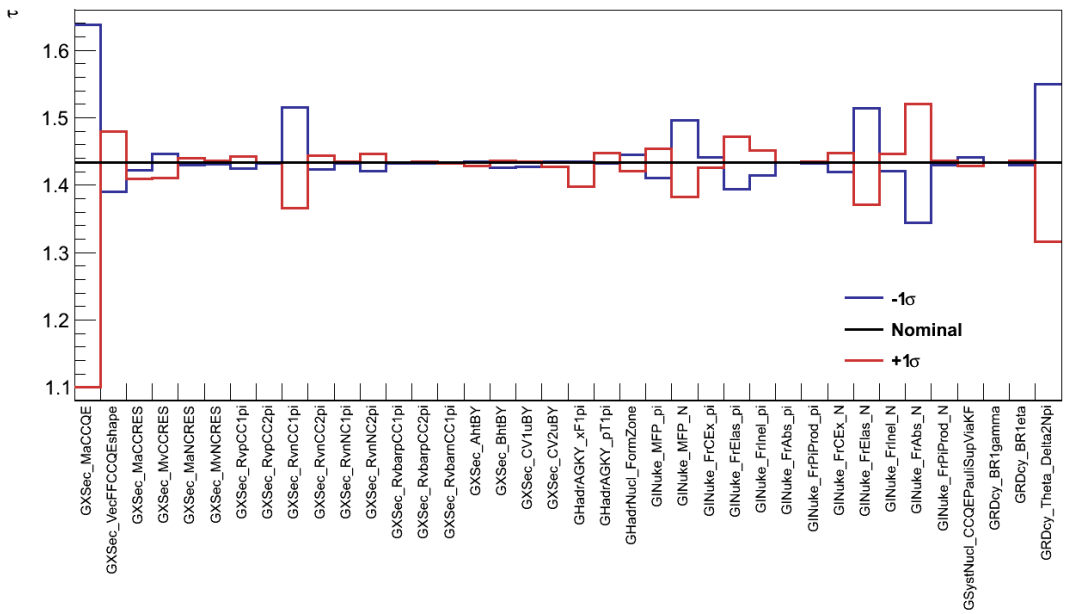

Figure 6.20: The values of τ resulting from +1σ and -1σ variations of GENIE interaction parameters. Only those parameters which affected the analysis are shown.

The values of τ resulting from this re-weighting were then calculated for the two shifts of each parameter, and are shown in Figure 6.20 for the parameters which affected the analysis. For each parameter, the largest shift in the value of τ was taken to be the uncertainty from that parameter. The total uncertainty resulting from the interaction modelling was then taken from the sum-in-quadrature of all the parameters: $\sigma_\tau^{\text{INTERACTIONS}} = 0.398$.

As mentioned, the GENIE manual [84] provides a thorough description of the various models, their parameters and parameter uncertainties. For information, the list of parameters which affect the analysis and their uncertainties are shown in Table 6.9. For the more significant parameters in this analysis the descriptions in the GENIE manual are summarised:

- **Cross-Section Form-Factors**
  Variations in the form-factors for CC QE and resonance production are simply treated by calculating the differential cross-section for the given interaction with the nominal and alternative values of the parameters. The interaction then simply receives a weight corresponding to the change of the differential cross-section.

  It is clear that the CC QE axial-mass form-factor parameter (GXSec_MaCCQE) dominates the interaction uncertainty. As can be

Parameter Name	Parameter Description	σ [%]
GXSec_MaCCQE	Parameter in CC QE axial form-factor	25
GXSec_VecFFCCQEshape	Choice of CC QE vector form-factors (BBA05 / dipole)	-
GXSec_MvCCRES	Parameter in CC resonance vector form-factor	10
GXSec_MaCCRES	Parameter in CC resonance axial form-factor	20
GXSec_MvNCRES	Parameter in NC resonance vector form-factor	10
GXSec_MaNCRES	Parameter in NC resonance axial form-factor	20
GXSec_RvpCC1pi	Non-resonance ν CC 1π	50
GXSec_RvpCC2pi	Non-resonance ν CC 2π	50
GXSec_RvnCC1pi	Non-resonance ν CC 1π	50
GXSec_RvnCC2pi	Non-resonance ν CC 2π	50
GXSec_RvnNC1pi	Non-resonance ν NC 1π	50
GXSec_RvnNC2pi	Non-resonance ν NC 2π	50
GXSec_RvbarpCC1pi	Non-resonance $\bar{\nu}$ CC 1π	50
GXSec_RvbarpCC2pi	Non-resonance $\bar{\nu}$ CC 2π	50
GXSec_RvbarnCC1pi	Non-resonance $\bar{\nu}$ NC 1π	50
GXSec_AhBY	A_{HT} parameter in Bodek-Yang (DIS) model scaling variable ξ_W	25
GXSec_BhBY	B_{HT} parameter in Bodek-Yang (DIS) model scaling variable ξ_W	25
GXSec_CV1uBY	C_{V1u} u-quark valence GRV98 PDF correction parameter in Bodek-Yang (DIS) model	30
GXSec_CV2uBY	C_{V2u} u-quark valence GRV98 PDF correction parameter in Bodek-Yang (DIS) model	40
GHadrAGKY_xF1pi	Pion Feynman-x PDF for Nπ states in AGKY (hadronisation model)	-
GHadrAGKY_pT1pi	Pion transverse momentum PDF for Nπ states in AGKY (hadronisation model)	-
GHadrNucl_FormZone	Hadron formation zone length	50
GINuke_MFP_pi	π mean free path (total rescattering probability)	20
GINuke_MFP_N	Nucleon mean free path (total rescattering probability)	20
GINuke_FrCEx_pi	π charge exchange probability	50
GINuke_FrElas_pi	π elastic reaction probability	10
GINuke_FrInel_pi	π inelastic reaction probability	40
GINuke_FrAvs_pi	π absorption probability	20
GINuke_FrPiProd_pi	π probability	20
GINuke_FrCEx_N	Nucleon charge exchange probability	50
GINuke_FrElas_N	Nucleon elastic reaction probability	30
GINuke_FrInel_N	Nucleon inelastic reaction probability	40
GINuke_FrAvs_N	Nucleon absorption probability	20
GINuke_FrPiProd_N	Nucleon probability	20
GSystNucl _CCQEPauliSupViaKF	CC QE Pauli suppression (via k_F)	35
GRDcy_BR1gamma	Branching ratio for radiative resonance decays	50
GRDcy_BR1eta	Branching ratio for single-η resonance decays	50
GRDcy_Theta_Delta2Npi	Choice of pion angular distribution in $\Delta \rightarrow \pi N$ (isotropic / Rein-Sehgal)	-

Table 6.9: List of GENIE systematic parameters and their uncertainties

seen in the bottom-right of Figure 6.19 this is a result of almost all the CC QE background lying within the control region, and hence any changes of their normalisation have a direct effect on τ. This is further exaggerated by the high 25 % uncertainty currently assigned to this

parameter, predominantly motivated by the fitting of larger values of M_A in MiniBooNE.

- **Inelastic Cross-Sections**
  As was discussed in Chapter 3, inbetween the regions dominated by resonance and DIS interactions is a "transition region", where the target nucleon can produce off-shell resonances or is partly fragmented but does not clearly fall into either category.

  This can be modelled as some combination of resonance and DIS models, but simply summing them would result in double-counting. In GENIE this is treated by combining the resonance model with a scaled and modified version of the DIS model below a threshold in invariant hadronic mass (W $< 1.7\,\mathrm{GeV}$). In this region the DIS contribution is:

$$\frac{\mathrm{d}^2\,\sigma^{\mathrm{DIS}}(W, \,<, 1.7)}{\mathrm{d}\,Q^2\,\mathrm{d}\,W} = \frac{\mathrm{d}^2\,\sigma^{\mathrm{DIS}}}{\mathrm{d}\,Q^2\,\mathrm{d}\,W} \sum_m R_m P_m \tag{6.11}$$

  Where m refers to the initial state and the multiplicity of the hadronic system (m = νpCC1π, νpCC2π, νnNC1π...), and P_m is the default probability of that final hadronic system from the hadronisation model. The R_m are then tunable parameters which scale each of the different components. The values of the R_m, and uncertainties on them, are set by the GENIE collaboration by fitting data on inclusive, 1π and 2π final-states from multiple experiments.

  The uncertainty in these R_m parameters are controlled in the re-weighting by the parameters beginning "GXSec_R". As is to be expected, the uncertainty on those parameters which relate to final states containing pions are those which affect this analysis the most, in particular GXSec_RvnCC1pi which for ν_μ corresponds to the production of $\mu^- + \pi^+$ topologies.

- **INTRANUKE**
  The INTRANUKE/hA model is the intra-nuclear rescattering model implemented in GENIE, which determines the effect on hadronic particles of propagating out through the nuclear environment. During this propagation particles may undergo elastic scattering, inelastic scattering, charge exchange or absorption. The model has been extensively tuned on

scattering data from other fields, particularly hadron-nucleus scattering and photon-nucleus scattering.

Essentially the INTRANUKE/hA model selects either survival or rescattering as the fate of a hadron (h = π,N) at δr = 0.05 nm steps acording to the probabilities calculated:

$$P^{h}_{\text{resccat}} = 1 - P^{h}_{\text{survive}} = 1 - \int e^{\frac{-r}{\lambda^{h}}} \, \mathrm{d}\, r \tag{6.12}$$

Where r is the position of the hadron within the nucleus, and λ^{h} is the mean free path of that hadron, which is a function of its position and energy, E:

$$\lambda^{h} = \frac{1}{\varrho\,(r)\sigma^{\mathrm{hN}}(E)} \tag{6.13}$$

With ϱ the nuclear density, and σ^{hN} the total interaction cross-section for that hadron with a nucleon.

If the hadron is determined to rescatter at any point an interaction mode is chosen according to the relative sizes of their respecitve cross-sections (see Figure 6.21). The fate of hadrons simulated to result from that interaction must also then be calculated.

The re-weighting paramaters beginning "GINuke_MFP" modify the mean free paths, λ^{h} acording to the uncertainty assigned to them from the data tuning mentioned earlier. An event then receives a weight which is the product of weights assigned to each of the primary hadrons generated at the neutrino interaction vertex. The weight given to each primary hadron is calculated from the change in its survival probability. If $\mathrm{P}_{\text{survive}}$ increases for a hadron which did survive it is weighted up. If $\mathrm{P}_{\text{survive}}$ decreases for a hadron which did survive it is weighted down. The inverse is applied to primary hadrons which did not survive.

The re-weighting parameters beginning "GINuke_Fr" alter the fraction of hadron rescatters assigned to each of the possible interaction modes.

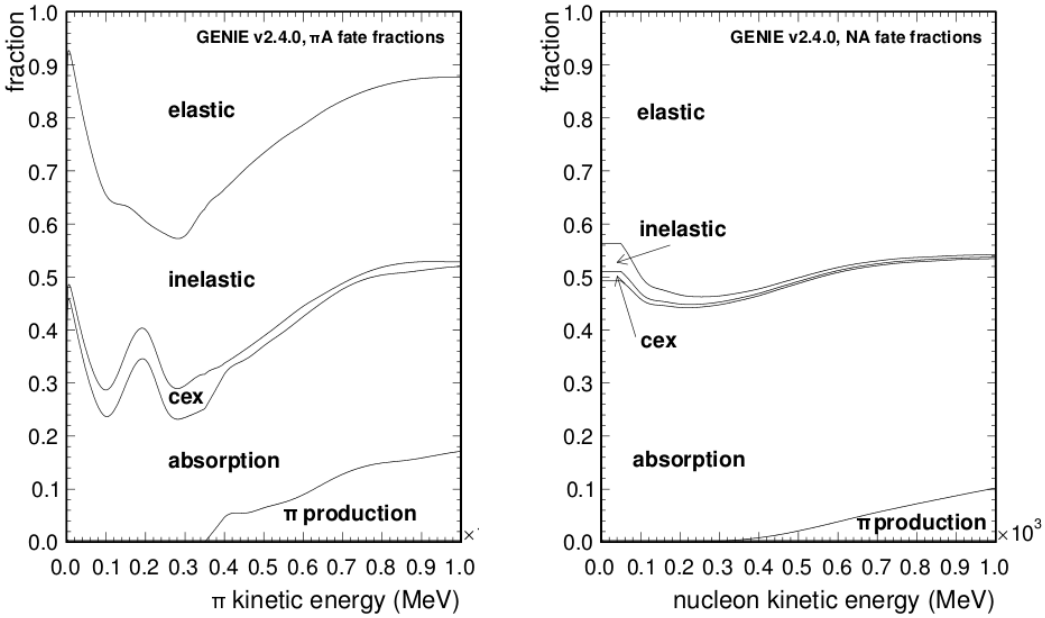

Figure 6.21: For hadrons determined to undergo rescattering in INTRANUKE/hA, the fractions of each scattering mode available to them as a function of their kinetic energy, for pions (left) and nucleons (right) [85].

Again, events are given a weight which is the product of weights assigned to each of its primary hadrons. The primary hadrons receive a weight if their fate was to undergo the interaction, proporitonal to the change in that interaction's fraction.

The intra-nuclear interactions of pions directly affect their number which escape the nulceus, and the intra-nuclear interactions of nucleons can often result in additional pions being created. The fact that many of the INTRANUKE/hA re-weighting parameters strongly affects the background events in this analysis is consistent with expectations.

- **Δ Decay Kinematics**
  The parameter GRDcy_Theta_Delta2Npi has a significant effect on the analysis. This is unsurprising since it controls the angular distribution of π^+ resulting from the decay of Δ resonances, and it is clear that a more forward-peaked distribution would result in lower reconstructed values of $|t|$.

  A general expression of the angular distribution, W_π, of pions from $\Delta \rightarrow N\ \pi^+$ [84]:

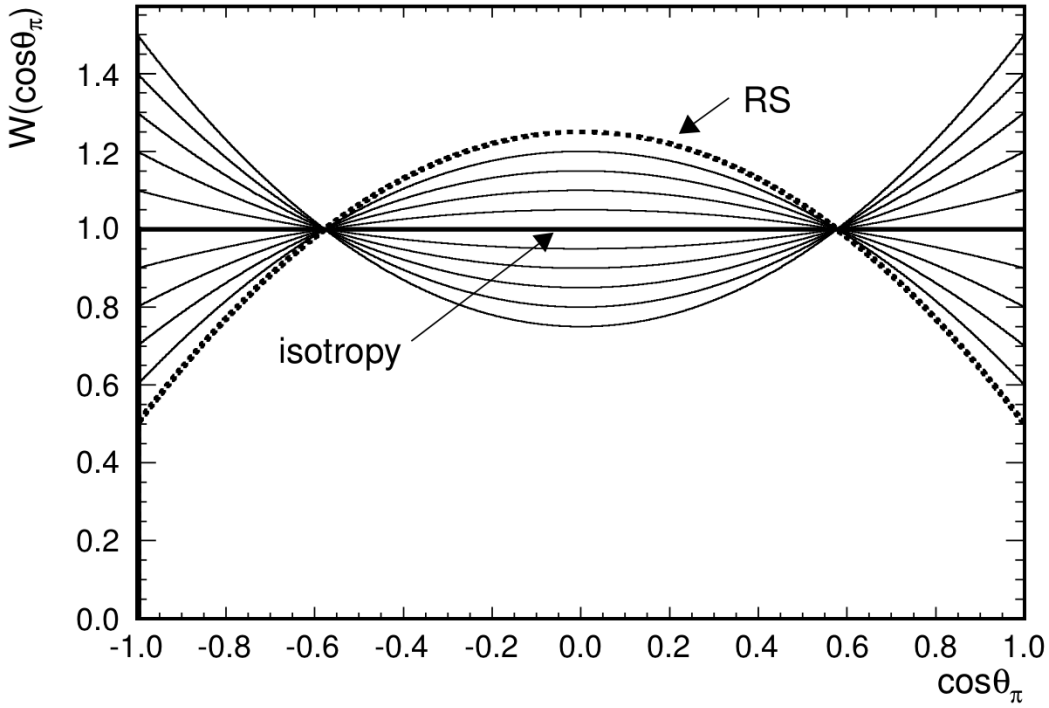

Figure 6.22: The angular distribution of pions resulting from Δ decays for values of GRDcy_Theta_Delta2Npi ranging from -1σ, through 0σ (isotropy), to +1σ (Rein-Sehgal) [84].

$$W_\pi\Big(\cos\vartheta_\pi\Big) = 1 - \ \mathrm{p}\left(\frac{3}{2}\right)\mathrm{P2}\left(\cos\vartheta_\pi\right) + \ \mathrm{p}\left(\frac{1}{2}\right)\mathrm{P2}\left(\cos\vartheta_\pi\right) \qquad (6.14)$$

Where p(3/2) and p(1/2) are coefficients, and P2 is the 2nd order Legendre polnomial. The Rein-Sehgal resonance model [22] predicts p(3/2) = 0.75, p(1/2) = 0.25. However, for simplicity, GENIE decays Δs isotropically (effectively p(3/2) = p(1/2) = 0.5).

The effect of re-weighting GRDcy_Theta_Delta2Npi, which corresponds to varying this distribution from isotropy (0σ) to Rein-Sehgal (+1σ) or any step inbetween, is shown in Figure 6.22.

6.10.3. Detector Systematics

There are numerous systematic differences in the simulation of the detector that could affect this analysis:

- differences in the reconstruction efficiency, particularly those which are a function of a track's angle or momentum
- differences which affect the measurement of a track's properties, particularly its direction or momentum
- differences in the passage of particles through the detector, particularly when it affects their ability to make reconstructible tracks
- differences in the measurement of energy deposited at the vertex

The categorisation, treatment and quantification of the detector systematics here broadly follows that which was done for the ND280 ν_μ Inclusive analysis [78] [79] and its supporting studies.

6.10.3.1. Momentum Resolution

There are two potential sources of systematic difference in the reconstructed momentum of a track: the absolute value of the measurement, and the resolution of the measurement.

The reconstruction measures a track's momentum from the component of the momentum transverse to the magnetic field, p_B. The resolution on $1/p_B$ is approximately Gaussian and, as mentioned in Section 6.2, it is found that this is $32 \pm 10\,\%$ worse in data than in simulation. A correction was applied to account for the 32 % difference, so the remaining uncertainty on the momentum resolution is $\sigma(1/p_B) = 10\,\%$ [81].

To assess the effect of this uncertainty, the analysis was re-run 10000 times, each time selecting a new resolution, δ_σ, from a Gaussian centred at 1.0 with width 0.1. The muon and pion tracks' $1/p_B$ were then adjusted based on this change of resolution in the same way as the initial correction (Equation 6.1):

$$\frac{1}{p_B^{\text{new}}} = \frac{1}{p_B^{\text{true}}} + \delta_\sigma \left(\frac{1}{p_B^{\text{initial}}} - \frac{1}{p_B^{\text{true}}} \right) \tag{6.15}$$

The tracks' reconstructed momentum was then updated based on the new value of $1/p_B$, and the resulting value of τ recorded. The resulting distribution

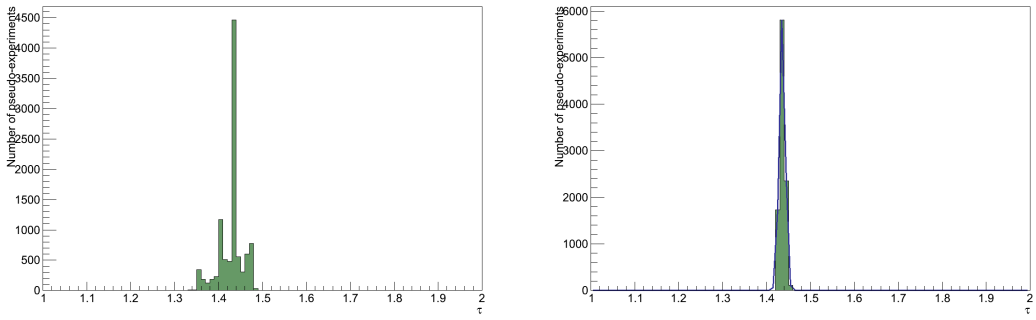

Figure 6.23: Values of τ resulting from variation of the reconstructed momentum. (left) Variation of the momentum resolution. (right) Variation of the momentum scale, with its Gaussian fit overlaid.

was non-Gaussian with quantised spikes as a result of events migrating across the p_T cut (Figure 6.23). Since a Gaussian fit cannot be made to this distribution, the largest deviation in the value of τ was taken to be the uncertainty from the momentum resolution: $\sigma_\tau^{\text{P-RESOLUTION}} = 0.084$.

6.10.3.2. Momentum Scale

The second possible systematic difference in the momentum can come from the absolute scale of the measurement, which is dominated by uncertainty in the strength of the magnetic field. Using measurements of the magnetic field taken with Hall probes inside ND280, the uncertainty on the magnetic field strength is found to be 0.5 %[87].

To assess the effect of this uncertainty, the analysis was re-run 10000 times, each time selecting a new scale factor from a Gaussian centred at 1.0 with width 0.005. The muon and pion tracks' momentum were then scaled according to this factor, and the resulting value of τ recorded. A Gaussian fit was made to the resulting distribution of τ values (Figure 6.23) and the uncertainty from the momentum scale taken from its width: $\sigma_\tau^{\text{P-SCALE}} = 0.0069$.

6.10.3.3. FGD-TPC Matching

In order to enter this analysis, the ND280 reconstruction must successfully match the reconstructed tracks left by the muon in FGD 1 and TPC 2. If the

efficiency, ε, of this matching differs between data and simulation as a function of momentum or angle, the resulting value of τ could also differ.

Using high statistics samples of cosmic-ray and T2K beam muons, a study of this matching efficiency concluded that the uncertainty on data-simulation agreement for ε did vary as a function of momentum and angle [88]. The study reported matching efficiency uncertainties, ${\sigma_\varepsilon}^{ij}$, for sixteen bins in muon momentum and angle (four of each, indexed by i and j) with values ranging in magnitude: $0.21\,\% \leq {\sigma_\varepsilon}^{ij} \leq 1.25\,\%$. These uncertainties were stated to be uncorrelated.

To assess the effect of a systematic difference in the matching efficiency between data and simulation, two weights were calculated for each muon momentum-angle bin, corresponding to an increase or decrease in efficiency:

$$w_{\pm}^{ij} = 1.0 \pm \sigma_{\varepsilon}^{ij} \tag{6.16}$$

Each momentum-angle bin was then considered independently, twice: once calculating the effect on τ of an increase in efficiency, and once for a decrease. This was done by weighting those events whose muon fell in that momentum-angle bin by the value calculated in Equation 6.16. In each case the shift, ${\delta_\tau}^{ij}(\pm)$, in the resulting value of τ was calculated and the magnitude of the largest shift for each bin was taken to be the uncertainty in that bin:

$$\sigma_{\tau}^{ij} = \max\left(\delta_{\tau}^{ij}(+),\, \delta_{\tau}^{ij}(-)\right) \tag{6.17}$$

The sum-in-quadrature of all ${\sigma_\tau}^{ij}$ was then taken to give the total uncertainty resulting from the FGD 1-TPC 2 efficiency matching as: ${\sigma_\tau}^{\text{MATCHING}} = 0.0025$.

6.10.3.4. TPC Track Quality Cut

Both the selection of the muon and pion candidate tracks include the requirement that they have a "good" component in TPC 2, defined as a TPC 2 track with hits on ≥ 18 of the micromegas' readout columns (the TPC

reconstruction is based on initially clustering of hits vertically). A difference in the efficiency of detecting those hits, ε, between data and simulation could result in tracks migrating across this 18 hit cut. If the susceptibility of a track to crossing that cut has a momentum or angle dependence, such a difference could also result in a change in τ.

A comparison of the number of vertical clusters between data and simulation was made for muon candidate tracks from the ν_μ Inclusive selection, where the track crossed two micromegas in TPC 2 ($\geq$ 62 vertical clusters). The difference in hit efficiency between data and simulation was then found by modelling the effect of such a difference on the distribution from simulation, and fitting the data distribution. A variety of studies as a function of location, momentum, angle etc. concluded that in all cases the difference in hit efficiency [88]:

$$\Delta\varepsilon = \left| \varepsilon_{\text{data}} - \varepsilon_{\text{simulation}} \right| < 0.001 \tag{6.18}$$

Since this difference is small only the loss of a single hit is sufficiently likely to change the event selection. The effect of a lower efficiency in data is assessed by giving each track with exactly 18 vertical clusters in TPC 2 a weight of 1 - $\Delta\varepsilon$ = 0.999, and every other track a weight of 1.0. Each event is then given a weight from the product of its two tracks' weights, and the resulting shift in the value of τ calculated. The effect on τ of an increase in efficiency is assumed to be symmetric to that from a decrease, allowing the calculated shift to be taken as the systematic uncertainty resulting from the TPC track quality cut: $\sigma_\tau^{\text{QUALITY}} = 0.00004$.

6.10.3.5. Out of Fiducial Volume Backgrounds

There are broadly three sources of backgrounds originating outside of the fiducial volume (OOFV): cosmic ray muons, "sand muons" from interactions upstream of ND280, and interactions within ND280 but outside the fiducial volume.

The ν_μ Inclusive analysis estimated that they would select 3 events from cosmic rays over T2K Runs 1-3 (0.02 % of their events). Since it is highly unlikely that these events could also produce a track meeting the requirements of the pion

candidate, and pass the subsequent analysis cuts, no systematic was assigned due to cosmic ray backgrounds.

Interactions of beam neutrinos upstream in the sand surrounding the ND280 facility are not included in the standard ND280 beam simulation but are simulated in a standalone production. Applying the coherent pion selection to this sample, equivalent to 12×10^{20} POT, resulted in zero events being selected, so no systematic uncertainty was applied due to sand muon backgrounds.

The only remaining source of OOFV backgrounds are those from interactions elsewhere in ND280, which make up just 2 % of the simulated events selected. These events fall into three categories: interactions in the FGD 1 scintillator bounding the fiducial volume (32 %), interactions in the Tracker dead-material (26 %) and interactions outside the tracker (42 %).

The uncertainty in the rate of these backgrounds coming from interaction and flux simulations has already been taken into account. This leaves two possible sources of systematic differences: differences in the mass of the regions in which the interactions take place, and differences in the reconstruction effects which allowed them into the selection.

A study conducted for the ν_μ Inclusive analysis concluded that no additional reconstruction uncertainty for OOFV backgrounds in the FGD 1 scintillator or Tracker dead-material need be considered beyond those already dealt with. Interactions from outside the Tracker however, which likely entered FGD 1 at high-angle, were assigned a 45 % reconstruction uncertainty [89].

The difference in mass between the real and simulated FGD 1 scintillator is 0.009 %, while the difference in mass of the entire detector is 0.67 % [70]. The former is therefore taken as the uncertainty on FGD 1 scintillator OOFV background, and the latter is taken as the uncertainty on interactions in the Tracker dead-material.

For the mass uncertainty for interactions outside the Tracker, a value of 10 % is estimated based on the uncertainty in the mass of the ECal detectors. This value originates primarily from the 10 % tolerance on the thickness specified by the supplier of the lead sheets which dominate the total mass of the ECals. From my work writing the simulation of the ECal detectors, I believe this uncertainty also covers the differences in the ECal's surrounding dead material.

The total uncertainties for the OOFV interactions are then: 0.009 % for interactions in FGD 1 scintillator, 0.67 % for interactions in Tracker dead-material, and 46 % for interactions outside the Tracker (from the sum-in-quadrature of the mass and reconstruction uncertainties).

To assess the effect of OOFV interactions on the value of τ, the analysis was re-run twice for each of the three categories described above, weighting the corresponding interactions up and down according to the uncertainty assigned to them. For each category, the largest of the two resulting shifts in the value of τ is taken to be the uncertainty resulting from that category. Finally, the total OOFV uncertainty is taken from the sum-in-quadrature of the three categories' uncertainties, giving a value of: $\sigma_{\tau}^{\mathrm{OOFV}} = 0.0079$.

It should be noted that the OOFV fraction in the selection is very small - totalling only 31 raw interactions in simulation. As a result the size of the statistical uncertainty in this sample is significant relative to the systematic uncertainty. Any future analysis which had access to greater simulation statistics would therefore want to re-evaluate this systematic. As will be seen in Section 6.10.4 however, such uncertainty is of little consequence for this analysis.

6.10.3.6. Pion Interactions

Another potential systematic difference between data and simulation is in the passage of charged pions through dense matter, such as the scintillator of FGD 1. There is evidence to suggest that the cross-sections for interactions which would prevent a π^+ from leaving FGD 1 are not well simulated by GEANT4, which is used in the ND280 simulation. The interactions which could most directly prevent a π^+ from leaving FGD 1 are absorption (where the pion is captured by a nucleus) and charge exchange (where a nuclear interaction results in the π^+ being replaced by a π^0).

The effect of such a difference on this analysis was determined by adapting a similar study conducted for the ν_μ Inclusive selection [90], which compared the π^+ interaction cross-sections in carbon from GEANT4 with published experimental values (Figure 6.24). The goal is to consider the effect that higher

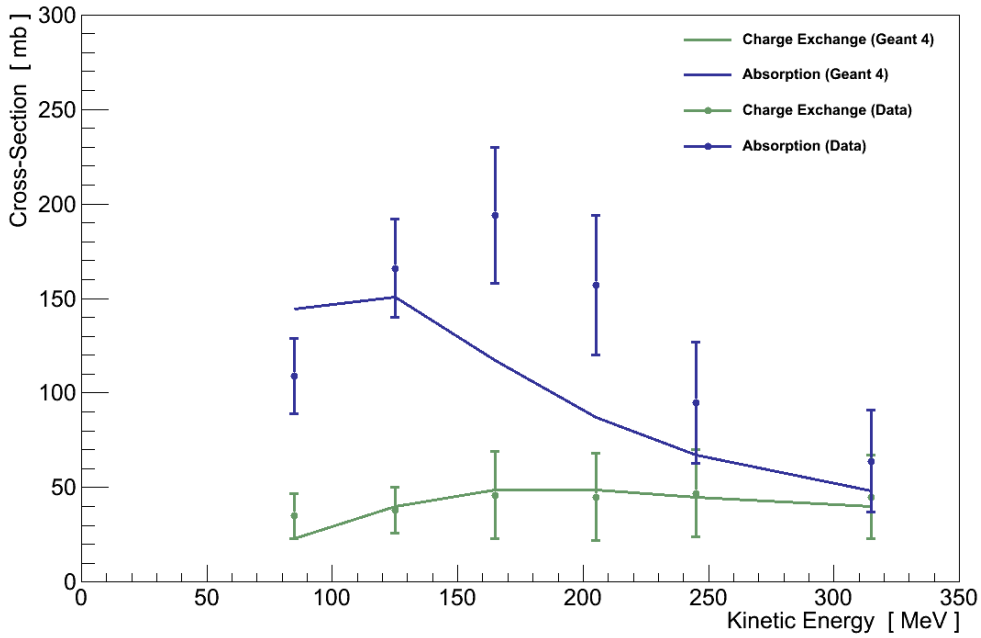

Figure 6.24: Comparison of charge exchange and absorption cross-sections for charged pions in carbon from data and a GEANT4 simulation (from [90]).

or lower cross-sections would have on π^+ which made it into TPC 2 and were selected by this analysis.

First, a sample of π^+ which had the potential to enter TPC 2 and contribute to the analysis was selected by searching events in the ν_μ Inclusive selection for those which meet the following requirements:

1. The number of π^+ made in the simulated interaction was exactly 1
2. A linear extrapolation of the initial direction of the π^+ to the back of FGD 1 indicates it would enter TPC 2.
   (At z = 446.955 mm: |x| ≤ 874.51 mm, |y - 55.0 mm| ≤ 874.51 mm)

Each of these interactions was then classified according to the fate of the π^+:

- Underwent charge-exchange (CE)
- Underwent absorption (ABS)
- Entered TPC 2 (TPC2)
- Other

The method for classifying a pion as undergoing charge exchange or absorption followed that defined in the original pion interactions study [90]. Pions were determined to have entered TPC 2 if they were labelled as having done so by the simulation, and all remaining events were classified as other. This final category contains pions which underwent interactions other than charge exchange or absorption which resulted in them not entering TPC 2, or where the simple linear extrapolation was misleading. All of the selected interactions were then binned in 2D histograms, one for each category, according to the initial kinetic energy of the pion, T^{init}, and its extrapolated distance from TPC 2.

For those events in the charge exchange or absorption categories, the final kinetic energy of the pion, T^{final}, at the point it interacted was also estimated, again following a procedure defined in the original study[2]. Using T^{final} the cross-sections for data and simulation were found by linearly-interpolating the information shown in Figure 6.24. Weights corresponding to taking the simulated cross-section to the top, w_+, and bottom, w_- of the data's uncertainty band were then calculated for these events, and used to fill two additional weighted histograms for each category.

The total number of pions in each T^{init}-distance bin (ij) can be calculated from the un-weighted histograms:

$$N^{ij}_{\mathrm{TOTAL}} = N^{ij}_{\mathrm{TPC2}} + N^{ij}_{\mathrm{ABS}} + N^{ij}_{\mathrm{CE}} + N^{ij}_{\mathrm{OTHER}} \tag{6.19}$$

The total number of pions is constant, and it is assumed that the "other" category is unaffected by changes in the pion cross-sections. Then the re-weighted number of pions in the TPC 2 category can be calculated corresponding to the top, $N_{TPC2,+}$, and bottom, $N_{TPC2,-}$, of the data uncertainty bands using the contents of the weighted charge exchange and absorption histograms, in every bin:

$$N^{ij}_{\mathrm{TPC2},\pm} = N^{ij}_{\mathrm{TOTAL}} - N^{ij}_{\mathrm{ABS},\pm} - N^{ij}_{\mathrm{CE},\pm} - N^{ij}_{\mathrm{OTHER}} \tag{6.20}$$

Finally, weights equivalent to such changes in the pion interaction cross-sections can also be calculated for each bin:

2. Essentially, the Bethe-Bloch formula was used to calculate the energy lost over the distance from creation to absorption/charge exchange.

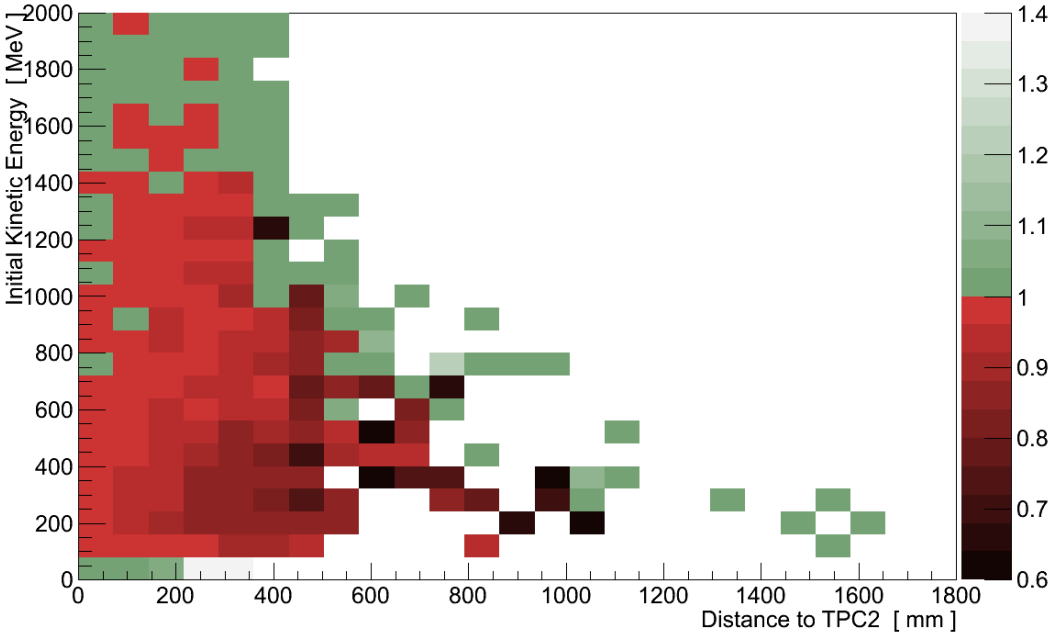

Figure 6.25: The weights calculated corresponding to the top of the data uncertainty bands, as a function of the initial kinetic energy and distance to TPC 2 of the π^+.

$$w^{\mathrm{ij}}_{\mathrm{TPC2},\pm} = \frac{N^{\mathrm{ij}}_{\mathrm{TPC2},\pm}}{N^{\mathrm{ij}}_{\mathrm{TPC2}}} \tag{6.21}$$

An example of the resulting weights, calculated for the top of the data uncertainty band, is shown in Figure 6.25.

Now, the effect on the value of τ can be determined by re-running the analysis twice, once for each of the top/bottom data uncertainty band weights. For every event where the pion candidate track corresponded to a true pion, the event was given the weight calculated in Equation 6.21 for a pion with that $\mathrm{T}^{\mathrm{init}}$-distance. Taking the largest of the two resulting shifts in the value of τ, the uncertainty due to pion interactions was calculated as: $\sigma_\tau{}^{\mathrm{PION}} = 0.039$.

6.10.3.7. Vertex Activity

The final systematic to be considered is that for the vertex activity (VA), which is directly cut on in the analysis (Section 6.7). Differences in the amount

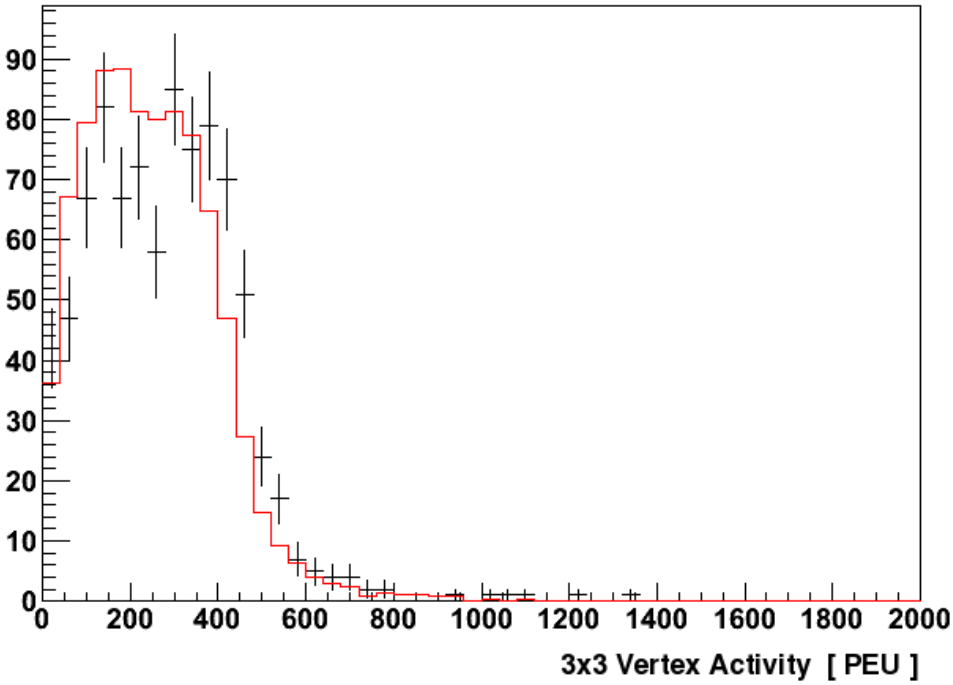

Figure 6.26: The 3×3 vertex activity measured at the end of proton tracks which stop in FGD 1. The red line is simulation, the black crosses are T2K beam data [91].

of energy deposited by particles, or in the response of the detector to a given energy deposition could result in differences in the VA measured.

The FGD group assessed the level of agreement in the energy recorded by FGD 1 for two samples of particles from data and simulation. For muons, which generate relatively low energy hits, the distribution of energies deposited in hits was found to agree within 3 %. For stopping protons, which generate very high energy hits, there was found to be an approximately 10 % shift in the 3×3 vertex activity[3] measured at the end of the track (Figure 6.26) [91].

The 5×5 VA cut of 290 PEU corresponds to an average hit energy between these two extremes. However, since the VA is cut on directly, and the distribution of hit energies could include high fluctuations, the uncertainty assigned to the VA was set to 10 %.

To assess the effect of the VA uncertainty on the value of τ the analysis was re-run twice, once scaling the VA for each event up by 10 %, once scaling it down by 10 %. Each time the value of τ was recalculated, and the largest of

3. Unlike this analysis, which uses a 5×5 region of bars, the stopping protons study used a 3×3 region of bars as the vertex activity.

Source		Uncertainty	
		Absolute	**Fractional**
Flux		0.042	2.9 %
Interactions		0.398	27.8 %
Detector	**Momentum resolution**	0.084	5.8 %
	Momentum scale	0.0069	0.48 %
	FGD-TPC matching	0.0025	0.17 %
	TPC track quality cut	0.00004	0.003 %
	OOFV	0.0079	0.55 %
	Pion interactions	0.039	2.7 %
	VA	0.073	5.1 %
Total		0.42	29.1 %

Table 6.10: Summary of the systematic uncertainties expressed as absolute deviations from the nominal value $\tau = 1.43$, and as a percentage.

the two resulting shifts was taken as the uncertainty due to the VA: $\sigma_\tau^{\text{VA}} = 0.073$.

6.10.4. Summary

Table 6.10 shows a summary of all the systematic uncertainties considered. The individual absolute uncertainties were combined via a sum in quadrature to conclude that there is a total 29 % systematic uncertainty: $\tau = 1.43 \pm 0.42$.

6.11. Results

Figure 6.27 shows the $|t|$ distribution for events selected in data and simulation. In the signal region, $|t| < 0.09\,\text{GeV}^2$, there are 53 events in data,

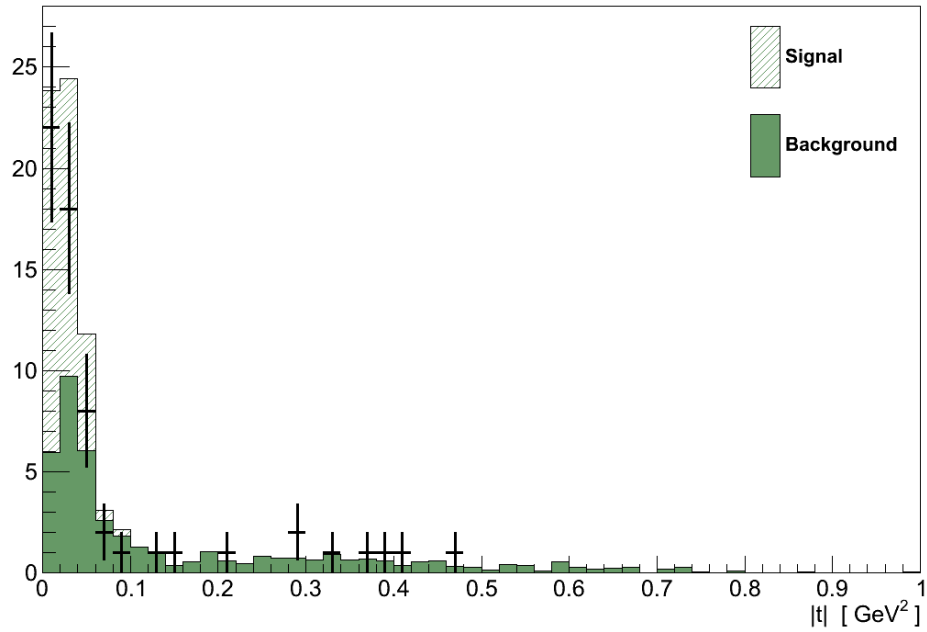

Figure 6.27: Final |t| distribution.

Data	**Signal region, n_D**	53
	Control region, m_D	12
Simulation	**Signal region, s**	39.0
	Signal region, b	25.3
	Control region, b / $\tau_{nominal}$	17.6
	$\tau_{nominal}$	1.43 ± 0.42

Table 6.11: Inputs to the result calculations from data and simulation.

compared with a prediction of only 25.3 background events from simulation. In the control region there are 12 data events, compared with 17.6 in simulation.

The event numbers in the two regions from data and simulation are summarised in Table 6.11. It is these numbers which are input into the result calculations.

The first calculation is a comparison of the data to the "background-only hypothesis", the assumption that there is no coherent signal ($\mu = 0$) and only

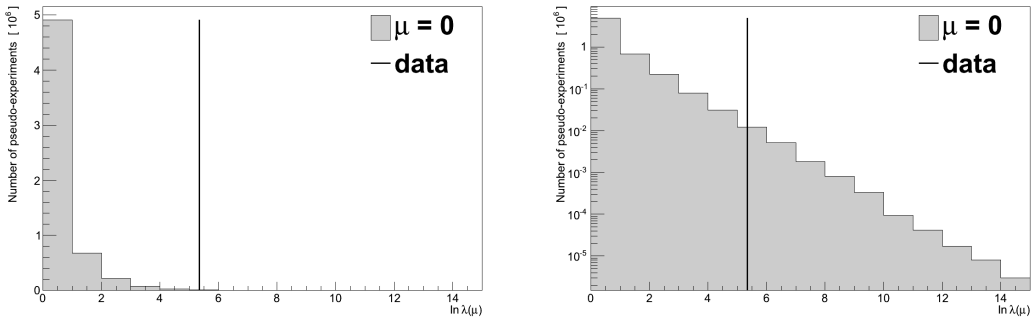

Figure 6.28: Test of the background-only hypothesis showing the expected $\ln\lambda(\mu = 0)$ distribution (histogram) compared with the value measured in data (vertical line). (left) Shown on a linear scale the data is clearly extreme compared to the expected distribution. (right) Shown on a log-scale, sufficient statistics were used to fill-out the tail and provide a valid P-value.

background events. A sample of 10 million pseudo-experiments were generated to find the maximised log-likelihood ratio distribution, which is shown in Figure 6.28 compared with the maximised log-likelihood ratio of the data: $\ln\lambda(0) = 5.35$.

In 13371 pseudo-experiments the value of $\ln\lambda(0)$ was ≥ 5.35, giving the data a P-value of 0.00134. Converted to a significance, that corresponds to a $3.003\,\sigma$ excess.

The stringent limits set on the existence of ν_μ CC coherent pion production by SciBooNE motivated this analysis to be conducted as a search rather than a measurement. None the less, faced with such a significant excess it is interesting to explore what this result says if considered as a signal from coherent pion production.

As discussed in Chapter 4, it is widely believed that an alternative to the Rein-Sehgal model will be required to successfully describe coherent pion production at these low neutrino energies. However its implementation in the GENIE simulation used in this analysis, and its wide use in other analyses, provide a good baseline with which to interpret the data.

The maximised likelihood, $L(\mu',\tau',b')$, found in the result calculation gives the values of μ and τ which best describe the data, i.e the best-fit signal-strength[4]. For the GENIE simulation this is found at $\mu' = 0.92\ ^{+0.34}_{-0.36}$. In other words, the

4. The uncertainties on this value come from statistics and τ. They do not include systematic uncertainties on the signal efficiency.

Rein-Sehgal model in GENIE would best describe the data if its cross-section were 92 % of the default.

For a cross-section $\sigma(E_\nu)$ and flux $\Phi(E_\nu)$, the flux-averaged cross-section is defined:

$$\langle\sigma\rangle = \frac{\int \Phi\left(E_\nu\right)\ \sigma\left(E_\nu\right)\ \mathrm{dE}_\nu}{\int \Phi\left(E_\nu\right)\ \mathrm{dE}_\nu} \tag{6.22}$$

Applying the best-fit signal-strength to the GENIE Rein-Sehgal model averaged over the ν_μ flux at ND280 gives a flux-averaged cross-section:

$$\langle\sigma\rangle = 0.060^{+0.022}_{-0.023} \times 10^{-38}\mathrm{cm}^2 \tag{6.23}$$

For reference, this measurement was made on a predominantly carbon target with $A^{\text{effective}} = 12.10$ (Section 5.4.2), in a ν_μ beam with mean energy 0.856 GeV, and where 68 % of the total ν_μ flux is found within 0.475 GeV of that mean.

Figure 6.29 shows this result compared with the limits set by SciBooNE, along with the default Rein-Sehgal cross-section in GENIE.

6.11.1. Comparison with the Alvarez-Ruso model

The analysis was re-run using the Alvarez-Ruso model implemented in GENIE. Recalling Section 6.2, this sample used the same background events from the standard GENIE simulation, and all cut values were left the same. Its purpose being to assess how dependent the analysis is on the coherent model used.

Table 6.12 shows the effect on signal events of the various selections and cuts in the analysis, compared between the Rein-Sehgal and Alvarez-Ruso models. The efficiencies from the two models are very similar at every stage of the analysis and, most importantly, differ by just 1 percentage point at the final selection. This is consistent with the analysis goal of being as model independent as possible.

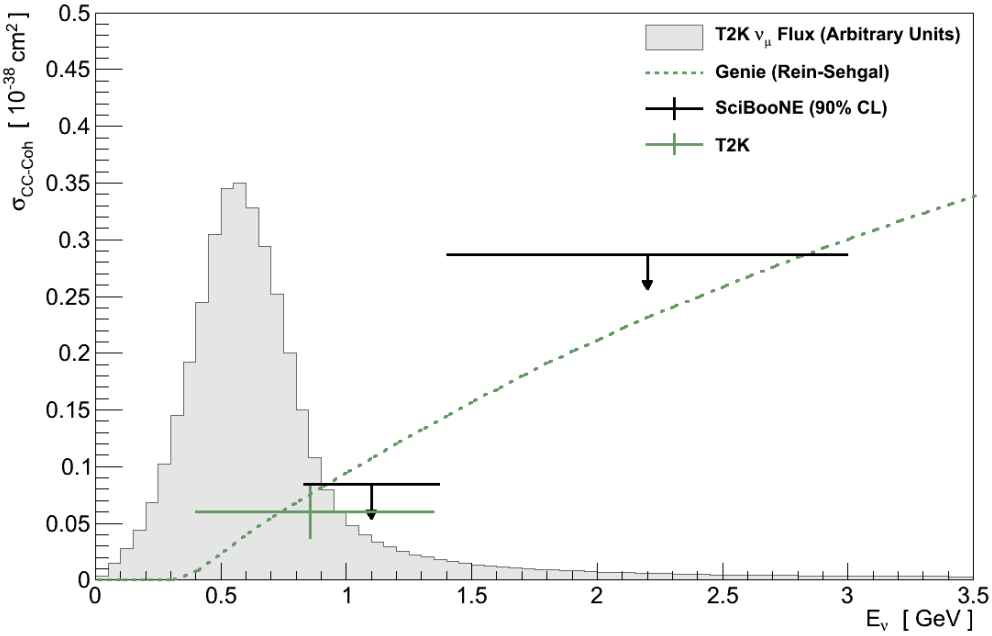

Figure 6.29: The flux-averaged ν_μ CC coherent pion cross-section measured in T2K using the GENIE Rein-Sehgal model. The default GENIE Rein-Sehgal cross-section and limits from SciBooNE are shown for comparison. Horizontally the T2K point is placed at the flux's mean energy, and the width is a symmetric region containing 68 % of the total. The ND280 ν_μ flux is shown in grey.

Step	Data	Rein-Sehgal			Alvarez-Ruso		
		Total	Signal	Efficiency	Total	Signal	Efficiency
ν_μ Inclusive selection	10303	10016	96	78 %	9983	63	74 %
Coherent Initial selection	620	704	52	42 %	689	38	44 %
p_T cut	122	169	43	35 %	156	30	35 %
VA cut	65	81	39	32 %	71	28	33 %

Table 6.12: Total and signal events passing through each stage in the selection, compared between Rein-Sehgal and Alvarez-Ruso.

Figure 6.30 shows the distributions on which the two cuts are placed. For the transverse momentum distribution (cf. Figure 6.13) the Alvarez-Ruso model predicts a very simlar distribution to Rein-Sehgal model, after accounting for the overall difference in normalisation. The vertex activity distribution (cf. Figure 6.15) is also very similar between the two models. This is to be

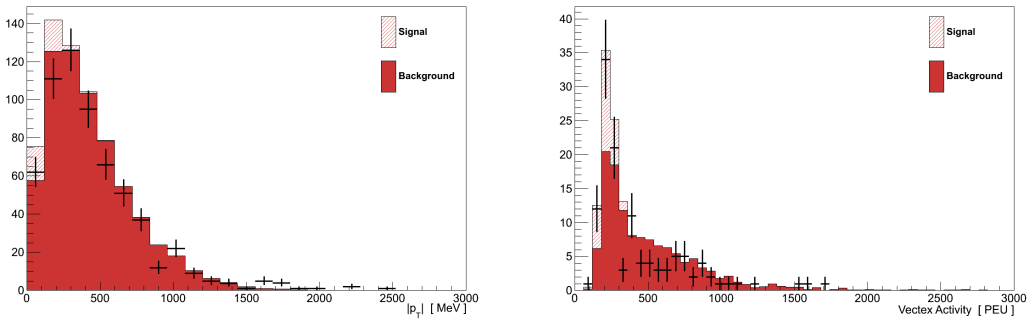

Figure 6.30: Cut distributions predicted using the Alvarez-Ruso simulation. (left) The p_T distribution, events above 180 MeV are rejected. (right) The VA distribution, events above 190 PEU are rejected.

expected since the VA measured for coherent events is mostly independent on the kinematics of the muon and pion created.

The kinematics of the muon and pion candidates from the final selection are shown in Figure 6.31 (cf. Figure 6.16). The angular plots show the Alvarez-Ruso model's preference for more forward-going topologies, though the difference in this flux-integrated distribution is more slight than the comparison at fixed energy in Section 4.3. The pion momentum spectrum is also noticable softer, with fewer events exceeding 1000 MeV than for Rein-Sehgal. Comparing the four plots in Figure 6.31 and Figure 6.16, neither model is consistently the better at describing the data. Given also the degree of uncertainty on the background events lying underneath, no statement can be made on which model is preferred.

The |t| distribution of the Alvarez-Ruso model shown in Figure 6.32 (cf. Figure 6.27), again shows its slight preference for a more forward-going topology. However, because this difference moves events further from the cut value, it does not adversely affect the analysis.

Since the background events in this simulation are identical to those in the standard GENIE simulation, there is no need to repeat the search for an excess. In fact the only fit parameter that differs from the standard GENIE simulation is the signal prediction, s = 27.8. Calculating the best-fit signal strength, $\mu_{\mathrm{AR}} = 1.28^{+0.48}_{-0.51}$, which gives a best-fit flux-averaged cross-section of[5]:

5. Please note that the model used here is not identical to the authors' full model (see Section 4.3).

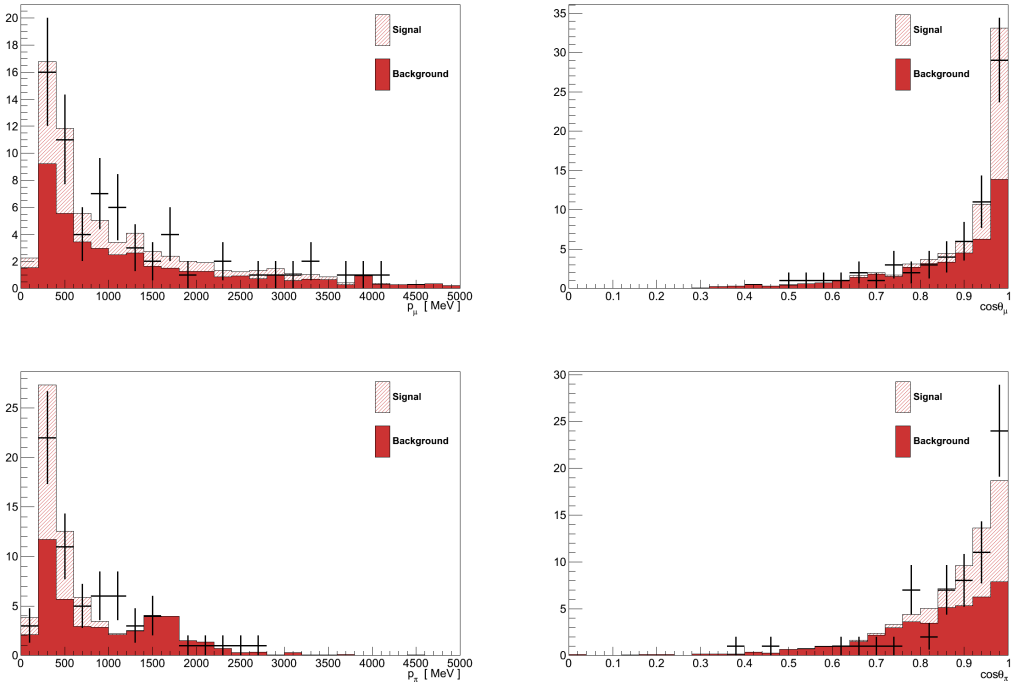

Figure 6.31: Final-state kinematics predicted by the Alvarez-Ruso simulation. (top) Muon candidate track. (bottom) Pion candidate track. (left) Momentum. (right) Angle with respect to the incoming neutrinos.

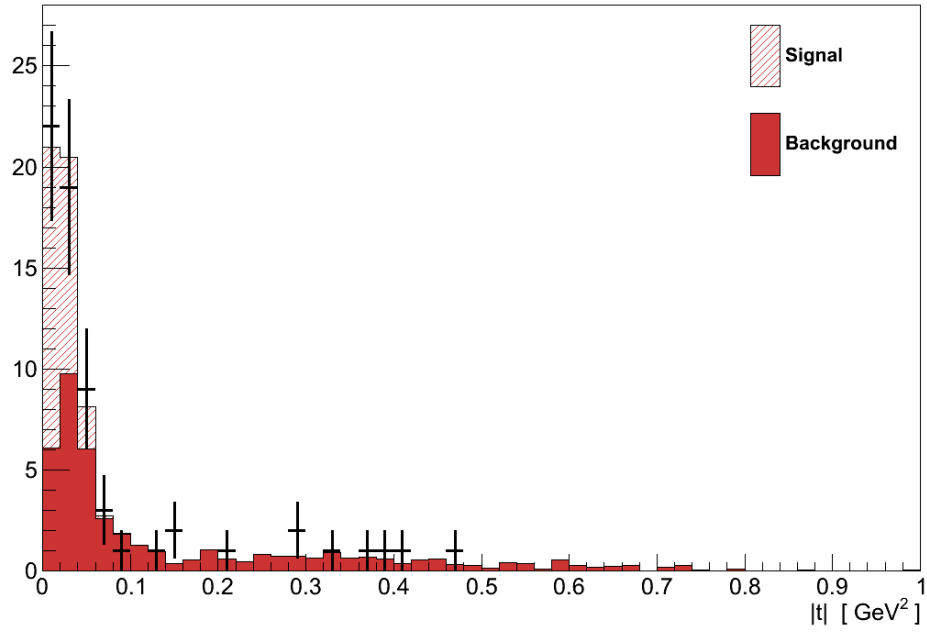

Figure 6.32: The |t| distribution of events in the final selection from the Alvarez-Ruso simulation.

$$\langle\sigma\rangle = 0.058^{+0.022}_{-0.023} \times 10^{-38}\text{cm}^2 \tag{6.24}$$

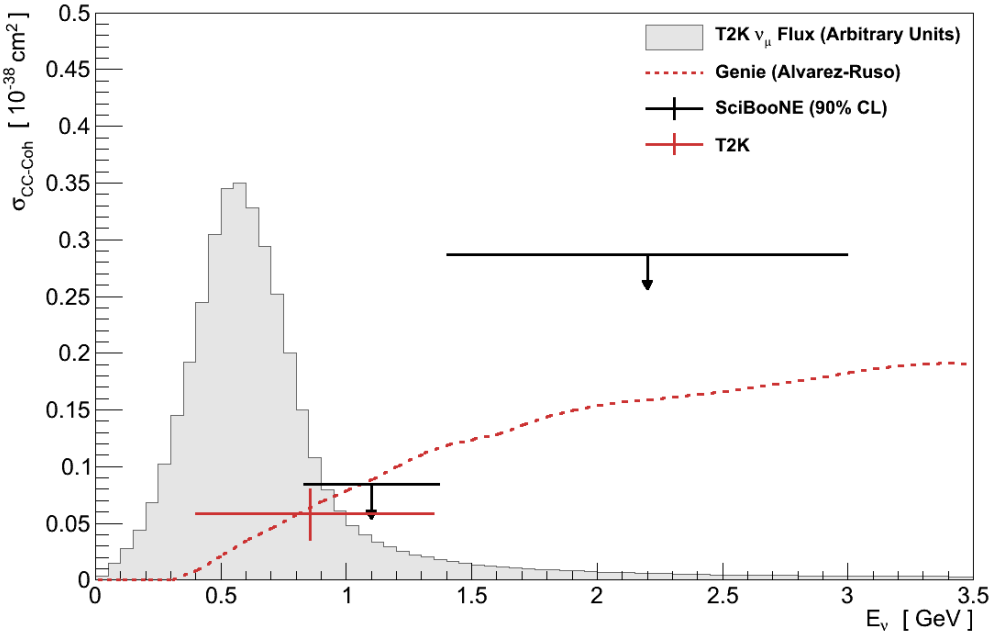

Figure 6.33: The flux-averaged ν_μ CC coherent pion cross-section measured in T2K using the GENIE Alvarez-Ruso model. The default GENIE Alvarez-Ruso cross-section and limits from SciBooNE are shown for comparison. Horizontally the T2K point is placed at the flux's mean energy, and the width is a symmetric region containing 68 %of the total. The ND280 ν_μ flux is shown in grey.

This best-fit signal strength is in remarkable agreement with the data, though considering the size of the uncertainty on it no strong conclusion can be drawn from it. The best-fit fluz-averaged cross-section is compared with the default Alvarez-Ruso cross-section and SciBooNE limits in Figure 6.33.

6.11.2. Comparison with NEUT

The analysis was also re-run using the NEUT simulation generated as part of the production 5 processing. Since the Rein-Sehgal model in NEUT is quite dated the motivation for reviewing it is its relevance for other ND280 analysers who use NEUT as their primary simulation, and its alternative background model.

Table 6.13 shows the number of total and background events at each stage in the analysis, compared between GENIE and NEUT. It is clear that NEUT predicts quite different background numbers compared to GENIE. Although

Step	Data	GENIE			NEUT		
		Total	Background	Purity	Total	Background	Purity
ν_μ **Inclusive selection**	10303	10016	9920	1.0 %	10797	10472	3.0 %
Coherent Initial selection	620	704	652	7.4 %	631	500	20.7 %
p_T **cut**	122	169	126	25.3 %	159	76	52.2 %
VA cut	65	81	42	47.8 %	98	23	77.0 %

Table 6.13: Total and background events passing through each stage in the selection, compared between GENIE and NEUT.

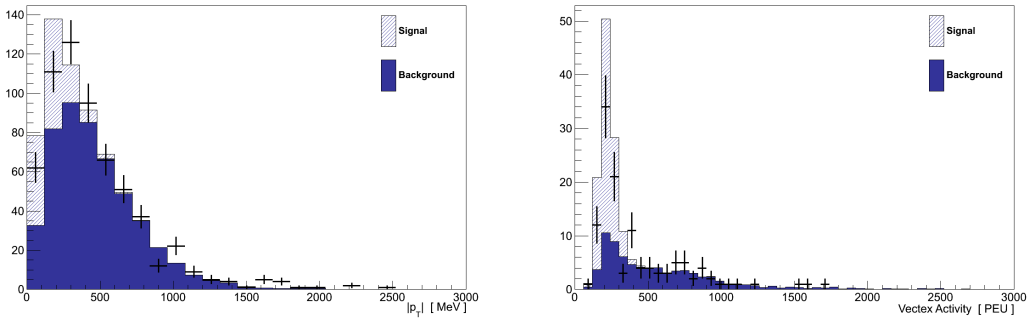

Figure 6.34: Cut distributions predicted by the NEUT simulation. (left) The p_T distribution, events above 180 MeV are rejected. (right) The VA distribution, events above 190 PEU are rejected.

its total event prediction agrees better with data early on, that trend is gradually reversed as the selection focuses on the final coherent selection.

Figure 6.34 shows the NEUT predictions of the distributions which are cut on, as for the Alvarez-Ruso re-run the cut positions were unaltered. For the transverse momentum (cf. Figure 6.13) both GENIE and NEUT reproduce well the high-p_T tail which is rejected, but neither provide good agreement at the low end (either with or without the signal). For the vertex activity (cf. Figure 6.15) NEUT arguably gives better agreement for the high VA tail which is rejected, but predicts a much smaller background component in the low-VA peak than GENIE.

The angle and momentum distributions of the muon and pion tracks which made it to the final selection from NEUT are shown in Figure 6.35 (cf. Figure 6.16). In contrast with GENIE the kinematic distributions from

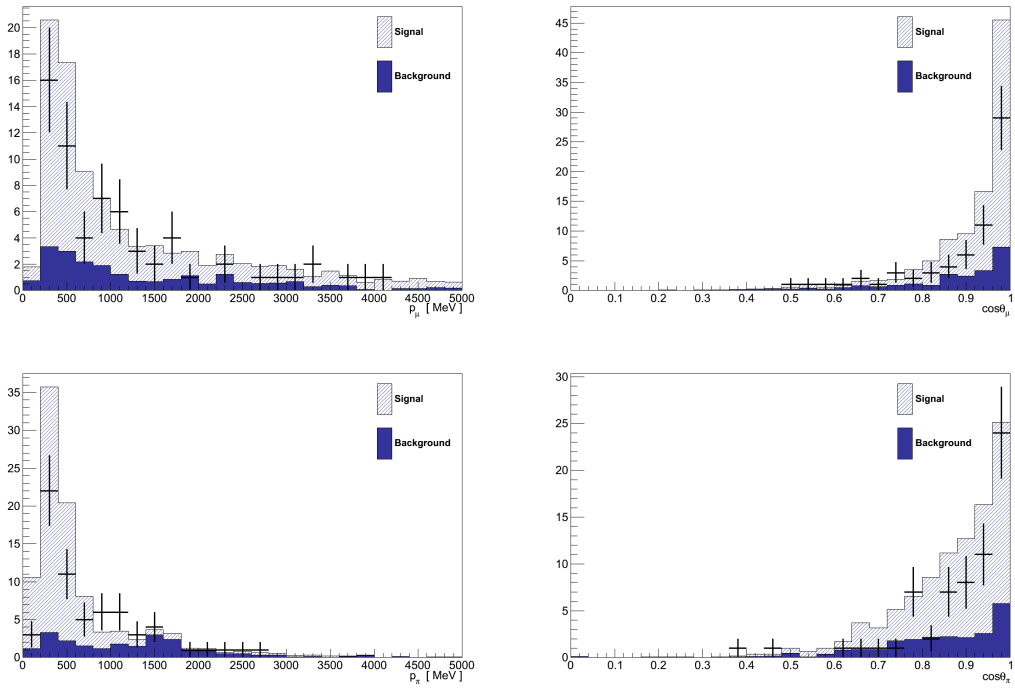

Figure 6.35: Final-state kinematics predicted by the NEUT simulation. (top) Muon candidate track. (bottom) Pion candidate track. (left) Momentum. (right) Angle with respect to the incoming neutrinos.

backgrounds in NEUT are much flatter, and it is clear that they are unlikely to be sufficient to describe the data.

Finally, the |t| distribution of the selected events is shown in Figure 6.36 with a substantially lower background predicted in the signal region compared with GENIE (cf. Figure 6.27). If this were the primary analysis it may have been concluded that simply cutting on |t| and performing a straight counting experiment would suffice, rather than bothering to constrain the minimal background in the signal region.

The inputs to the result calculation from the NEUT simulation are shown in Table 6.14. No attempt was made to re-assess the flux or detector systematic uncertainties for NEUT, since this is only a cross-check of the primary analysis. However the interaction systematics were re-evaluated, again using T2KReWeight but this time applying the parameters and uncertainties determined for NEUT by the Neutrino Interactions Working Group for use in the official oscillation analyses [92]. This procedure determined the uncertainty on τ due to interactions was 63.9 % (again dominated by M_A in CC QE interactions). Combining this with the detector and flux uncertainties determined previously gives a total uncertainty on τ of 64.5 %.

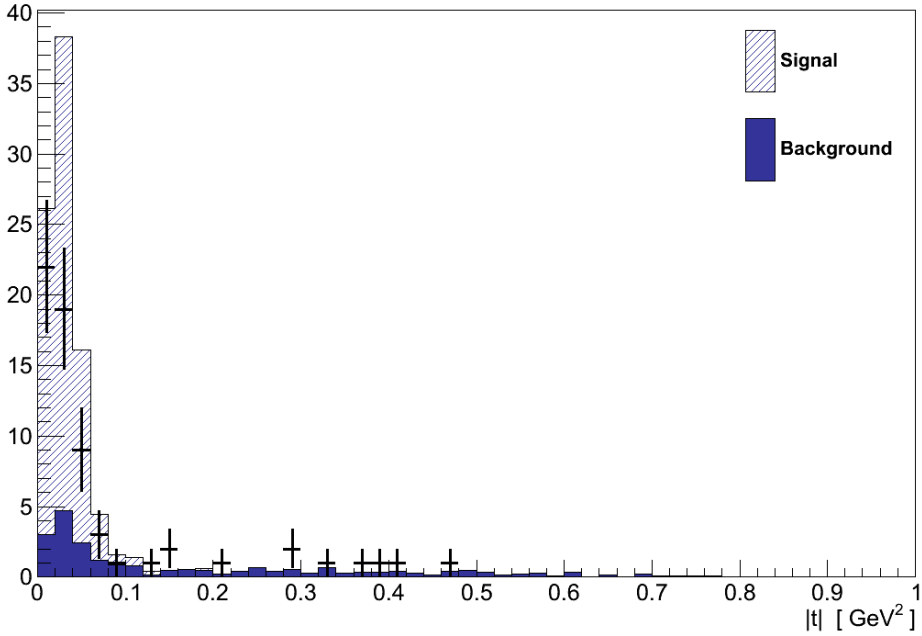

Figure 6.36: The |t| distribution of events in the final selection from the NEUT simulation.

Data	**Signal region, n_D**	53
	Control region, m_D	12
NEUT Simulation	**Signal region, s**	74.2
	Signal region, b	11.7
	Control region, b / $\tau_{nominal}$	12.0
	$\tau_{nominal}$	0.975 ± 0.629

Table 6.14: Inputs to the result calculations from the NEUT simulation.

To compare the data to the background-only hypothesis from NEUT, 10 million pseudo-experiments were generated with $\mu = 0$, and compared with the data value for $\ln \lambda(0) = 6.28$ (Figure 6.37). In 8301 pseudo-experiments the value of $\ln \lambda(0)$ was ≥ 6.28, giving the data a P-value of 0.0083. Converted to a significance, that corresponds to a $3.15\,\sigma$ excess showing, like GENIE, a clear signal despite the larger systematic uncertainty.

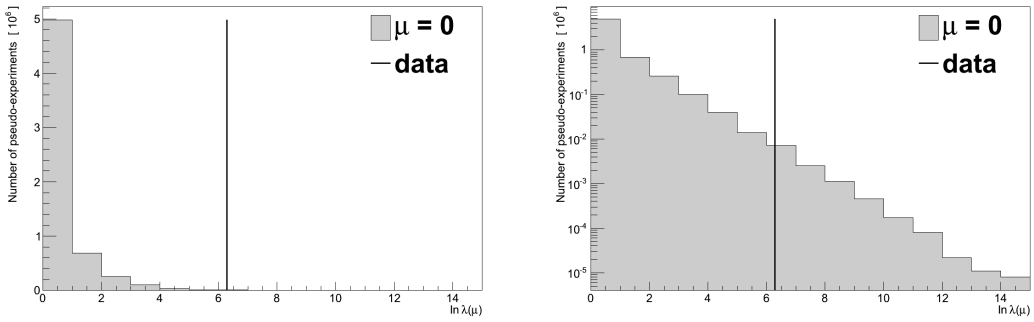

Figure 6.37: Test of the background-only hypothesis showing the expected $\ln\lambda(\mu = 0)$ distribution (histogram) compared with the value measured in data (vertical line). (left) Shown on a linear scale the data is clearly extreme compared to the expected distribution. (right) Shown on a log-scale none of the 10 million pseudo-experiments were close to the data value.

It is also possible to find the best-fit signal strength for the NEUT Rein-Sehgal coherent model, which is found to be $\mu = 0.56^{+0.18}_{-0.19}$. This corresponds to a flux averaged cross-section of:

$$\langle\sigma\rangle = 0.091^{+0.030}_{-0.031} \times 10^{-38}\text{cm}^2 \tag{6.25}$$

which is somewhat higher than the values from the GENIE Rein-Sehgal and Alvarez-Ruso models as a result of the much lower background prediction. It is compared with the default NEUT Rein-Sehgal cross-section and SciBooNE limits in Figure 6.38.

6.12. Summary

This search has found a $3.0\,\sigma$ excess of events above the background prediction which, in the conventional parlance of particle physics, constitutes evidence of CC coherent pion production at T2K. Measured at a mean neutrino energy of 0.856 GeV, this is also the first experimental evidence of the process below 7 GeV.

The analysis was developed in the context of the Rein-Sehgal model in GENIE, but comparisons using the Alvarez-Ruso model and the NEUT simulation both add credance to this claim. The NEUT simulation, which represents the best available alternative description for background processes, suggested

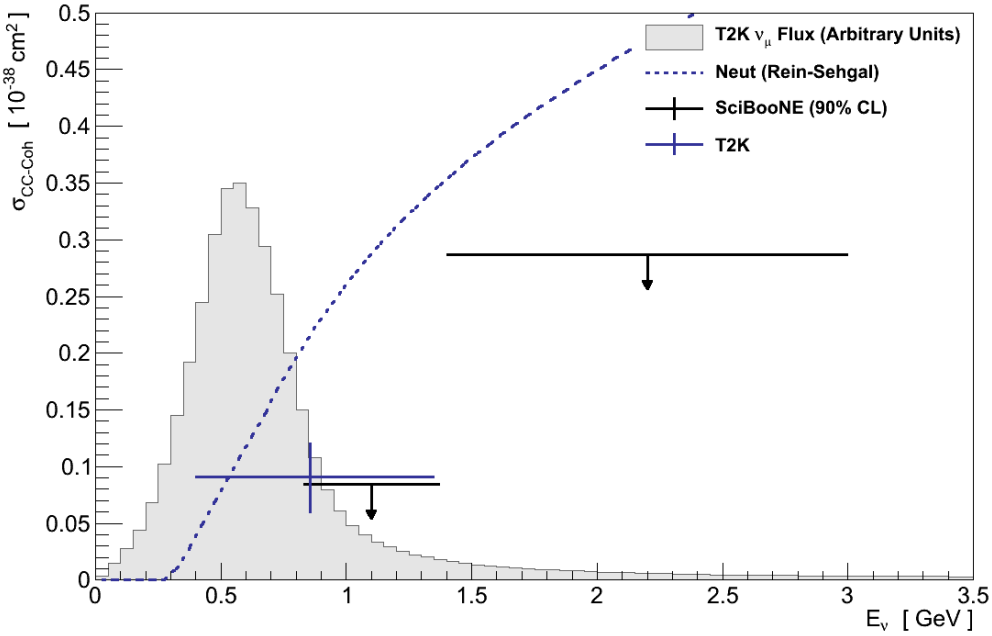

Figure 6.38: The flux-averaged ν_μ CC coherent pion cross-section measured in T2K using the NEUT Rein-Sehgal model. The default NEUT Rein-Sehgal cross-section and limits from SciBooNE are shown for comparison. Horizontally the T2K point is placed at the flux's mean energy, and the width is a symmetric region containing 68 % of the total. The ND280 ν_μ flux is shown in grey.

that if anything the background in the analysis is lower than that predicted by GENIE. While the Alvarez-Ruso model, which represents an alternative possible description of coherent pion production, resulted in very little change in the efficiency of the analysis, implying it is reasonably independent of the signal model used. Unfortunately, the statistical uncertainty in the data and systematic uncertainty in the background simulation prevent any statement on which model is preferred by the data.

The significance of the excess observed is the primary result of this analysis, however it is difficult to interpret this result in a wider context without making some attempt to infer a cross-section. The Rein-Sehgal model in GENIE was found to best describe the data when scaled to 92 % of its default value. The Rein-Sehgal model's compatibility with data at higher neutrino energies would be degraded by such a scaling, supporting the widely held belief from NC coherent pion measurements that it is inappropriate for describing low energy coherent pion production.

Scaling the GENIE Rein-Sehgal model by this factor gives a cross-section, averaged over the ND280 flux, of $0.060 \times 10^{-38}\,\mathrm{cm}^2$. As can be seen in

Figure 6.29, this is compatible with the 90 % CL limits set by SciBooNE, though the validity of any such comparison is limited by the fact that the two analyses used very different simulations for both signal and backgrounds.

Such a clear and interesting coherent pion signal should motivate further future analysis within T2K. Future analyses can immediately take advantage of additional data accumulated by ND280 since, which doubles that used here. However the analysis would most greatly benefit from further work to better constrain the backgrounds, the systematic uncertainty on which currently obscures move detailed investigation.

7. Conclusions

It is likely that the investigation of neutrinos, particularly through the phenomenon of neutrino oscillations, can provide vital clues to the future development of particle physics. However such investigations are limited by the precision with which neutrino interactions with nuclei are understood. One such interaction, neutrino induced coherent pion production, is of particular importance as a potential source of background to ν_e oscillation searches, and as part of the broader goal of understanding neutrino induced pion production in general.

A review of experimental data on coherent pion production was presented, noting in particular the reduced NC and lack of evidence for CC cross-sections recently measured below 3 GeV, in conflict with the Rein-Sehgal model which explained well data at higher energies. Investigation of the Rein-Sehgal model found that its predictions vary greatly depending on the choice of inputs, but also that its validity at low energy is questionable. One alternative low energy model, the Alvarez-Ruso model, was therefore implemented in the GENIE interaction simulation for the purposes of comparison. This implementation represents the first time a "microscopic" coherent model has been included in a full neutrino interaction simulation.

A search for coherent pion production was conducted using data gathered from the T2K experiment's near detector, ND280, and predictions from the GENIE interaction simulation. This analysis found a 3.0σ excess of events over the background expectation, constituting the first experimental evidence of ν_μ CC coherent pion production below 7 GeV. The analysis was repeated using alternative signal (Alvarez-Ruso) and background (NEUT) models, both of which supported this conclusion.

In order to put this result in context of those from other experiments, it was found that the size of the excess seen in data is compatible with a flux-averaged cross-section which is 92 % of that predicted by the Rein-Sehgal model in GENIE. This is compatible with other comparable data, in particular that from SciBooNE (Figure 7.1).

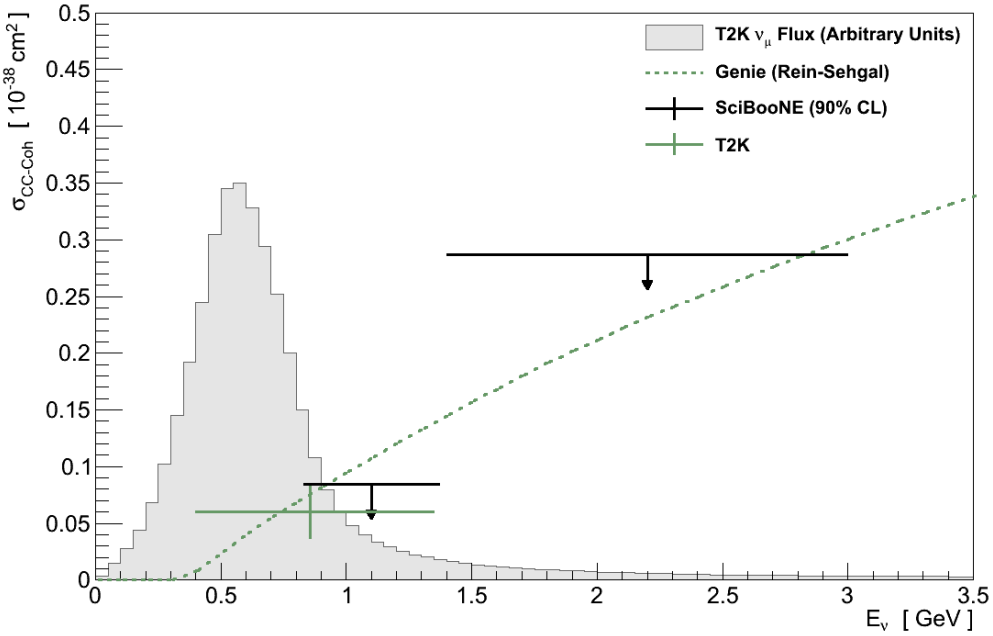

Figure 7.1: The flux-averaged ν_μ CC coherent pion cross-section measured in T2K using the GENIE Rein-Sehgal model.

The primary goal for improving understanding of coherent pion production must be the identification of a model which can better explain the process at low energies, but the uncertainties in this analysis are not yet low enough to allow discrimination between the signal models used. However, the strong evidence found here should motivate continued investigation in T2K which, with improved statistics and reduced background systematic uncertainties, should be capable of constraining the available models. In combination with similar searches at other experiments, this goal should be attainable in the near future.

References

1. The ATLAS Collaboration
   Observation of a new particle in the search for the Standard Model Higgs boson with the ATLAS detector at the LHC
   Physics Letters B, Volume 716, p1-29, 2012

2. The CMS Collaboration
   Observation of a new boson at a mass of 125 GeV with the CMS experiment at the LHC
   Physics Letters B, Volume 716, p30-61, 2012

3. A.D. Sakharov
   Violation of CP invariance, C asymmetry, and baryon asymmetry of the universe
   Soviet Physics Uspekhi, Volume 34, p392, 1991

4. The Particle Data Group
   Review of Particle Physics - CP Violation in Meson Decays
   Physical Review D, Volume 86, p166-176, 2012

5. A. Riotto
   Baryogenesis and Leptogenesis
   Journal of Physics: Conference Series, Volume 335, p012008, 2011

6. C.L. Cowan, F. Reines et al.
   Detection of the Free Neutrino: A Confirmation
   Science, Volume 124, p103-104, 1956

7. The Particle Data Group
   Review of Particle Physics - Neutrino Mass, Mixing and Oscillations
   Physical Review D, Volume 86, p177-198, 2012

8. B. Pontecorvo
   Neutrino Experiments and the Problem of Conservation of Leptonic Charge
   Journal of Experimental and Theoretical Physics, Volume 26, p984, 1968

9. Z. Maki, M. Nakagawa, and S. Sakata
   Remarks on the Unified Model of Elementary Particles
   Progress of Theoretical Physics, Volume 28, p870-880, 1962

10. B. Kayser
    On the quantum mechanics of neutrino oscillation
    Physical Review D, Volume 24, p110-116, 1981

11. The ALEPH, DELPHI, L3, OPAL and SLD Collaborations, the LEP Electroweak Working Group, and The SLD Electroweak and Heavy Flavour Groups
Precision electroweak measurements on the Z resonance
Physics Reviews, Volume 427, p257-454, 2006

12. V.N. Aseev et al.
Upper limit on the electron antineutrino mass from the Troitsk experiment
Physical Review D, Volume 84, p112003, 2011

13. D. Griffiths
Introduction to Elementary Particles
Second Edition, Wiley-VCH

14. The Particle Data Group
Review of Particle Physics - Physical Constants
Physical Review D, Volume 86, p107, 2012

15. M. Goldhaber et al.
Helicity of Neutrinos
Physical Review, Volume 109, p1015-1017, 1958

16. J.A. Formaggio and G.P. Zeller
From eV to EeV: Neutrino cross sections across energy scales
Reviews of Modern Physics, Volume 84, p1307-1341, 2012

17. E. Fermi
Versuch einer Theorie der β-Strahlen
Zeitschrift für Physik, Volume 88, p161-177, 1934

18. A. Tsapalis
Nucleon And Pion-Nucleon Form-Factors From Lattice QCD
Proceedings of the 11th International Conference on Meson-Nucleon Physics and the Structure of the Nucleon, Volume 1, 2007

19. M. Day, K.S. McFarland
Differences in Quasi-Elastic Cross-Sections of Muon and Electron Neutrinos
Physical Review D, Volume 86, p053003, 2012

20. A. Bodek et al.
Extraction of the Axial Nucleon Form Factor from Neutrino Experiments on Deuterium
Journal of Physics: Conference Series, Volume 110, p082004, 2008

21. C.H. Llewellyn-Smith
Neutrino reactions at accelerator energies
Physics Reports, Volume 3, p261-379, 1972

22. D. Rein and L.M. Sehgal
Neutrino-Excitation of Baryon Resonances and Single Pion Production
Annals of Physics, Volume 133, p79-153, 1981

23. R.A. Smith and E.J.Moniz
Neutrino reactions on nuclear targets
Nuclear Physics B, Volume 43, p605-622, 1972

24. A. Bodek and J.L. Ritchie
Further studies of Fermi-motion effects in lepton scattering from nuclear targets
Physical Review D, Volume 24, p1400-1402, 1981

25. O. Benhar et al.
Spectral function of finite nuclei and scattering of GeV electrons
Nuclear Physics A, Volume 579, p493-517, 1994

26. The MiniBooNE collaboration
First Measurement of the Muon Neutrino Charged Current Quasielastic Double Differential Cross Section
Physical Review D, Volume 81, p092005, 2010

27. J. Nieves et al.
The nucleon axial mass and the MiniBooNE Quasielastic Neutrino-Nucleus Scattering problem
Physics Letters B, Volume 707, p72-75, 2012

28. H. Gallagher
The NEUGEN neutrino event generator
Nuclear Physics B - Proceedings Supplements, Volume 112, p188-194, 2002

29. D. Casper
The nuance neutrino physics simulation, and the future
Nuclear Physics B - Proceedings Supplements, Volume 1-3, p161-170, 2002

30. Y. Hayato
Neut
Nuclear Physics B - Proceedings Supplements, Volume 1-3, p171-176, 2002

31. C. Andreopoulos et al.
The GENIE Neutrino Monte Carlo Generator
NIM A, Volume 614, p87-104, 2010

32. J.T. Sobczyk et al.
Effects of final-state interactions in neutrino-nucleus interactions
Physical Review C, Volume 86, p015505, 2012

33. U. Mosel et al.
Transport-theoretical description of nuclear reactions
Physics Reports, Volume 512, p1-124, 2012

34. The Aachen-Padova Experiment
Observation of Neutrino and Antineutrino induced coherent neutral pion production off Al^{27}
Physics Letters B, Volume 125, p230-236, 1983

35. K.S. Lackner
Coherent Meson Production as a Test for Neutral Weak Currents of Exotic Space-Time Structure
Nuclear Physics B, Volume 153, p526-545, 1979

36. D. Rein and L.M. Sehgal
Coherent π^0 Production in Neutrino Reactions
Nuclear Physics B, Volume 223, p29-44, 1983

37. E. Isikal, D. Rein and J.G. Morfin
Evidence for Neutrino- and Antineutrino-induced Coherent π^0 Production
Physical Review Letters, Volume 52, p1096-1099, 1984

38. BEBC WA59 Collaboration
Coherent Single Pion Production by Antineutrino Charged Current Interactions and Test of PCAC
Zeitschrift fur Physik C, Volume 31, p191-197, 1986

39. The CHARM II Collaboration
Coherent Single Charged Pion Production by Neutrinos
Physics Letters B, Volume 313, p267-275, 1993

40. The CHARM Collaboration
Measurement of the cross section of coherent π^0 production by muon-neutrino and antineutrino neutral-current interactions on nuclei
Physics Letters B, Volume 157, p469-474, 1985

41. The SKAT Collaboration
Coherent Pion Production in Neutrino and Antineutrino Interactions on Nuclei of Heavy Freon Molecules
Zeitschrift fur Physik C, Volume 31, p203-211, 1986

42. BEBC WA59 Collaboration
Coherent Production of π^+ Mesons in ν-neon Interactions
Zeitschrift fur Physik C, Volume 31, p523-526, 1986

43. The FNAL E632 Collaboration
Coherent Production of Single Pions and ϱ Mesons in Charged-Current Interactions of Neutrinos and Antineutrinos on Neon Nuclei at the Fermilab Tevatron
Physical Review D, Volume 47, p2661-2674, 1993

44. The K2K Collaboration
Search for Coherent Charged Pion Production in Neutrino-Carbon Interactions
Physical Review Letters, Volume 95, p252301, 2005

45. The MiniBooNE Collaboration
First observation of coherent π^0 production in neutrino-nucleus interactions with $E_\nu < 2$ GeV
Physics Letters B, Volume 664, p41-46, 2008

46. The SciBooNE Collaboration
Search for charged current coherent pion production on carbon in a few-GeV neutrino beam
Physical Review D, Volume 78, p112004, 2008

47. The NOMAD Collaboration
A Measurement of Coherent Neutral Pion Production in Neutrino Neutral Current Interactions in NOMAD
Physics Letters B, Volume 682, p177-184, 2009

48. The SciBooNE Collaboration
Improved measurement of neutral current coherent π^0 production on carbon in a few-GeV neutrino beam
Physical Review D, Volume 81, p111102, 2010

49. D. Rein and L.M. Sehgal
PCAC and the Deficit of Forward Muons in π^+ Production by Neutrinos
Physics Letters B, Volume 657, p207-209, 2007

50. S.L. Adler
Tests of the Conserved Vector Current and Partially Conserved Axial-Vector Current Hypotheses in High-Energy Neutrino Reactions
Physical Review, Volume 135, p963-966, 1964

51. C.A. Piketty and L. Stodolsky
Diffraction Model of High-Energy Leptonic Interactions
Nuclear Physics B, Volume 15, p571-600, 1970

52. C. Berger and L. Sehgal
Partially conserved axial vector current and coherent pion production by low energy neutrinos
Physical Review D, Volume 79, p053003, 2009

53. L. Alvarez-Ruso et al.
Charged current neutrino-induced coherent pion production
Physical Review C, Volume 75, p055501, 2007

54. L. Alvarez-Ruso et al.
Erratum: Charged current neutrino-induced coherent pion production
Physical Review C, Volume 80, p019906(E), 2009

55. L. Alvarez-Ruso et al.
Neutral current coherent pion production
Physical Review C, Volume 76, p068501, 2007

56. E. Oset and L.L. Salcedo
Delta self-energy in nuclear matter
Nuclear Physics A, Volume 468, p631-652, 1987

57. E. Oset et al.
Many-body approach to low-energy pion-nucleus scattering
Nuclear Physics A, Volume 554, p554-579, 1993

58. H Budd et al.
Modelling Quasi-elastic Form Factors for Electron and Neutrino Scattering
arXiv:hep-ex/0308005, 2003

59. S. Boyd et al.
Comparison of Models of Neutrino-Nucleus Interactions
AIP Conference Proceedings, Volume 1189, p60-73, 2009

60. E.A. Paschos and D. Schalla
Coherent pion production by neutrinos
Physical Review D, Volume 80, p033005, 2009

61. E. Hernandez et al.
Weak pion production off the nucleon
Physical Review D, Volume 76, p033005, 2007

62. S.X. Nakamura et al.
Coherent Pion Production in the Neutrino-Nucleus Scattering in Few-GeV Region
arXiv:nucl-th/0901.2366, 2009

63. The T2K Collaboration
The T2K Experiment
NIM A, Volume 659, p106-135, 2011

64. The T2K Collaboration
T2K neutrino flux prediction
Physical Review D, Volume 87, p012001, 2013

65. The Super-Kamiokande Collaboration
Search for Proton Decay via $p \to e^+\pi^0$ and $p \to \mu^+\pi^0$ in a Large Water Cherenkov Detector
Physical Review Letters, Volume 102, p141801, 2009

66. The T2K Collaboration
Measurements of the T2K neutrino beam properties using the INGRID on-axis near detector
NIM A, Volume 694, p211-223, 2012

67. The T2K ND280 P0D Collaboration
The T2K ND280 Off-Axis Pi-Zero Detector
NIM A, Volume 686, p48-63, 2012

68. G. Lopez et al.
Measurement of NC π^0 Production with the T2K π^0 Detector (P0D)
T2K Technical Note 056, Version 6

69. The T2K ND280 FGD Collaboration
The T2K fine-grained detectors
NIM A, Volume 696, p1-31, 2012

70. S. Oser
Elemental Composition of the FGD XY Modules
T2K Technical Note 091, Version 1.2

71. The T2K ND280 TPC collaboration
Time Projection Chambers for the T2K Near Detectors
NIM A, Volume 637, p25-46, 2011

72. A. Vacheret et al.
Characterization and Simulation of the Response of Multi Pixel Photon Counters to Low Light Levels
NIM A, Volume 656, p69-83, 2011

73. The NA61/SHINE Collaboration
Pion emission from the T2K replica target: Method, results and application
NIM A, Volume 701, p99-114, 2013

74. G. Battistoni et al.
The FLUKA code: description and benchmarking
AIP Conference Proceedings, Volume 896, p31-49, 2007

75. R. Brun, F. Carminati, and S. Giani
GEANT: Detector description and simulation tool
CERN-W5013, 1994

76. The Geant4 Collaboration
Geant4 - a simulation toolkit
NIM A, Volume 506, p250-303, 2003

77. A. Cervera-Villanueva et al.
"RecPack" a reconstruction toolkit
NIM A, Volume 534, p180-183, 2004

78. F. DiLodovico, et al.
CCQE-like and CC-non-QE-like numu event selections in the ND280 tracker using Run 1+2 data
T2K Technical Note 093, Version 4

79. F. DiLodovico et al.
CCQE-like and CC-non-QE-like numu event selections in the ND280 tracker using Run 1+2+3 data
T2K Technical Note 128, Version 4

80. The T2K collaboration
Measurement of the Inclusive NuMu Charged Current Cross Section on Carbon in the Near Detector of the T2K Experiment
Physical Review D, Volume 87, p092003, 2013

81. F. DiLodovico et al.
CC-multiple-pion ν_μ event selections in the ND280 tracker using Run 1+2+3+4 data
T2K Technical Note 152, Version 4.1

82. G Cowan et al.
Asymptotic formulae for likelihood-based tests of new physics
European Physical Journal, Volume 71, p1554, 2011

83. M. Hartz et al.
Flux Prediction and Uncertainties for the 2012a Oscillation Analysis
T2K Technical Note 099, Version 7

84. C. Andreopoulos et al.
The GENIE Neutrino Monte Carlo Generator Physics & User Manual
http://genie-mc.org

85. C. Andreopoulos et al.
Neutrino Generator (GENIE) Uncertainties and 2010a ν_μ-Disappearance / ν_e-Appearance Oscillation Analysis Systematics
T2K Technical Note 035, Version 2

86. C. Andreopoulos et al.
Handling Neutrino Interaction Uncertainties using Event Reweighing
T2K Technical Note 007, Version 1

87. E. Frank et al.
B-field calibration and systematic errors
T2K Technical Note 081

88. A. Hillairet et al.
ND280 tracker tracking efficiency
T2K Technical Note 075, Version 1.1

89. F. Dufour et al.
Systematics on Out-of-Fiducial-Volume Backgrounds in the ND280 Tracker
T2K Technical Note 098, Version 1

90. J. Myslik
Determination of pion secondary interaction systematics for the ND280 tracker ν_μ analysis
T2K Technical Note 125, Version 1

91. Thomas Lindner
Private communication

92. P. de Perio et al.
Cross section parameters for the 2012a oscillation analysis
T2K Technical Note 108, Version 1.5